Physical and chemical characterisation of exfoliated layered nanomaterials

Aline Amorim Graf

Submitted for the degree of Doctor of Philosophy

University of Sussex

August 2020

Declaration

I hereby declare that this thesis has not been and will not be submitted in whole or in part to another University for the award of any other degree.

Signature:

Aline Amorim Graf

UNIVERSITY OF SUSSEX

ALINE AMORIM GRAF, DOCTOR OF PHILOSOPHY

PHYSICAL AND CHEMICAL CHARACTERISATION OF EXFOLIATED LAYERED NANOMATERIALS

Liquid phase exfoliation (LPE) is a versatile and scalable production technique for two-dimensional nanomaterials, such as graphene and molybdenum disulfide (MoS_2). Solution processing enables a wide range of applications, many of which are sensitive to nanosheet microscopic properties, including size, thickness and functionalisation. Yet these nanosheets remain poorly characterised with the lack of standardisation. A method to sonochemically edge functionalise MoS_2 in acetone is detailed here; a way of producing stable dispersions over extended periods of time (over one year) at high concentrations. By using a range of techniques, it is shown that this stabilisation is achieved through a self-limiting oxidation of MoS_2 at the edges. The method results in enhanced catalytic performance for MoS_2 and potentially other sulfur containing layered materials.

In addition, a general method to reconstruct nanosheets size and thickness distributions based on Raman spectroscopic metrics is demonstrated with graphene and MoS_2. This is essential for any research that relies on quantifying the influences of size and thickness on applications, such as mechanical reinforcement, electrical conductivity, sensing, and catalysis. A new metric for characterising layer number of MoS_2 nanosheets is developed using an intensity ratio of resonant Raman modes. Raman spectroscopy is less time consuming and less dependent on sample preparation when compared to microscopic characterisation techniques that yield the same information. The method presented here is more robust than current literature metric as it does not rely on mode positions, which shift depending on factors inherent to the sample such as strain, doping, and defect density. The metric was developed for LPE nanosheets but it can also be applied to mechanically exfoliated sheets. The first proposed metric for LPE nanosheet length was developed using the main Raman modes of MoS_2 for resonant spectra, showing excellent agreement with microscopic measurements. It is anticipated this combination of mapping and metric analysis can be extended to other materials, paving the way for a much-needed standardisation for industry and laboratory research applications of layered nanomaterials.

Publications

Elements of this thesis have contributed (in part or in their entirety) to the following publications:

1. Matthew J. Large, Sean P. Ogilvie, Manuela Meloni, **Aline Amorim Graf**, Giuseppe Fratta, Jonathan P. Salvage, Alice A. K. King and Alan B. Dalton. Functional liquid structures by emulsification of graphene and other two-dimensional nanomaterials. *Nanoscale*, 10 (4). p. 1582-1586, January 2018. DOI: 10.1039/C7NR05568D (AAG performed characterisation).

2. Yuanyang Rong, Matthew J. Large, Manoj Tripathi, Sean P. Ogilvie, **Aline Amorim Graf**, Boyang Mao, Jacob Tunesi, Jonathan P. Salvage, Alice A. K. King, Alessia Pasquazi, Marco Peccianti, Richard Malpass-Evans, Neil B. McKeown, Frank Marken, Alan B. Dalton. Charge transfer hybrids of graphene oxide and the intrinsically microporous polymer PIM-1. *ACS Applied Materials & Interfaces*, 11 (34). p. 31191-31199, August 2019. DOI: 10.1021/acsami.9b09832 (AAG performed Raman characterisation and analysis).

3. **Aline Amorim Graf**, Matthew J. Large, Sean P. Ogilvie, Yuanyang Rong, Peter J. Lynch, Giuseppe Fratta, Santanu Ray, Aleksey Shmeliov, Valeria Nicolosi, Raul Arenal, Alice A. K. King, Alan B. Dalton. Sonochemical edge functionalisation of molybdenum disulfide. *Nanoscale*, 11 (33). pp. 15550-15560, August 2019. DOI: 10.1039/C9NR04974F (AAG performed materials preparation, characterisation and analysis).

4. Matthew J. Large, Sean P. Ogilvie, **Aline Amorim Graf**, Peter J. Lynch, Marcus A. O'Mara, Thomas Waters, Izabela Jurewicz, Jonathan P. Salvage, and Alan B. Dalton. Large-scale surfactant exfoliation of graphene and conductivity-optimized graphite enabling wireless connectivity. *Advanced Materials Technologies*, p. 2000284, May 2020. DOI: 10.1002/admt.202000284 (AAG performed materials preparation and characterisation).

5. Marcus A. O'Mara, Sean P. Ogilvie, Matthew J. Large, **Aline Amorim Graf**, Anne C. Sehnal, Peter J. Lynch, Jonathan P. Salvage, Izabela Jurewicz, Alice A. K. King, and Alan B. Dalton. Ultrasensitive strain gauges enabled by graphene-stabilized silicone emulsions. *Advanced Functional Materials*, p. 202002433, June 2020. DOI: 10.1002/adfm.202002433 (AAG performed Raman characterisation and analysis).

6. Sean P. Ogilvie, Matthew J. Large, Adam J. Cass, **Aline Amorim Graf**, Anne C. Sehnal, Marcus A. O'Mara, Peter J. Lynch, Jonathan P. Salvage, Marco Alfonso, Philippe Poulin, Alice A. K. King, and Alan B. Dalton. Nanosheet-stabilized emulsions: Ultra-low loading segregated networks and surface energy determination of pristine few-layer 2D materials, 2020. arXiv:2005.06330 [cond-mat, physics:physics] (Submitted) (AAG performed Raman characterisation and analysis).

7. **Aline Amorim Graf**, Sean P. Ogilvie, Hannah J. Wood, Christopher J. Brown, Manoj Tripathi, Alice A. K. King, Alan B. Dalton, and Matthew J. Large. Raman metrics for molybdenum disulfide and graphene enable statistical mapping of nanosheet popula-

tions. *Chemistry of Materials*, 32 (14). p. 6213-6221, June 2020. DOI: 10.1021/acs.chemmater.0c02109 (AAG performed materials preparation, characterisation and analysis).

8. Peter J. Lynch, Sean P. Ogilvie, Matthew J. Large, **Aline Amorim Graf**, Marcus O'Mara, James Taylor, Jonathan P. Salvage, and Alan B. Dalton. Graphene-based printable conductors for cyclable strain sensors on elastomeric substrates. *Carbon*, 169. p. 25-31, July 2020. DOI: 10.1016/j.carbon.2020.06.078 (AAG performed materials preparation and characterisation).

9. Peter J. Lynch, **Aline Amorim Graf**, Sean P. Ogilvie, Matthew J. Large, Jonathan P. Salvage, and Alan B. Dalton. Surfactant-free liquid-exfoliated copper hydroxide nanocuboids for non-enzymatic electrochemical glucose detection. *Journal of Materials Chemistry B*, 8. p. 7733-7739, July 2020. DOI: 10.1039/D0TB01476A (AAG performed Raman characterisation and analysis).

10. Rhiannon W. Harries, Christopher J. Brown, Sean P. Ogilvie, Matthew J. Large, Keiran Clifford, **Aline Amorim Graf**, Thomas Simon, Georgios Giamas, Alan B. Dalton, and Alice A. K. King (2020) Langmuir films of layered nanomaterials: edge interactions and cell culture applications. *The Journal of Physical Chemistry B*, 124 (33). p. 7184-7193, July 2020. DOI: 10.1021/acs.jpcb.0c05573 (AAG performed materials preparation and characterisation).

Acknowledgements

Firstly, I would like to thank my parents, Amauri and Léia. The cliché that if it wasn't for them, I would not be here is true for obvious biological reasons but especially for my dad's "why not?" when I was still unsure if I wanted to apply for a one-year scholarship and move to the UK in 2014. I'm grateful they accepted my career choice and always encouraged me to follow my path, even if that meant meeting twice a year. Also, I would like to thank them for their constant support and love, even from a distance.

I want to thank my supervisor Alan for giving me the opportunity to be part of the group for a summer placement at the University of Surrey, and then inviting me to come back for a fully-funded PhD degree. Thank you for giving us independence but also clear feedback when needed. Also, for encouraging meaningful science discussions (especially in the pub).

I would also like to recognise the contributions from my second supervisor Alice, who always notices when things could be improved. Also, Izabela for being supportive during those four months we worked together in Surrey and also for being so enthusiastic about nanomaterials, which influenced my decision to pursue this career.

Special thanks and recognition to Matt for answering (or at least trying to) all my constant questions. I would like to thank him for his encouragement throughout these three years but especially during this final writing stage. I'm grateful for all his thorough proofreading and for believing we could solve this Raman project from the beginning.

I would like to thank Sean for proofreading everything quickly (even this thesis) and for always raising interesting questions in the process. I recognise the contributions and new insights of every co-author of my papers, both from this University and from other institutions.

I want to extend my thanks the rest of the Materials Physics group for all the science (and also non-science related) discussions: Peter, Manoj, Annie, Marcus, Frank, Abdullah, Hannah, Chris, Keiran, Conor, Cencen, and Adel.

I would also like to express my gratitude to Nick for always encouraging me and for his support during these challenging times. Finally, a special thanks to my friends and family who always had a positive word of encouragement to say during these three years.

Contents

List of Figures

Chapter 1

Introduction

Nanotechnology covers both production and applications of physical, chemical, and biological materials in sub-micron scales [13]. It encompasses the ability to control and explore their unique properties in novel devices and structures [14]. Graphene is the most renowned nanomaterial, which has attracted wide research interest because of its outstanding thermal conductivity [15], mechanical properties [16], high carrier mobility [17], and molecular barrier characteristics [18, 19], among others.

The nanotechnology field has been growing rapidly in recent years. One indicator of this growth is the number of publications, as seen in Figure 1.1. Books, articles, and reviews that contained the word "nano" in their title, abstract or keywords reached 416,000 publications, since 1943. An exponential trend is also seen for research on graphene, reaching 164,000 publications, since 1985, at time of writing.

The emerging properties of few-layer structures are not limited to the carbon family of graphene but, in particular, transition metal dichalcogenides (TMD) show a large variety of enhanced electronic [20, 21, 22], optical [23, 24, 21, 25, 26], chemical [27, 28, 29, 30], thermal [31, 32], and mechanical properties [33]. Depending on their chemical composition, they may have semiconducting, semi-metallic or metallic behaviour [34]. The varied chemistry of the TMDs presents opportunities for moving beyond graphene, which is relatively chemically inert, paving the way to novel fundamental and technological research on nanomaterials [35].

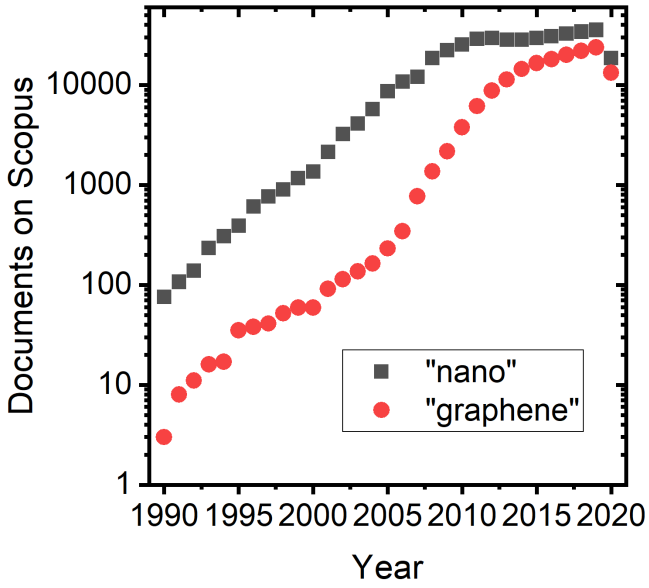

Figure 1.1: Number of publications between 1990 and 2020 containing the words "nano" (black) and "graphene" (red). Data was collected on 29th June 2020 using Scopus. Results include the use of the words in title, abstract, and keywords for books, articles, and reviews.

Research motivation

Following the increasing interest on potential world-wide applications of the nanomaterials, the European Union has proposed actions and acknowledged issues arising from implementing nanotechnology for the benefit of society since 2004 [36, 37, 38, 39]. The trend is not limited to Europe. The Food and Agriculture Organization of the United Nations and the World Health Organization held an expert meeting in 2009. The result is a document published in 2013 that highlights the importance of the development of applications in agriculture, water treatment, preservation, and packaging, which should bring benefits to farmers and consumers [40]. It was also recognised the need for clear international definitions and proper assessment of health risks arising from production and also use of nanomaterials. Since the materials have different properties from their bulk structure counterpart, the effects on health might also vary. A complete study is necessary before the uptake of nanomaterials by industry, since many factors influence toxicity of materials, such as chemical composition, surface area, size, and shape [41].

In order to harness the novel properties of nanomaterials, different production techniques can be used, each one with its advantages and drawbacks (discussed in subsequent chapters). This thesis focuses on liquid phase exfoliation, which has the potential to produce large quantities of high-quality nanosheet dispersions, facilitating the post-processing necessary for a range of applications [42, 43]. The solvent known to produce high concentrations and exfoliation yield for layered materials is *N*-methyl-2-pyrrolidone (NMP) [42, 43, 44, 45, 46, 47]. The major drawbacks of NMP are the presence of residues on the nanosheets and its toxicity [48, 49, 50, 51, 52]. This solvent decomposes upon heating, a standard procedure used to deposit dispersions on substrates for further characterisation, producing toxic fumes such as nitrogen oxides and carbon monoxide [53].

Research on alternative solvents has been growing recently. Layered materials are generally insoluble in water and require amphiphilic surfactants or polymers for successful exfoliation and stabilisation in this solvent [52, 54]. Forsberg *et al.* tested a combined mechanical exfoliation with further liquid processing without any additives [55]. A good degree of exfoliation was obtained, however stability, determined by the concentration difference over time, was at least 250 times lower than for an NMP dispersion. Different organic solvents have been studied [56, 44, 57, 58, 59] and usually achieve exfoliation but show poor stability over long periods of time. Motivation for the work presented in this thesis is to investigate solvents considered poor for liquid processing of layered materials but have desirable properties such as low-toxicity and facilitation of further processing for applications.

Another motivation is related to a standardised and reliable characterisation of nanomaterials. An international definition of terms related to graphene and other layered materials, including production methods, properties, and characterisation was created in 2017 by the International Organization for Standardization [60]. A specific guide for graphene was created by the UK National Physical Laboratory (NPL) [61] presenting a range of techniques to determine accurately substrate coverage, layer number, lateral dimensions, alignment, and disorder level for different production methods. The guide also includes sample preparation procedures and sources of uncertainty. One of the main

characterisation techniques suggested by this guide is Raman spectroscopy, a laser-based vibrational spectroscopy technique, which is generally non-destructive and yields chemical information that can be coupled with physical properties following microscopic calibration.

The first Raman spectrum of graphite was reported in 1970 by Tuinstra and Koenig [62]. Following the renewed interest after the isolation of graphene by Geim and Novoselov in 2004 [17], Ferrari *et al.* reported on the Raman spectra of graphene in 2006 [63]. Specifically, they studied the modifications to the spectrum as a function of varying layer number and defects. This understanding lead to the development of phenomenological metrics for layer number and size of liquid-processed graphene nanosheets [64].

The Raman spectrum of bulk molybdenum disulfide (MoS_2), the archetypal TMD, was first reported around the same time as graphite by Verble and Wieting [65, 7] and the monolayer spectrum in 2010 [66]. However, the same understanding obtained from graphene cannot be transferred to MoS_2 easily since the equivalent Raman modes are not always observed [67]. In order to extend understanding of Raman of LPE graphene to MoS_2 and other layered materials, it will be important to investigate the representativeness of Raman spectra of nanosheet populations where the laser spot contains a large number of sheets.

Thesis outline

This thesis has two main research questions. One of them is to understand the liquid processing of MoS_2 in non-standard solvents and any effects on the nanosheet chemistry and morphology during ultrasonication. The use of these solvents facilitates novel film processing methods. The other aim is to investigate whether a new approach based on Raman microscopy expands the amount of information obtained while characterising layer number and length of layered material nanosheets.

The interesting properties of layered materials, focussing on the TMD MoS_2, are discussed in Chapter 2. Also, a general overview of the most common exfoliation techniques is given. Chapter 3 has a more detailed and applied discussion about the exfoliation processes and characterisation techniques used in subsequent experimental chapters. In

Chapter 4, by describing the exfoliation of MoS_2 in acetone, the current framework (based on Hansen parameters) to choose appropriate solvents that give the highest concentrations and exfoliation yields is analysed. The chapter also describes the influence of such modifications on macroscopic properties and their self-limiting nature. This is achieved by a spontaneous functionalisation of the nanosheets edges with molybdenum oxides.

Chapter 5 details a mapping approach to reconstruct size and thickness distributions using Raman microscopy. By creating Raman maps with resolution-limited pixel size (related to the diffraction limit) and applying spectroscopic metrics to every pixel and creating histograms of the results, instead of averaging them, it is possible to obtain near-complete information about the properties of a sample. The approach is demonstrated using literature graphene metrics. The prospect of extending it to MoS_2 is discussed, which led to the development of calibrated metrics with microscopic verification for layer number and lateral size using resonant Raman spectroscopy, as described in Chapter 6.

Experiments and analysis in this thesis were devised and conducted by myself, except where stated otherwise. This thesis offers new insight about modifying the solubility and electrochemical performance of MoS_2 nanosheets during exfoliation in a common solvent. Also, the characterisation of layer number and size for MoS_2, important for both academic research and industrial applications, uses a general approach that can be extended to other layered materials.

Chapter 2

Layered nanomaterials

Some materials exhibit emerging properties as they are confined to a nanometric length scale. In this chapter, examples of these properties are discussed, with a particular emphasis on transition metal dichalcogenides. Their different polytypes and electronic band structures are considered, which explain some of their observed optoelectronic properties. Exfoliation and synthesis of layered materials are also discussed in terms of their main advantages and drawbacks.

2.1 Introduction

Nanomaterials are defined as materials with at least one dimension of or under 100 nm [68]. This is usually interpreted in the sense that the nanostructured material as a result differs from the bulk form in any of its physical, electronic, or chemical properties. These differences often originate from the high surface area to volume ratio [68].

Layered materials allow preparation of a special class of nanomaterials with thickness-dependent properties. They are strongly bonded in-plane but weakly bonded by the van der Waals force in the perpendicular direction, and as such may in principle be cleaved into atomically-thin layers. Graphene is the most well-known two-dimensional (2D) nanomaterial. In a graphene nanosheet, carbon atoms are organised in a hexagonal configuration and bonded with sp^2 hybridisation [69]. The carbon family is completed by the zero-dimensional (0D) fullerene [70], the 1D carbon nanotube [71], and 3D graphite. Other

examples of nanomaterials are hexagonal boron nitride (h-BN), graphene oxide, transition metal dichalcogenides (TMDs), III-VI layered semiconductors (GaS, Bi_2Se_3), black phosphorus, silicene, transition metal carbides, metal oxides, layered double hydroxides, quantum dots, and perovskite nanocrystals [72].

2.2 Transition metal dichalcogenides

Transition metal dichalcogenides are compounds having the chemical formula MX_2, where M is a transition metal (such as Mo, W, Nb, Hf, V) and X is a chalcogen (S, Se, Te) [72]. The monolayers are formed by the metal atom covalently bonded between two chalcogen atoms. These layers are held in the bulk form by van der Waals force. This is analogous to stacking of graphene layers in graphite. Over 60 transition metal dichalcogenides are known and about 40 of them have a layered crystal structure [20]. TMDs proved to be an interesting route for research since their similar crystal and electronic structure allows for logical extensions to explain similar properties. And yet, their different compositions result in a wide range of possible applications for their optoelectronic properties, e.g. photoluminescence [24, 25, 26], *n*- or *p*-type behaviour [28, 29], and catalytic performance [30, 27]. Molybdenum disulfide (MoS_2), the most studied TMD, is a naturally-occurring and abundant material, which has been known for several centuries [73]. Its dry lubricant properties [74], catalytic activity for hydrodesulfurisation in refineries [75], and intercalation chemistry [76] have been exploited since the 1970s.

Monolayers of MoS_2 were isolated almost 20 years before [77] the Nobel prize winning work on graphene [17]. However, it was not until the field matured with the renewed interest led by the work on graphene and the development of exfoliation techniques that new applications became possible. In 2010, Mak *et al.* [78] reported a tunable bandgap in MoS_2 nanosheet based on layer number. More specifically, they found a transition from an indirect bandgap of 1.3 eV in bulk MoS_2 to a direct band gap of 1.9 eV in the monolayer form. The direct band gap results in a higher luminescence quantum efficiency for MoS_2 monolayers by a factor of 1000 compared to the bulk form [78]. This leads to applications in light emitting diodes, solar cells and photodetectors [73]. One year later, a single-layer

MoS_2 transistor was reported, showing high electron mobility and high on/off current ratio [79].

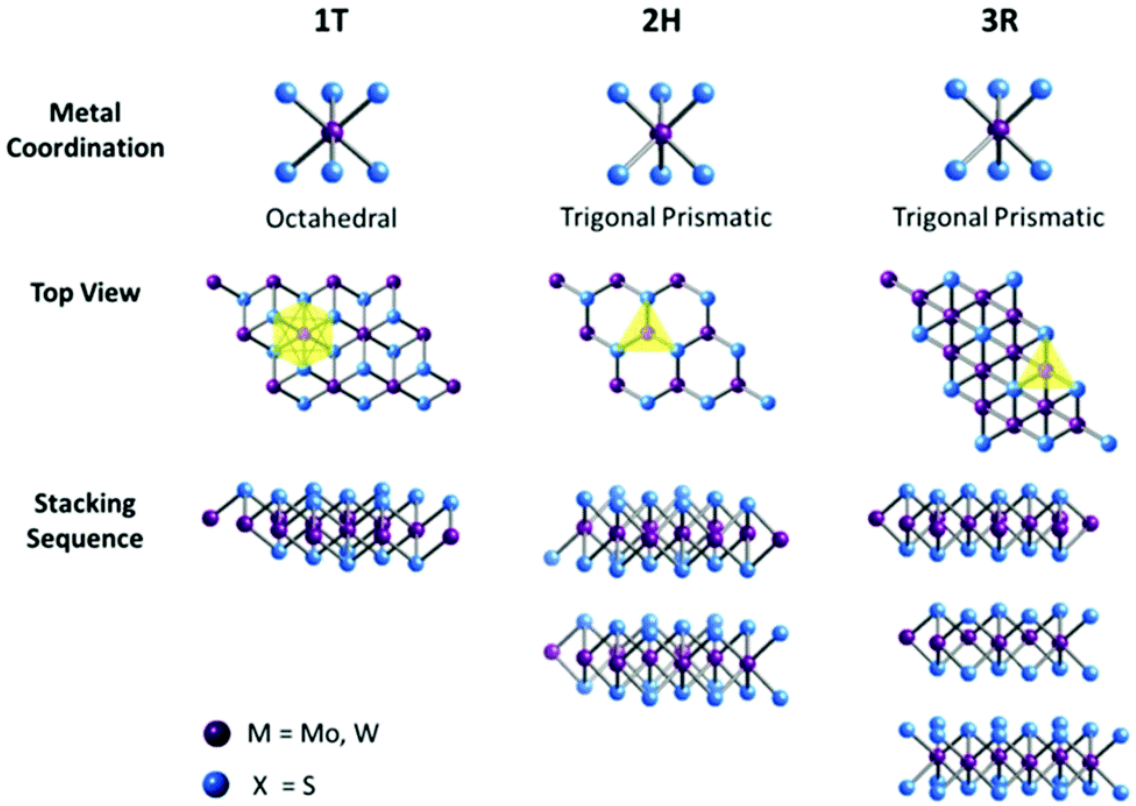

Figure 2.1: Columns show an example of different crystal phases for MoS_2 and WS_2: 1T, 2H, and 3R. Rows illustrate the metal coordination, top view of the monolayer, and the stacking sequence in the bulk structure. Image from Toh *et al.* [1].

Some TMDs are naturally occurring whilst others are synthesised. For example, MoS_2 can be mined as the mineral molybdenite [7]; the same for WS_2 and tungstenite. Meanwhile, $MoSe_2$ and WSe_2 are both synthesised at high temperatures [80, 81]. MoS_2 can be found naturally in the form of two different stable polytypes: 2H and 3R. The notation used here represents the crystal symmetry, where H stands for hexagonal, R, rhombohedral, and T, tetragonal. The numbers represent the number of layers in the unit cell. The 2H-polytype is dominant for all bulk TMDs at about 80 at.% [82], following the same trend of molybdenite natural occurrence [83]. MoS_2 has another metastable polytype: 1T [84]. Figure 2.1 shows each polytype and corresponding metal coordination. For both naturally occurring polytypes, each molybdenum atom has a trigonal prismatic coordination and it is covalently bonded to six sulfur atoms, while the metastable phase

has octahedral configuration [1]. A recent report by Lin *et al.* [85] found that the 1T-phase of WS_2 is a direct band gap semiconductor and that the 1T'-phase has metallic behaviour. The notation 1T' indicates this phase is a distorted 1T polytype which is deformed into a zig-zag chain structure [85]. This distortion leads to lack of inversion symmetry with regards to different Mo-S bond lengths, as opposed to the identical bonds in 2H and 3R-MoS_2 [2]. The main difference between the crystal phases is the 3D stacking along the c-axis. The 1T' phase has one MoS_2 layer per unit cell and no overlapping sulfur atoms. The 2H phase contains two layers in each unit cell and the sulfur atoms are aligned in the c-axis direction. This configuration leads to the maximum interlayer spacing of 3.087 Å, resulting in the highest stability of the three polytypes. The 3R phase has three layers per unit cell with no overlapping sulfur atoms [2].

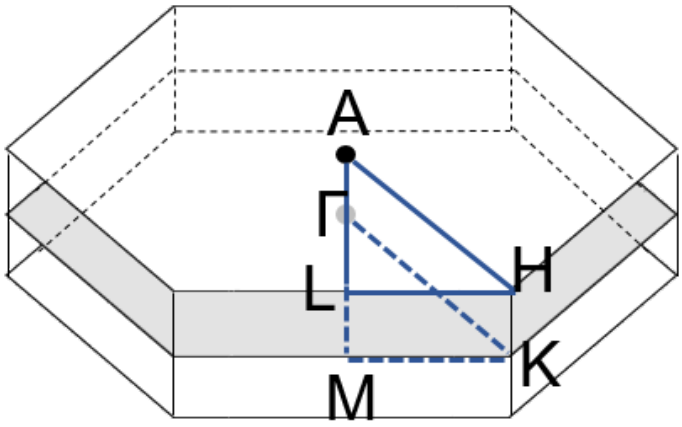

Figure 2.2: Schematic representations of the Brillouin zone corresponding to 2H-MoS_2.

In order to explain the band structure configurations in solids, the free-electron theory may be modified by including an additional periodic potential resulting from the crystal lattice, which gives the band theory [68]. Different symmetry points, also known as critical points, can be identified in the first Brillouin zone. For layered materials like graphene and 2H-MoS_2, the hexagonal lattice gives the following points (shown in Figure 2.2): Γ, the centre of the Brillouin zone; A, the centre of the hexagonal face; H, a corner point, K, middle of an edge joining two rectangular faces; L, middle of an edge joining a rectangular and a hexagonal face, and M, centre of a rectangular face.

Energy bands are ranges of energies that electrons may have in a solid. For single atoms, according to quantum theory, electrons can only have discrete levels of energy. In a crystalline solid, these electrons are influenced by adjacent nuclei, causing their electron orbitals to overlap and the well-defined levels become bands [86]. The valence band contains the outermost electrons in a solid. The electrons in this band, when provided with sufficient energy, reach the conduction band and become free electrons, which results in conductivity [87].

For conductors, the two bands overlap and low energy electrons can reach the conduction band easily. For insulators, the two bands are separated by a wide gap. For intrinsic semiconductors, the forbidden gap is narrow and electrons can move to the conduction band by thermal excitation [88]. Extrinsic semiconductors have additional bands in this forbidden gap and different numbers of charge carriers. If there are more electrons than holes (an empty state that behaves like a positively-charged electron), it is said the semiconductor is of *n*-type. Alternatively, if there are more holes than electrons, they are *p*-type [68].

Fermi level is defined as the energy in a solid at which half of the quantum states are occupied. The probability of a fermion, a particle with half-integer spin (such as an electron), being at a certain energy ε is given by the Fermi-Dirac distribution:

$$f(\varepsilon) = \frac{1}{e^{(\varepsilon-\mu)/k_B T} + 1} \tag{2.1}$$

where k_B is the Boltzmann's constant, T is the absolute temperature, and μ is the chemical potential. At absolute zero μ is equal to the Fermi level, since in the limit $T \to 0$, the function varies from one to zero, meaning it varies from filled to empty [89]. For conductors, it lies in the conduction band, and for insulators and semiconductors, in the gap between the conduction and valence bands [90]. This concept shows that conductors still conduct a current at absolute zero, whereas all other materials become perfect insulators. For band structure calculations, energy levels are represented as a difference to the Fermi level. This representation is useful because at absolute zero, the band below the Fermi level is completely filled and above it, completely empty [88].

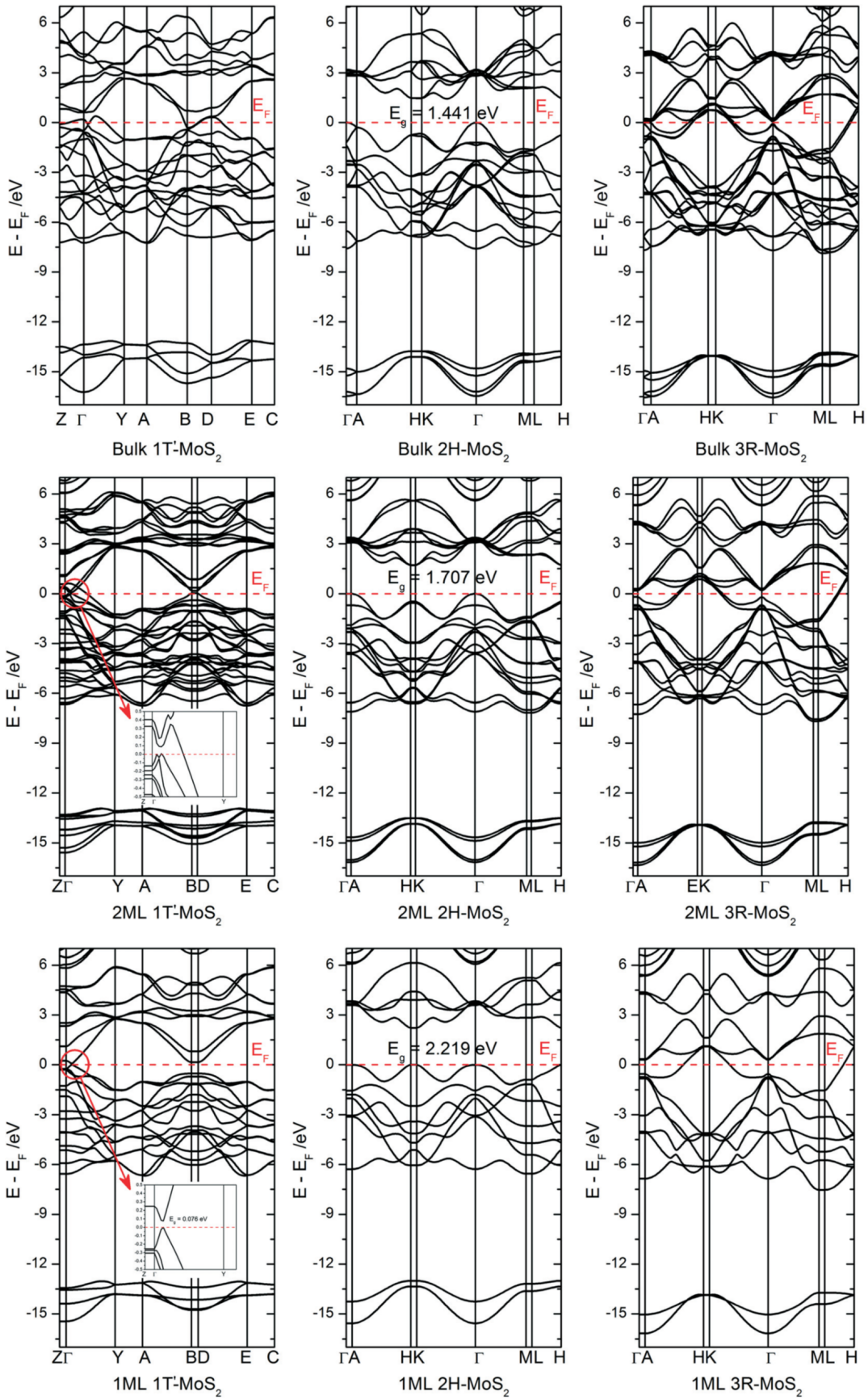

Figure 2.3: Calculated band structures of MoS_2 nanosheets. First column corresponds to 1T' phase, second, 2H, and third, 3R. Each row is the structure for bulk, bilayers, and monolayers, respectively. Image from Zhao and Liu [2].

Figure 2.3 illustrates the calculated electronic band structures for different number of layers and polytypes of MoS_2. Comparing the bulk forms, it is clear that both 1T' and 3R phases have conducting behaviour, since the energy levels cross the Fermi energy level. Bulk 2H-MoS_2 has semiconducting characteristics. The valence band maximum is located at the Γ point whilst the conduction band minimum is between the Γ and K points. The fact that these are different points, shows that bulk 2H-MoS_2 has an indirect band gap.

For an indirect band gap, a photon cannot be emitted because the crystal momentum of the charge carriers is not the same in both valence and conduction band. It must transfer momentum to the crystal lattice, due to momentum conservation, whilst in an intermediate state [78]. Calculated value for the band gap in the figure is 1.441 eV [2] and experimental value is 1.29 eV [78]. The band gap originates from the crystal potential field, a measure of the interaction between the atomic core and the valence electrons. The fact that the sulfur atoms are aligned in the c-axis direction for the 2H-MoS_2 structure means that is a strong repulsive force between them. For the other phases, the sulfur atoms do not align, resulting in an attractive force and the overlap of wave functions, and ultimately the absence of a band gap.

With decreasing layer number to 2H-MoS_2 monolayer, the valence band maximum shifts from the Γ point. The valence band energy at K point increases and assumes the same value. The conduction band minimum shifts towards the K point. This results in a direct band gap of 2.219 eV [91, 2] for the calculations shown in Figure 2.3. This direct gap also gives rise to photoluminescence of 2H-MoS_2 monolayer [78]. Experimental results show a value of 1.9 eV [78]. For the other polytypes, the conduction band shift is negligible. It is interesting to note that at the B-D line, for the 1T' phase, the monolayer has semiconducting behaviour, with a 0.683 eV direct band gap at that point [2]. For the bilayer, the valence and conduction bands overlap just at that point, resulting in a semi-metallic conductivity. For layer number larger than two, both bands overlap throughout the whole line, showing a metallic behaviour. According to Figure 2.3, the 3R phase is metallic and has an energy level shift near the Γ point. Such behaviour was not observed in other calculations, where semi-conducting properties, similar to that of 2H-MoS_2 were found [92, 93, 94]. Zhao

and Liu [2] also found that this phase has the largest surface and cleaving energy, and the smallest binding and van der Waals energy out of the three polytypes. The variations observed in band structure present an interesting route to modulate the electronic properties for different applications as a function of interlayer separation, in the form of the different phases, but also with varying layer number [95, 96].

Phonon behaviour is also critical to understand the electronic and optical properties of the TMDs [97]. Phonons are quanta of crystal lattice vibrations that propagate in the lattice as a wave and show dispersion, an effect that causes a change in wavelength with frequency [98]. Limited phonon mobility has been shown to limit optical properties in monolayer MoS_2 [99]. The concept is also useful to understand thermal conductivity in non-metallic solids, the temperature dependence of electrical conductivity in metals, their infrared absorptions, and inelastic light scattering [68]. The coupling between electrons and phonons is responsible for macroscopic quantum phenomena, especially thermal and electrical transport.

2.3 Exfoliation and synthesis of layered materials

There are several methods to produce nanomaterials. They can be divided into two main categories: bottom-up and top-down approaches. The first one involves synthesising the few-layer materials whilst the second, consists of the exfoliation of the bulk material [100]. Each method produces materials that can have suitability for different applications. The techniques used in this thesis were mechanical exfoliation and liquid-phase exfoliation, including high-pressure homogenisation.

2.3.1 Mechanical exfoliation

Nobel Prize winners Geim and Novoselov performed their pioneering work on graphene in 2004 using micromechanical cleavage as the technique to exfoliate graphite into stable nanosheets [17]. In the following year, they extended the approach to other materials: h-BN, MoS_2, $NbSe_2$, $Bi_2Sr_2CaCu_2Ox$ [101]. The mechanical exfoliation (ME) process

works by peeling off thin nanosheets from a bulk crystal using Scotch tape. Those sheets are then transferred to the desired substrate [102]. An intermediate transfer substrate, usually a polymer layer, like PDMS (polydimethylsiloxane) or PVA (polyvinyl alcohol) is used. It is known that ME is an efficient process to produce large (tens of microns in lateral size) and well-exfoliated nanosheets. However, the main drawbacks associated with the process are low yield and the poor transfer efficiency, in addition to impurities often being present in the form of residual tape adhesive. Therefore, a different approach is necessary to fill the expanding industry demand for nanomaterials, following the growing interest in graphene and its enhanced mechanical and electrical properties [103, 104].

2.3.2 Liquid-phase exfoliation

Liquid-phase exfoliation (LPE) is usually based on ultrasonication creating cavitation bubbles that are used to overcome the van der Waals force maintaining the layered materials stacked together in the bulk form. During sonication in liquids, the propagation of high amplitude pressure waves generate molecular dissociation, void creation and the formation of bubbles. The implosion of those bubbles can produce local temperatures of several thousands Kelvin and pressures of hundreds of atmospheres [105]. These effects result in exfoliation of the layered materials and, at the same time, tearing them into smaller nanosheets in lateral size [106], as seen in Figure 2.4.

Liquid processing was used routinely in the 2000s for dispersing graphene oxide (GO), followed by a reduction step [107, 108]. However, the oxidation process introduces defects that even annealing at 1100°C does not remove the functional groups completely [109, 110]. Around the same time, carbon nanotubes were successfully debundled in different organic solvents using ultrasonication [111, 112, 113, 114].

The next logical step was developed independently by different research groups, achieving direct exfoliation of graphite to graphene nanosheets in high boiling point solvents [42, 115]. Research was further developed by introducing the use of surfactants [116] or polymers [117] to stabilize the nanosheets in water-based dispersions.

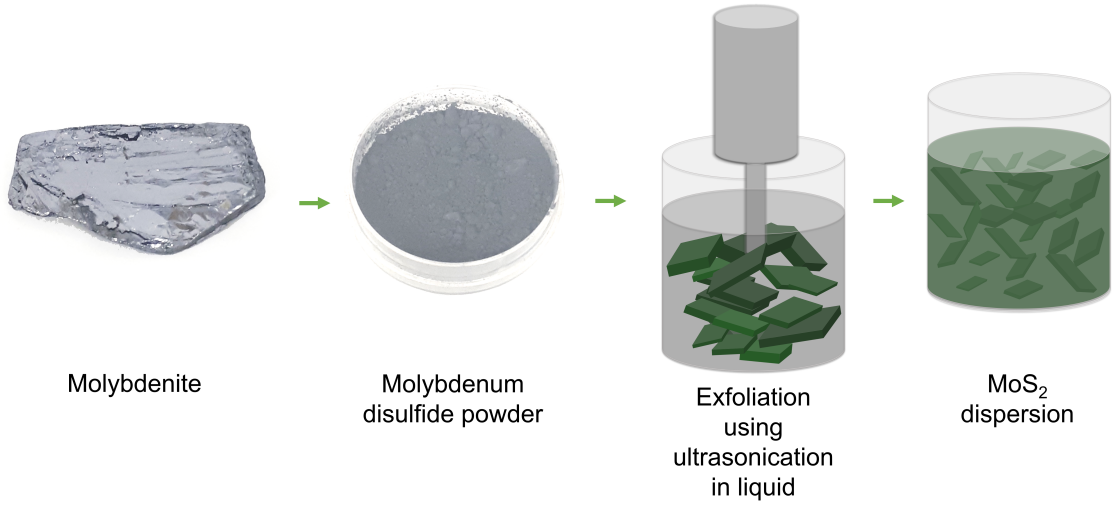

Figure 2.4: A diagram of liquid phase exfoliation process. The steps are illustrated, starting from the mineral molybdenite and resulting in a dispersion of exfoliated nanosheets in the desired solvent. Diagram shows molybdenum disulfide but the process is similar for other layered materials.

Coleman *et al.* [43] introduced a further understanding about LPE by demonstrating the exfoliation of various layered materials in different organic solvents. The choice of solvent that yields high quality dispersions uses the Hansen solubility parameter framework, which effectively describes the interactions between layered materials and solvents [46, 118]. This formalism predicts high exfoliation yields and good dispersion stability if there is close matching of the solubility parameters of the solvent and the layered material [119]. As such, Hansen solubility parameter analysis makes it possible to develop liquid phase methods to disperse and process various layered materials in a general and reproducible way.

The framework was first proposed to understand the solubility of polymers, for which it has proven effective. Hansen expanded Hildebrand's formalism for solubility of polymers in solvents. Both frameworks are based on the Flory-Huggins theory, which introduced a parameter (χ) in the calculation of Gibbs free energy of mixing considering the interaction energy between the polymer and the solvent molecules [120].

Hildebrand proposed a solubility parameter defined as the square root of the cohesive energy density of the solvent [121]:

$$\delta = \sqrt{\frac{E}{V}}, \tag{2.2}$$

where E is the energy of vaporization and V is the molar volume.

Charles Hansen extended this solubility formalism by hypothesising that the cohesive energy density can be resolved into a sum of contributions from three classes of intermolecular interactions [122]. The Hildebrand solubility parameter is therefore written as:

$$\delta^2 = \delta_D^2 + \delta_P^2 + \delta_H^2, \tag{2.3}$$

where δ_D, δ_P and δ_H are the dispersive, polar and hydrogen bond components, respectively.

A simple method of visualisation for the framework is treating each component as a coordinate in a three-dimensional space. A distance defined between two points in this space describes the likelihood of two materials being miscible. The solubility increases with the decreasing of distance, as it means a smaller combinatorial free energy change. The mathematical expression for this distance (R_A) is:

$$R_A = \sqrt{4(\delta_D^{(A)} - \delta_D^{(B)})^2 + (\delta_P^{(A)} - \delta_P^{(B)})^2 + (\delta_H^{(A)} - \delta_H^{(B)})^2} \tag{2.4}$$

where (A) and (B) represent the materials in question. The constant multiplying the term related to the dispersive component allows for spherical plots in the referred space.

The optimisation of parameters for ultrasonic exfoliation is well developed [123, 124, 125], as opposed to detailed studies about the mechanisms [126]. Mainly, a comprehensive link between the geometry of vials with dispersion yield and quality is still missing. Also, the exact output power applied to the nanosheets during exfoliation is unknown [127].

High-pressure homogenisation

LPE is a process that can be scaled up to industry levels and fulfil the demand for nanomaterials, especially in future electronic and manufacturing applications. Ultrasonic-

ation, high-shear mixing [128, 129] and homogenisation [130, 131, 132] are options for producing large quantities of high quality nanosheets.

The homogeniser system shown in Figure 2.5 generates pressures up to 3000 atm using a hydraulic system to move an intensifier pump. The compressed dispersion is depressurised through a diamond nozzle, which produces a high velocity fluid jet. This jet strikes the fluid flowing in the reverse direction in the process cell, creating turbulent shear forces that exfoliate the bulk layered materials. The turbulent flow generates a significant amount of heat within the system, making it necessary to use an external chiller system to keep a constant temperature during the process (since temperature is one of the parameters that affects exfoliation yield) [133].

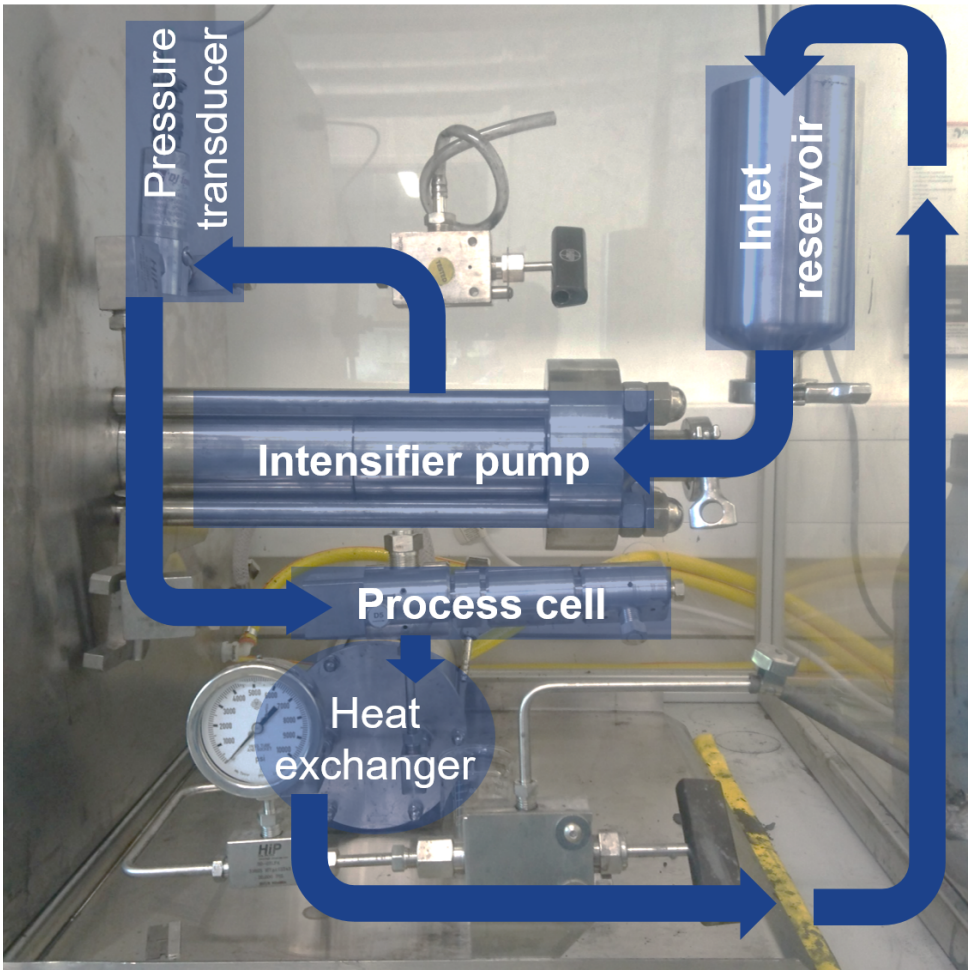

Figure 2.5: A diagram of the high-pressure homogenisation process. Image from Large *et al.* [3].

2.3.3 Other exfoliation and production techniques

There are other exfoliation and synthesis techniques beyond LPE that have potential to be scaled-up. Electrochemical exfoliation (ECE) is one example. Resulting sheets are larger than LPE nanosheets but more defective [134, 135, 136]. Functionalisation can be achieved easily as part of the exfoliation process. The experimental setup includes a working electrode that will be exfoliated, a counter electrode, and a reference electrode immersed in the electrolyte containing ions that intercalate the bulk material [137]. The exfoliation mechanism depends on the potential applied to the working electrode. An anodic exfoliation involves the intercalation of anions, whilst a cathodic exfoliation, involves cations. Both increase the interlayer spacing between the sheets in the bulk form, facilitating a subsequent exfoliation process [137]. Intercalation of ions in graphite under bias is known since the 19th century but the process works for other materials as well [138].

Chemical vapour deposition (CVD) is another technique that can be scaled-up [139, 140, 141]. Layered materials can be synthesised over large areas by exposing the substrate to volatile materials under vacuum and high temperatures. The process is more expensive than LPE and requires a transfer step between substrates, creating defects or producing residues [127]. Also, for monolayer MoS_2, it was shown that the strain induced during growth affects the optical properties of the material [142].

Thermally assisted conversion can also produce materials at industry-scales. TMDs can be produced by sulfurisation or selenisation of metal layers deposited on quartz substrates. A thermal treatment is applied to the transition metal layer while the chalcogen powder is melted in a second area. This method can produce not only the 2H polytype but also the 1T' [143].

Chapter 3

Processing and characterisation techniques

The emerging properties of few-layered nanomaterials require a good degree of exfoliation. This chapter describes the experimental details of the processing techniques used in this thesis for exfoliation of nanomaterials. Also, an overview of the characterisation techniques used and the information that can be obtained from each one of them is provided. This follows the motivation related to standardisation of reliable and reproducible characterisation of nanomaterials.

3.1 Materials production

3.1.1 Mechanical exfoliation

For Chapter 5 and 6, mechanically-exfoliated MoS_2 sheets were produced using a variation on the Scotch tape method. A natural bulk MoS_2 crystal (CrystalAge.com) was pressed into contact with 3M Scotch Magic tape and peeled. In a second step, clean tape was pressed into contact with the peeled material and removed to exfoliate the MoS_2 layers; this was repeated up to 6 times, using fresh tape each time. The exfoliated MoS_2 was transferred from the tape to an intermediate PDMS transfer substrate (QSil 216, Farnell) which was cast against a glass surface and cured at 140 °C prior to the transfer. To transfer

the exfoliated MoS_2, the cast surface of the PDMS was peeled off from the glass and pressed into contact with the tape, and heated at 120 °C on a hotplate under moderate pressure for 2-3 min. The tape was removed while heat was applied to maximise transfer of the exfoliated MoS_2, and minimise transfer of tape adhesive residue. The same heating-pressure-lifting step was used to transfer the exfoliated MoS_2 off of the PDMS transfer substrate onto the final target substrate (Si wafer or Si with a 300-nm layer of the thermal oxide SiO_2). Figure 3.1 shows an optical micrograph of a typical sample where the region containing a monolayer is highlighted.

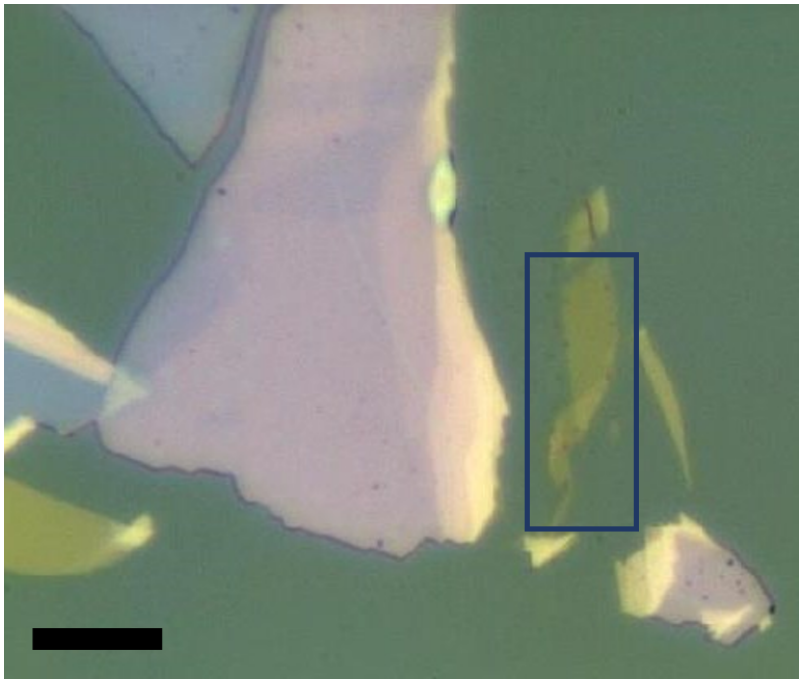

Figure 3.1: Mechanically exfoliated MoS_2 nanosheets on Si/SiO_2 substrate; a monolayer is highlighted. The layer number was identified by a combination of characterisation techniques: Raman spectroscopic metric and topography from atomic force micrographs. Scale bar is 10 µm

3.1.2 Liquid-phase exfoliation

For Chapter 4, the dispersion of MoS_2 bulk powder (Aldrich Chemistry) at initial concentration of 20 g L^{-1} (80 mL of total volume) was probe sonicated using the Sonics Vibracell VCX750 and the 1/2-inch (13 mm) tip for 1 h at 60% amplitude. The resulting dispersion was centrifuged for 30 min at 5000 g. The supernatant was discarded and

the sediment was redispersed into 80 mL of acetone (VWR Chemicals) or IPA (Fisher Chemical), as received. The dispersion was probe sonicated for 5 h at 60% amplitude, pulsed 6 s on and 2 s off. It was then centrifuged for 5 min at 5000 *g*. The supernatant was collected for further characterisation.

For the sonication time study in Chapter 4, a MoS_2 dispersion in acetone was prepared at the same initial concentration of 20 g L^{-1} but with total volume of 50 mL. It was probe sonicated using a Sonics Vibracell VCX130 with 1/4-inch (6.3 mm) tip for 1 h at 60% amplitude and centrifuged for 30 min at 5000 *g*. The supernatant was discarded and the sediment redispersed into 50 mL of acetone. The dispersion was sonicated at 60% amplitude for times ranging between 30 min and 8 h. Samples of 5 mL were collected every 30 min up until 3 h and then every hour. Fresh solvent was added to keep the total volume constant during sonication. Every sample was centrifuged for 5 min at 5000 *g* and the resulting supernatant was further characterised.

In order to measure the Hansen and Hildebrand solubility parameters (Chapter 4) for acetone-exfoliated MoS_2, a total of 10 samples were prepared by centrifuging 2 mL of the the dispersion using Beckman Coulter Optima TLX ultracentrifuge at 70,000 rpm (265,070 *g*) for 20 min. Additional 10 samples were prepared by redispersing the sediment from the initial centrifugation step during preparation in fresh acetone and centrifuging them in the ultracentrifuge for 5 minutes at 5,000 rpm (1,350 *g*). For both sets of centrifuge tubes the supernatant was discarded and 2 mL of solvent was added to each tube: n-pentane, ethanol, toluene, tetrahydrofuran, acetone, *N*-methyl-2-pyrrolidone, methanol (VWR Chemicals), cyclopentanone, 1-cyclohexyl-2-pyrrolidone (Aldrich Chemistry) and isopropanol (Fisher Chemical). Each sample was sonicated for 10 seconds at 30% amplitude using Sonics Vibracell VCX130 with 1/4-inch (6.3 mm) tip to redisperse the sediment into each solvent. These samples represent identical dispersions of particles (either exfoliated MoS_2 or bulk MoS_2) in different solvents of known solubility parameters. The stable concentrations achieved after a period of sedimentation allow the corresponding parameters of the particulates to be estimated.

For Chapter 5 and Chapter 6, graphite powder (Zenyatta Ventures Ltd.) at initial concentration of 25 g L^{-1} (20 mL total volume) was dispersed in cyclohexanone (Sigma Aldrich) and probe sonicated using the Sonics Vibracell VCX-130 and the 1/2 inch (13 mm) tip for 3 h at 60% amplitude. The resulting dispersion was centrifuged for 30 min at 5000 *g*. Supernatant was collected for further characterisation.

High-pressure homogenisation

Homogenisation of MoS_2 surfactant dispersions was performed using a BEE International Mini DeBEE high-pressure homogeniser, with a D5 diamond nozzle (∼200 µm aperture), in a reverse flow configuration. The system heat exchanger was connected to an Applied Thermal Control Ltd K4 4.5 kW recirculating chiller, with temperature control between 5 and 35 °C. During processing the thermal set point of the system was maintained to within 0.5 °C. Discussion of this process is given in full by Large *et al.* [3].

Liquid cascade centrifugation

Liquid phase exfoliation produces nanosheets with a broad distribution of size and thickness. One method for selecting narrow fractions of these distributions is known as liquid cascade centrifugation (LCC). It consists in submitting the dispersion to successive centrifugation steps gradually increasing the product of relative *g*-force by time, yielding smaller and thinner nanosheets [106, 47, 45, 144].

For Chapters 5 and 6, the homogenised MoS_2 dispersion in aqueous non-ionic surfactant (Triton™ X-100, TX-100) was submitted to an initial centrifugation step at 3000 *g* for 5 min to remove any unexfoliated material. The supernatant was used to start the cascade. The dispersion was centrifuged at relative *g*-force of 3000 *g* for 9 min. The resulting sediment was redispersed in TX-100 at a concentration of 0.5 g L^{-1} and the procedure was repeated using the supernatant to select narrow size distributions for subsequent 12 min, 14 min, 20 min, 40 min, 1 h, 2 h, 4 h, 8 h, and 12 h steps to produce the samples. The samples are always referred to using the time of centrifugation for the step which sedimented them, since relative *g*-force was kept constant.

3.2 Characterisation techniques

3.2.1 Raman spectroscopy

When electromagnetic radiation interacts with a sample, it might be absorbed by it if the radiation energy is equal to the separation between two electronic energy levels. Otherwise, the incident radiation suffers elastic scattering, resulting in no changes to its wavelength. Lord Rayleigh showed in 1871 that the intensity of this scattered light is inversely proportional to the fourth power of the wavelength ($I_s \sim \lambda^{-4}$), therefore this radiation is known as Rayleigh scattering [86].

The Raman effect was discovered by Sir Chandrasekhara Venkata Raman (1928) and independently by Leonid Mandelstam and Grigory Landsberg (1928). It was predicted theoretically by Adolf Smekal (1923) and by Hendrik Kramers and Werner Heinsenberg (1925) [68]. Raman won the 1930 Nobel Prize in physics for his discovery. He showed experimentally that the scattering produced when a monochromatic light interacts with different liquids and gases consists of a scattered radiation with the same wavelength as the incident light with fraction of radiation with modified frequency [145]. If the scattered photon has less energy than the incident radiation, it is called Stokes scattering. If there is an increase in photon energy, it is anti-Stokes scattering.

Figure 3.2 shows a diagram of the different types of scattering. The elastic scattering is much more intense than the inelastic Raman scattering, approximately by a factor of 10^8 [146], therefore good detectors and filters to remove the Rayleigh scattering are necessary for this characterisation technique. The anti-Stokes scattering is less intense than Stokes due to the differences in states population defined by a Maxwell-Boltzmann distribution, which is temperature dependent, with more anti-Stokes scattering at higher temperatures [146]. Also, the Raman effect is observed more easily if the light source is highly monochromatic, which can be achieved with special filters or more commonly by using lasers.

Polarisability, α, is the physical quantity that relates to the response to incident radiation in the form of scattering. It is a measure of the electrons displacement in relation to the

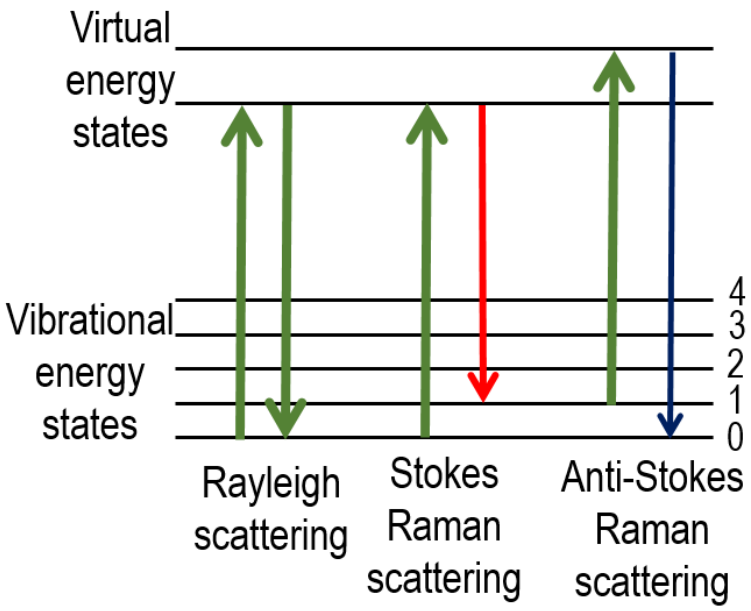

Figure 3.2: Diagram of Rayleigh and Raman scattering in terms of initial and final energy states. Rayleigh is an elastic scattering, meaning the incident light has no energy modification after interacting with the material. Stokes Raman scattering results in an energy transfer to the material, whilst the opposite effect is the anti-Stokes scattering.

nuclei and in general, it is an anisotropic property, depending on the molecule symmetry. A visual representation is an ellipsoid drawn using $\alpha_{x,y\,or\,z}^{-1/2}$, the x-, y-, and z-components of the polarisability as the axis length in the respective direction. This ellipsoid has elliptical cross-sections in each plane. Each one of this components is an element of a matrix, since polarisability transforms as a tensor. This matrix is represented as:

$$\alpha = \begin{pmatrix} \alpha_{xx} & \alpha_{xy} & \alpha_{xz} \\ \alpha_{yx} & \alpha_{yy} & \alpha_{yz} \\ \alpha_{zx} & \alpha_{zy} & \alpha_{zz} \end{pmatrix} \tag{3.1}$$

However, by the cross-section definition, $\alpha_{yx} = \alpha_{xy}$, $\alpha_{zx} = \alpha_{xz}$, and $\alpha_{yz} = \alpha_{zy}$. Therefore, there are only six components of the polarisability tensor: α_{xx}, α_{yy}, α_{zz} (the values along the axes), α_{xy}, α_{xz}, and α_{yz}.

When monochromatic radiation interacts with the sample and it is not absorbed by it, the electric field ($\vec{E}$) induces an electric dipole ($\vec{\mu}$) correlated numerically using polarisabilty [86]:

$$\vec{\mu} = \alpha\vec{E} \tag{3.2}$$

For classical systems, the difference between the incident and scattered radiation frequency can assume any value, however in quantum mechanical systems, those values are discretised, resulting in selection rules for allowed transitions.

Raman spectroscopy can be purely rotational, pure vibrational or combination of both. For rotational spectroscopy, the polarisability of the molecule should change as it rotates in an electric field. For diatomic molecules, the selection rule for angular momentum is given by $\Delta J = 0, \pm 2$. The $\Delta J = 0$ corresponds to Rayleigh line, whilst $\Delta J = 2$ corresponds to the Stokes line and the $\Delta J = -2$ corresponds to the anti-Stokes line. For the active modes in vibrational Raman spectroscopy, the polarisability of the molecule should change as it vibrates. The selection rule is for the wavenumber difference is $\Delta\nu = \pm 1$, where the $\Delta\nu = 1$ corresponds to Stokes lines and the $\Delta\nu = -1$ corresponds to anti-Stokes lines. Overtone transitions are also allowed $\Delta\nu = \pm 2, \pm 3, \ldots$ but are usually weaker. In addition to this, combination modes, involving transitions to vibrationally excited states are possible [86]. A complementary characterisation technique is infrared spectroscopy, which requires a change of dipole moment in the molecule when light is absorbed. The rule of mutual exclusion states that no normal modes can be both infrared and Raman active in a molecule that possesses a centre of symmetry, but there are exceptions to this rule [147].

For linear molecules, there are $3N-5$ normal vibrations, whilst there are $3N-6$ for a non-linear molecule, where N is the number of atoms in the molecule. These rules can be used to calculate the number of modes observed for each symmetry species of the point group that the molecules belongs. For crystalline solids with an unit cell containing N atoms, there are $3N$ degrees of freedom; three are acoustic and $3N-3$ are optical phonons [98]. Figure 3.3 compares the phonon dispersion curves for monolayer and bulk MoS_2 (image from Molina-Sanchéz and Wirtz [4]). For MoS_2 with even numbers of layers (or

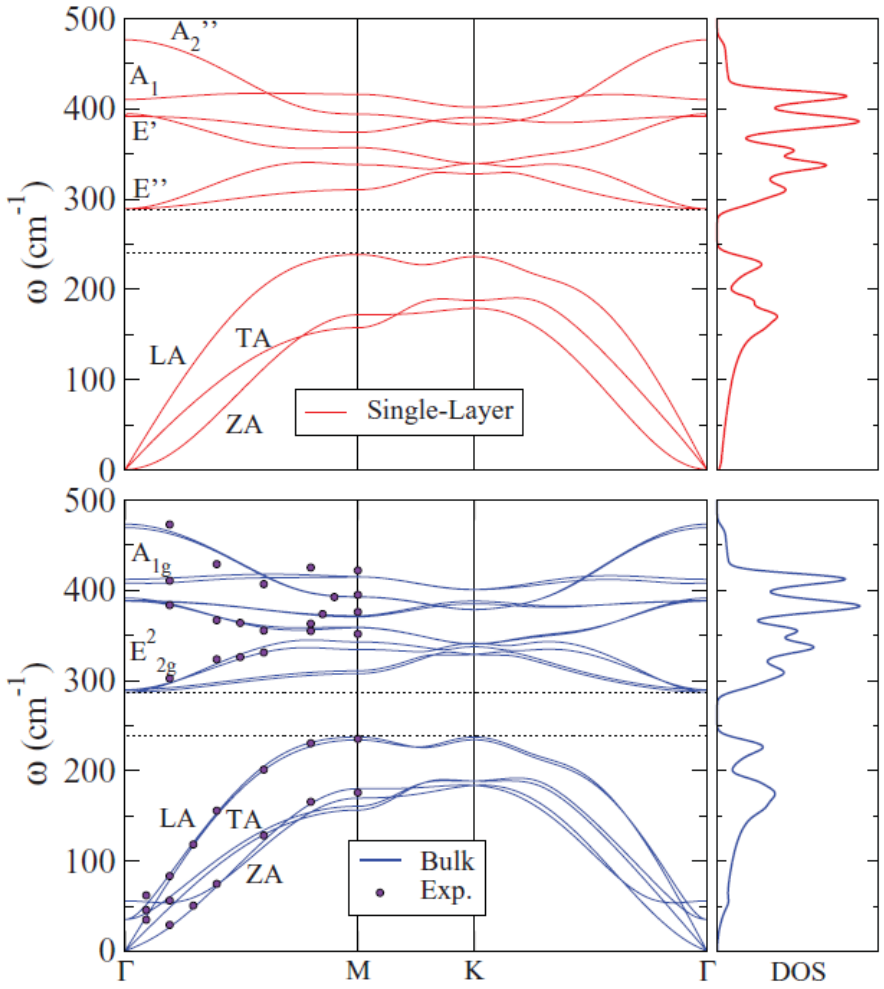

Figure 3.3: Phonon dispersion curves and density of states for monolayer and bulk MoS_2. Image from Molina-Sanchéz and Wirtz [4].

bulk) have a symmetry similar to the D_{6h} point group, and systems with odd numbers of layers (monolayer) have D_{3h} space group symmetry [148]. Point group is the group composed of every symmetry operation applied to a pattern keeping at least one fixed point, including rotational and also translational operations for crystals. There is a total of 32 crystallographic point groups [68]. The point group D_{nh} means there is a C_n axis and n C_2 axes perpendicular to the first one and at equal angles to each other and a σ_h symmetry plane and n other σ planes [86].

Bulk 2H-MoS_2 has four first-order Raman active modes and two IR-active modes (A_{2u} and E_{1u}) [22]. The Raman modes are represented according to the notation for the D_{6h} group: A_{1g}, E_{1g}, E^1_{2g}, and E^2_{2g}. The first three correspond to the A'_1, E', E'' modes of the

monolayer, respectively. The E^2_{2g} mode is not observed for monolayers as it is the vibration of adjacent rigid layers with respect to each other. The A'_1 mode is one out-of-plane vibration where the metal atom is stationary and the chalcogen atoms of the upper layer vibrate in-phase and opposite direction to the lower layer. Both E′ and E″ modes are in-plane vibrations. For the first one, the metal and chalcogen atoms vibrate in-phase and opposite direction. For the E″ mode, the non-zero elements of the Raman tensor are quadratic functions of xz and yz. This mode is not observed experimentally because of the relative orientation detectors, sample, and incident laser are arranged (laser perpendicular to xy-plane) [67]. Even for monolayer spectra, the modes are usually referred to using the notation for bulk MoS_2.

Figure 3.3 also shows the phonon density of states (DOS) for monolayer and bulk MoS_2 [4]. This quantity measures the number of states within a determine energy level [149, 68]. The measured Raman intensity increases for frequencies with a higher phonon DOS, as the likehood of Raman scattering is given by how many phonons and photons there are for that specific energy. Spectroscopic techniques, in principle, can only quantify optical phonons close to the Brillouin zone centre (wavevector $q \sim 0$). This selection rule is a consequence of the infinite periodicity of the crystal. This rule is relaxed due to confinement effects related to size, as observed for nanomaterials [150].

In non-resonant Raman spectroscopy, the intensities are proportional to the intensity of the incident light, proportional to the fourth power of the frequency of the light, and proportional to the square of the polarisability tensor. However, when the incident laser radiation has similar energy to a permitted electronic transition, the resonant Raman signal is increased by about five orders of magnitude [151, 146]. For resonance involving a transition from the ground state to the first excited state, combination modes, overtones of the active modes and modes from different points (other than Γ point) are enhanced [152].

Experimental details for Raman spectroscopy measurements are discussed in the relevant Chapters (5 and 6). Laser damage study was performed on mechanically-exfoliated MoS_2 using a 660 nm laser. Power applied to the sample was 22 mW for 1 s through a

100x objective. Exposure to high power induces heating, leading to higher surface atom mobility and therefore enhances defect mobility and oxidation rates at edges and defect sites [153, 154, 155]. Also, an experiment of electrochemical oxidation of ME sheets was performed. Applying a potential beyond the stability window for the electrolyte causes electrolysis, with the radicals produced being able to etch the edges of the sheets [156]. The ME sheets were exfoliated using the Scotch tape method and transferred to a gold substrate, covered in ionic liquid (lithium perchlorate dissolved in ethylene glycol) and a voltage of 3.0 V was applied to the sample.

3.2.2 UV-visible spectroscopy

UV-visible spectroscopy (UV-vis) is the measurement of the optical extinction or transmission as a function of wavelength in the visible and ultra-violet range. Extinction is a sum of the sample's absorption and scattering [157]. Typically, spectra are measured between 200 and 800 nm, even though UV-vis-NIR spectrophotometers have a much larger range, reaching about 3200 nm, such as the Shimadzu UV-3600 Plus spectrophotometer used for Chapters 4 and 6. Spectra of the dispersions were measured in quartz cuvettes (Starna Scientific).

A broadband monochromated light source path is split between two paths: a sample and a reference paths [158]. The intensity of both paths is measured and the ratio can be related to transmittance (T) and the extinction (Ext) as follows:

$$\text{Ext} = -\log T = -\log\left(\frac{I}{I_0}\right) \tag{3.3}$$

where I is the sample intensity and I_0 is the reference. Absorbance, in the absence of scattering, or extinction can be used to calculated the concentration, according to Beer-Lambert law.

$$\text{Ext} = \varepsilon C l \tag{3.4}$$

where ε is the extinction coefficient and l is the path length through the cuvette.

UV-vis spectroscopy also provides information about electronic transitions in the samples in the form of exciton peaks. The electrical neutral exciton is defined as a bound state of an electron and a hole which are attracted to each other by the electrostatic Coulomb force [68]. In particular, for semiconductors, the position and intensities of the excitons absorptions can be developed into metrics for both layer number and nanosheet size, when properly calibrated with microscopic techniques [64, 6, 159, 160].

3.2.3 X-ray photoelectron spectroscopy

X-ray photoelectron spectroscopy (XPS) is a chemical characterisation technique based on the photoelectric effect. The phenomenon consists of the ejection of an electron by a material when exposed to electromagnetic radiation [68]. The binding energy (E_B) of a core-level electron emitted from the material is determined by conservation of energy as follows:

$$E_B = h\nu - E_K - \phi \tag{3.5}$$

where $h\nu$ is the energy of the X-ray photons, E_K is the kinetic energy of the ejected photoelectrons, measured by the spectrometer of total work function ϕ [161]. Work function is the difference in potential energy of an electron between the vacuum level and the Fermi level, therefore, the amount of energy required by an electron to escape the surface of the material [89]. This work function has contributions from the sample and also from the spectrometer [162].

If a X-ray photon interacts with a material with energy higher than the binding energy of a core level electron, it ejects it from the sample. The spectrometer measures the kinetic energy of these ejected photoelectrons. The energy is characteristic of the orbital from which the photoelectron originated. A sample can be easily identified by survey scans, a low resolution scan over a broad binding energy range. High resolution spectra over specific regions associated with peak fitting provide more detailed information regarding oxidation states and atomic percentages. Advanced modes such as angle-resolved or imaging XPS can determine the atomic distribution with spatial resolution [161]. For

example, for MoS_2, analysis of atomic percentages of molybdenum, sulfur, and oxygen atoms can provide information about defects and also different functionalisations of the nanosheets [163, 164].

XPS was used in Chapter 4 and analysis was carried out using an ESCALAB 250 Xi system (Thermo Scientific) at the University of Brighton by Dr Santanu Ray. The spectrometer is equipped with a monochromated Al K_α X-ray source. Uniform charge neutralization was provided by multi-mode electrostatic flood source. The standard analysis spot of *ca.* 900 µm by 900 µm was defined by the microfocused X-ray source. Full survey scans (step size 1 eV, pass energy 150 eV, dwell time 50 ms and 5 scans) and narrow scans (step size 0.1 eV, pass energy 20 eV, dwell time 100 ms and 15 scans) of the Mo3d (binding energy, BE∼229 eV), S2p (binding energy, BE∼162 eV), C1s (BE∼285 eV) and O1s (BE∼531 eV) were acquired from four separate regions on each sample. Data were analysed using Thermo Avantage Software (Version 5.952) using a smart background.

3.2.4 Atomic force microscopy

Atomic force microscopy (AFM) is part of the scanning probe microscopy group. Its main advantage is giving a 3D topographical surface information with high resolution [165]. As shown in Figure 3.4, a sharp tip, with a radius of a few nanometres, is at the extremity of a cantilever. When the tip is in close proximity to the sample, they interact and the resulting attractive or repulsive force causes deflections of the cantilever [166]. The magnitude of these deflections are estimated by the reflection of a laser source on a spatially-resolved photodiode. In association with a calibrated piezoelectric sensor in the cantilever, precise measurements of height are possible.

Contact AFM might not be appropriate for some samples, especially soft materials, due to damage caused by the measurement. Tapping mode is the alternative. In this mode, the cantilever oscillates at its resonant frequency and the phase shift caused by the interaction with the sample is the quantity measured. The precalibrated PeakForce QNM® (Quantitative Nanomechanical Mapping) mode used in the Bruker Dimension Icon instrument provides additional properties about the sample from the force-distance

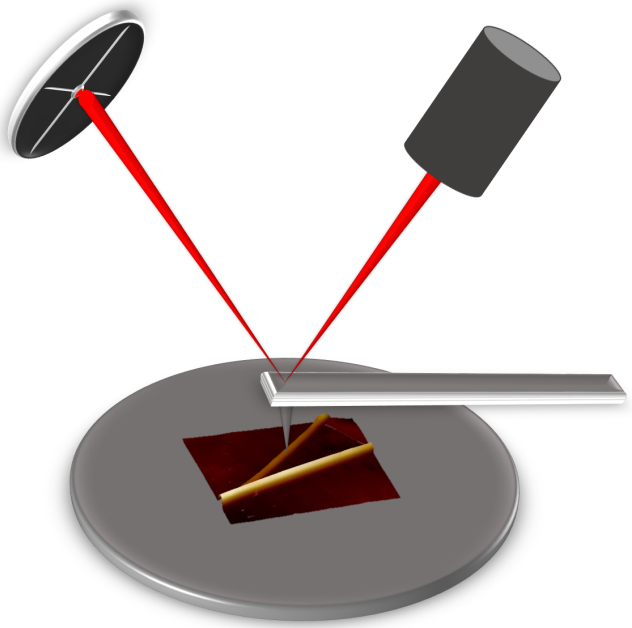

Figure 3.4: A diagram of a typical AFM setup, showing the laser path from the source to the photo diode after reflecting on the cantilever attached to the tip interacting with the sample.

curve, such as adhesion, Young's modulus, dissipation and deformation (shown in Figure 3.5), while simultaneously imaging the sample topography. This method is based on an off-resonance oscillation of the cantilever, in contrast to typical tapping mode.

For AFM characterisation on Chapters 4, 5, and 6, the Dimension Icon system from Bruker operating in the QNM mode was used. The probe used was a ScanAsyst Air tip whose spring constant is $0.4\,\mathrm{N\,m^{-1}}$. The sample was prepared drop casting the dispersions on silicon wafer. The wafer was heated above the boiling point of water to remove any residual solvent in the analysed sample, and to prevent re-aggregation of the nanosheets during drying.

AFM thicknesses were converted to nanosheet layer number by following an established methodology [6, 125]. Each flake height was measured and plotted with all measurements arranged in ascending order. The first plateau in the data indicates the thickness of the monolayer. The difference between subsequent plateaux positions indicate the interlayer spacing.

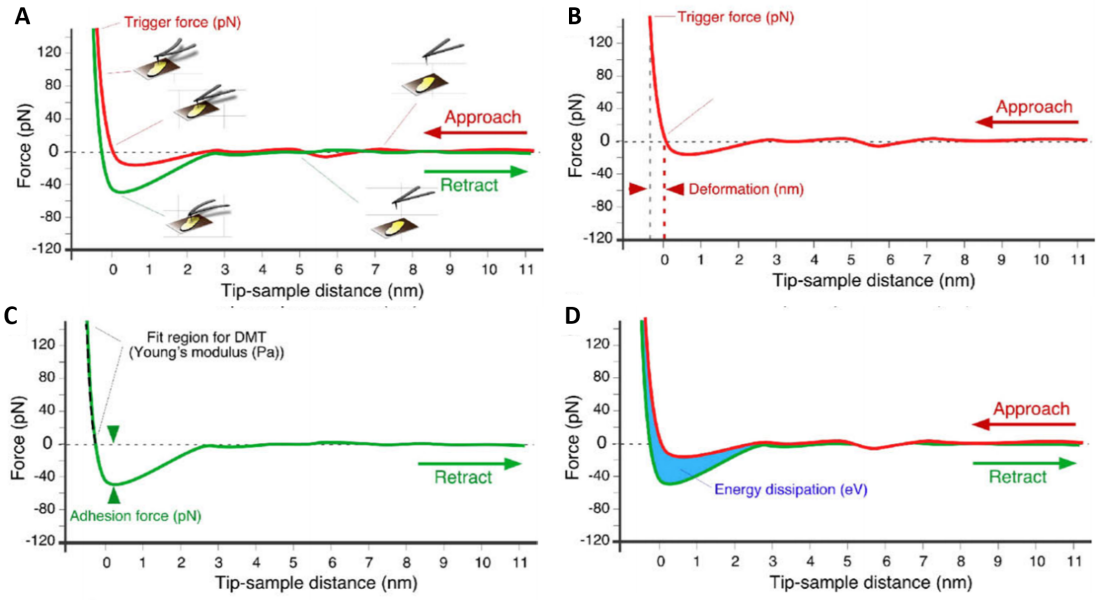

Figure 3.5: **A:** Typical force-distance curve. The tip approaches the surface, until contact is made. Pressing the sample increases the force and deflects the cantilever. Once force reaches the trigger force set, the tip is withdrawn until it detaches from the sample and returns to initial position. **B:** Deformation caused by the tip to the sample is calculated from the approach curve. **C:** Adhesion force can be calculated from the retract curve. The region of positive force is fitted using the Derjaguin, Muller and Toporov model (DMT) to determine the Young's modulus. **D:** The area difference between the approach and retraction curves are used to calculate the energy dissipation. Image adapted from Medalsy *et al.* [5].

3.2.5 Electron microscopy

Optical microscopes work by detecting electromagnetic waves of a determined wavelength scattered by the sample and focussed by glass lenses. Electron microscopes use a similar principle in the sense that electrons are scattered and focussed by electrostatic or magnetic lenses. An advantage of using electrons is that tuning their energy to smaller wavelengths, the resolution can be increased. The interaction between the electrons and the sample can result in back scattering, production of Auger electrons, secondary electrons, and X-rays [158].

There are two main types of electron microscopes: scanning electron microscope (SEM) and transmission electron microscope (TEM). The first one, uses primary and secondary backscattered electrons for imaging, whilst the other uses electrons transmitted through the sample. As a consequence from these definitions, SEM can only image the

surface of thick samples and TEM needs thin samples. Both are less time-consuming when compared to scanning probe microscopy. However, obtaining information about thickness can be challenging and only possible for specific samples. Also, electron microscopes work under vacuum which is not appropriate for more fragile samples, especially biological specimens. Another disadvantage of SEM is that insulating samples accumulate charges during analysis, resulting in blurred images. One solution is coating them with a thin metal film, like gold or platinum.

In addition to micrographs, electron microscopes can be used to determine the composition of samples by analysing energies and intensities of characteristic X-rays produced when high energy electrons strike the sample. TEM operates at higher energy than SEM so it can achieve a resolution of less than one nanometer. TEM can also obtain diffraction patterns from the sample, enabling an analysis of the crystal structure.

Micrographs (Chapter 4) were taken by Dr Aleksey Shmeliov at Trinity College Dublin using FEI Titan 80 – 300 scanning transmission electron microscope (STEM) operating at 300 kV. The samples were deposited onto ultrathin carbon grid (standard lacey with 2 nm film on the top). Fast Fourier transform pattern was created using the ImageJ software.

Electron energy loss spectroscopy

Electron energy loss spectrometry (EELS) analyses the energy distribution of electrons with known kinetic energy that interacted with the sample. Some electrons suffer inelastic collisions and lose energy. By evaluating the energy loss, it is possible to determine chemistry and electronic structure.

A spectrum is split into two different regions: a low-loss and a high-loss region, where the arbitrary value of $\sim$50 eV divides them. The first region contains information about the weakly bound conduction and valence-band electrons, whilst the second is about the tightly bound core-shell electrons, bonds and atomic distributions. EELS can quantify every element in the periodic table but especially light elements. Additionally, it has good spatial resolution, allowing for atomic maps to be made. The disadvantages of this technique are

that very thin samples are necessary, as the electrons are analysed after going through the material, and a correct analysis is challenging [167].

The scanning transmission electron microscopy (STEM) imaging studies were performed at University of Zaragoza by Dr Raul Arenal on probe-corrected FEI Titan Low-Base 60-300 microscope operating at 200 kV (fitted with a X-FEG® gun, a Cs-probe corrector, CESCOR from CEOS GmbH). EEL spectra were recorded using the spectrum-imaging (SPIM in 2D or spectrum-line (SPLI) in 1D) mode in a Gatan GIF Tridiem ESR 865 spectrometer. The convergent semi-angle was of 25 mrad, the collection semi-angle was of 80 mrad and the energy resolution $\sim$ 1.0 eV. The EEL spectra were denoised with the open-source program Hyperspy by using principal component analysis routines.

3.2.6 Dynamic light scattering and zeta potential

Dynamic light scattering (DLS) measures the intensity distribution of light scattered by the sample undergoing Brownian motion in a liquid as a function of time [168]. Through specific algorithms, the software converts between the scattering events and the relative intensity of light scattered by particles of a given size. The output measurement is the hydrodynamic radius, a static fluid layer surrounding the particle [169]. Lotya *et al.* [170] studied the empirical conversion between this hydrodynamic radius (a_{DLS}, defined for spherical particles) and the average length of a nanosheet:

$$\langle L \rangle = 0.07 a_{\mathrm{DLS}}^{1.5} \tag{3.6}$$

The equation agrees well with experimental data, with large uncertainties for fitting parameters (0.07 ± 0.03 and 1.50 ± 0.15), and follows the expected scaling obtained by treating the nanosheets as discs, even though it assumes different materials will produce the same light scattering, only dependent on the nanosheet length. Also, the dimensions were measured using TEM micrographs, therefore any influence thickness might have on the measurement is neglected. The relationship is a good indication for preliminary measurements of nanosheet length. Particle size (Chapters 4 and 6) was determined using the Anton Paar Litesizer 500 with a 658 nm laser (40 mW).

Zeta potential was measured in the same AntonPaar Litesizer 500 particle analyser, for Chapter 4. In a colloidal dispersion or ionic solution, a phenomenon known as electrical double layer appears. The first layer is called the Stern layer. It consists of ions which are strongly bound to the surface of the particle. The second layer is made of ions attracted to the first layer by Couloumb force. Zeta potential is an electrostatic potential defined at the interface of this double layer as the difference between the stationary fluid surrounding the particle and the bulk fluid [171].

The instrument measures the electrophoretic mobility (μ) by determining drift velocity (v) in an applied electric field (E):

$$v = \mu E \tag{3.7}$$

Zeta potential can be calculated using Henry's equation:

$$\mu = \frac{2\varepsilon\zeta F(\kappa a)}{3\eta} \tag{3.8}$$

where ζ is the zeta potential, ε is the solvent dielectric permittivity, η is the solvent viscosity, and $F(\kappa a)$ is Henry's function, which varies between 1 and 3/2 according to the ratio of the particle size (a) to the Debye length ($1/\kappa$).

Henry's function is a constant for a given system. For small values of κa, the function is equal to 1, which is known as the Hückel approximation for non-polar systems. For large values of κa, the Smoluchowski approximation gives a function equal to 3/2, for ionic media [172]. Smoluchowski approximation for plate-like particle gives:

$$\zeta = \frac{\eta\mu}{\varepsilon} \tag{3.9}$$

This expression applies to plates with uniform surface charge large enough for the edge contributions to be neglected and radii much larger than the electrical double layer thickness. This quantity has been estimated around 20 nm for surfactant-exfoliated graphene nanosheets [173].

Measuring zeta potential is a direct indication of dispersion stability, since the electrostatic repulsion between the nanosheets prevents flocculation and precipitation in ionic dispersions for long periods of time [52].

Zeta potential was measured (Chapter 4) by diluting 10 µL of MoS_2/acetone dispersion in 350 mL of deionized water. A Thermo Scientific Barnstead MicroPure purification system was used to prepare ultrapure water (18.2 MΩ resistivity). A potential difference of 200 mV was applied to an Omega cuvette containing the sample during the measurement.

3.2.7 Electrochemical characterisation

An electrochemical cell can be used to either induce chemical reactions by an applied potential or to generate energy from those reactions. Possible applications of such phenomena are electrophoresis, electroplating of metals, sensors, batteries, and fuel cells. The most common configuration for this characterisation is a three-electrode system: a working, a reference, and a counter electrode. The sample is in contact with the working electrode exchanging electrons under an applied voltage. Chemically inert and conducting materials are usually used as the counter electrode (including noble metals such as gold and platinum). It balances the reaction and allows the measurement without compromising the reference electrode's stability. The reference electrode does not participate in the reaction but has a known reduction potential, allowing for a quantitative analysis [174]. Nanomaterials are particularly interesting for electrochemical characterisation since their physical and chemical properties differ from their respective bulk forms, especially due to the large surface area per mass, affecting its reactivity [175].

For Chapter 4, measurements were performed in a three-electrode configuration with a Gamry potentiostat. Glassy carbon electrodes were used as the working electrode (3 mm diameter, BASi), while platinum wire and Ag/AgCl (3M KCl) were used as the counter and the reference electrode, respectively. A total mass of 13.4 µg of MoS_2 exfoliated in acetone was deposited onto the glassy carbon electrode with an areal loading of 0.2 mg cm^{-2}. For comparison, the same mass of MoS_2 exfoliated in IPA was deposited in the same way. Linear sweep voltammetry experiments were performed with a scan rate of 5 mV s^{-1} from

0 V to -1 V (vs RHE, the reversible hydrogen electrode) in 0.5M H_2SO_4 to investigate the hydrogen evolution performance. The measured potential was converted to the RHE scale by adding 0.210 V, measured with respect to a Gaskatel Hydroflex H_2 reference electrode.

Chapter 4

Sonochemical edge functionalisation of molybdenum disulfide

Liquid-phase exfoliation (LPE) has been shown to be capable of producing large quantities of high-quality dispersions suitable for processing into subsequent applications. LPE typically requires surfactants for aqueous dispersions or organic solvents with high boiling point. However, they have major drawbacks such as toxicity, aggregation during solvent evaporation or the presence of residues. Here, dispersions of MoS_2 in acetone are prepared and show much higher concentration and stability than predicted by Hansen parameter analysis. Aiming to understand those enhanced properties, the nanosheets were characterised using UV-vis, zeta potential measurements, AFM, Raman spectroscopy, TEM, XPS and STEM combined with spatially-resolved EELS. Also, the performance of the MoS_2 nanosheets exfoliated in acetone was compared to those exfoliated in isopropanol as a catalyst for the hydrogen evolution reaction. The conclusion from the chemical characterisation was that MoS_2 nanosheets exfoliated in acetone have an oxygen edge functionalisation, in the form of molybdenum oxides, changing its interaction with solvents and explaining the observed high-quality and stability of the resulting dispersion in a low boiling point solvent. Exfoliation in acetone could potentially be applied as a pretreatment to modify the solubility of MoS_2 by edge functionalisation.

4.1 Introduction

The most common organic solvents for LPE have a high boiling point, based on the correlation between surface tension and solubility parameters through the cohesive energy density, as discussed in Chapter 2. However, high boiling point solvents produce an undesirable aggregation during deposition of thin films due to the slow evaporation [176]. Similarly, for fabrication of polymer composites, heat treatments above the boiling point of the solvent are usually required to remove them, which is impractical for several high boiling point solvents and incompatible with some polymers. Alternatively, surfactants in aqueous dispersions are used to achieve high concentrations and stable dispersions [45, 116]. While aqueous dispersions provide a lower boiling point alternative, it is difficult to remove any residual surfactant which may influence film or composite properties [56]. Other approaches such as washing with lower boiling point solvents are wasteful and may impact the properties of the produced structures [177]. A solvent exchange method has been used as a way of incorporating the advantages of low boiling point dispersions of layered materials with more effective exfoliating solvents [178]. While this provides a solution, it would be desirable to prepare dispersions in low boiling point solvents by direct exfoliation as a mean of reducing process complexity [56, 55].

4.2 Results and discussion

Acetone is an example of a desirable low boiling point solvent for LPE as it is readily available, has low toxicity and is widely used. As such, dispersions of molybdenum disulfide (MoS_2) in acetone were prepared and found to have concentration and stability much higher than expected, according to the standard Hansen parameter framework. Table 4.1 compares Hansen parameters of acetone and other conventionally used organic solvents [43] for LPE of MoS_2 (N-methyl-pyrrolidone and cyclopentanone), as well as Hansen interaction radius of those solvents with the nanomaterial. While the interaction radius for acetone is only $\sim 50\,\%$ greater than NMP and CPO, the attainable concentration exponentially decays with the square of the interaction radius [46]. Isopropanol (IPA) is

another low boiling point solvent that has been used before to exfoliate layered materials [43, 179, 180], despite it being poorly Hansen matched, as seen in Table 4.1. There is also a high mismatch between the surface tension of acetone ($23.4\,\mathrm{mN\,m^{-1}}$) and the value for solvents which produced maximum concentration dispersions of layered materials (around $40\,\mathrm{mN\,m^{-1}}$) [43].

Material	Dispersive component ($MPa^{1/2}$)	Polar component ($MPa^{1/2}$)	Hydrogen bond component ($MPa^{1/2}$)	Interaction radius to MoS_2 ($MPa^{1/2}$)
MoS_2	18.0	8.5	7.0	0
NMP	18.0	12.3	7.2	3.8
CPO	17.9	11.9	5.2	3.8
Acetone	15.5	10.4	7.0	5.4
IPA	15.8	6.1	16.4	10.7

Table 4.1: Hansen parameters for MoS_2 [44, 43] and different organic solvents: *N*-methylpyrrolidone (NMP), cyclopentanone (CPO), acetone and isopropanol (IPA) [122]. The last column contains the respective calculated interaction radius to the layered material.

Using metrics based on the extinction efficiency and confinement effects [6], it is possible to analyse the quality of the dispersion by estimating the concentration and the average layer number $\langle N \rangle$.

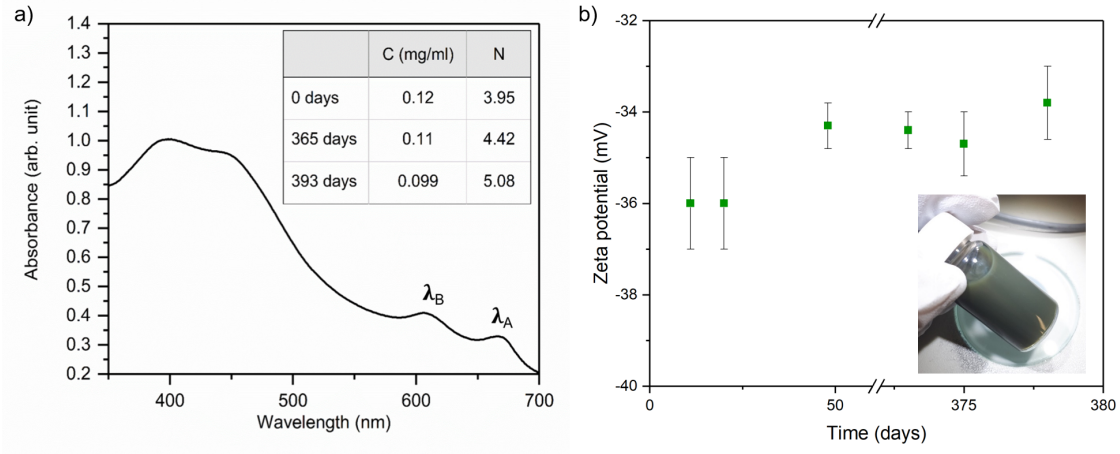

Figure 4.1: **A:** Representative extinction spectrum versus wavelength. The inset table contains the values for concentration (in $\mathrm{mg\,mL^{-1}}$) and layer number over time. **B:** Zeta potential data shows that the dispersion is stable ($\zeta > 30\,\mathrm{mV}$) for more than one year. A photograph of the high-quality dispersion is shown.

Figure 4.1A shows a typical extinction spectrum with the position of both A and B exciton absorptions of MoS_2 indicated. The A peak is related to a ground state exciton and

the B peak corresponds to a higher spin-orbit split transition between the valence band and the conduction band [181]. An inset table contains values of both estimated dispersion properties over one year. Concentration was found to be higher than 0.1 $mg\,mL^{-1}$ and the average layer number was estimated as approximately four. Both values are unexpected results for a low boiling point solvent with such a mismatch in the Hansen solubility parameters. Analysing the concentration and average layer number over a long time scale, it is inferred that the dispersion remains stable and the aggregation is minimal. Zeta potential measurements, shown in Figure 4.1B, corroborate the observed stability [116, 52, 173]. It is noted that the magnitude decreased by only 6% over more than a year.

In order to understand the enhanced properties of the acetone-exfoliated MoS_2, further characterisation was performed to identify any structural modification to the exfoliated nanosheets. Atomic force micrographs show that the nanosheets have a different morphology (Figure 4.2A when comparing with MoS_2 exfoliated in isopropanol (IPA) using the same exfoliation parameters (Figure 4.2D). IPA is chosen as another low boiling point solvent and a molecular structural analogue for acetone. Line sections indicated on the micrographs of the height and adhesion channels (Figures 4.2A, 4.2B, 4.2C, 4.2D) are plotted separately in Figures 4.2E and 4.2F. The values for nanomechanical adhesion were offset to the average value for the substrate for both samples. There is a "halo", a region of higher adhesion surrounding the nanosheets exfoliated in acetone representing a higher interaction between the tip and nanosheets than tip and substrate. The feature is not observed in the height channel, as seen in Figure 4.2A. Also, the magnitude of adhesion forces is lower for the acetone-exfoliated nanosheets, which differs from the IPA sample, where adhesion for the flakes is the same as for the substrate.

LPE inherently produces a dispersion with a broad size distribution. This is particularly true since a single centrifugation step was used for size selection. The relationship between physical thickness and layer number for LPE MoS_2 has been studied previously [6, 47, 128], with a monolayer thickness of 1.9 nm. In this case, thicknesses between approximately 2 nm and 20 nm correspond to 1-10 layer (i.e. 'few-layer') nanosheets, consistent with the average layer numbers measured using UV-vis metrics which are only

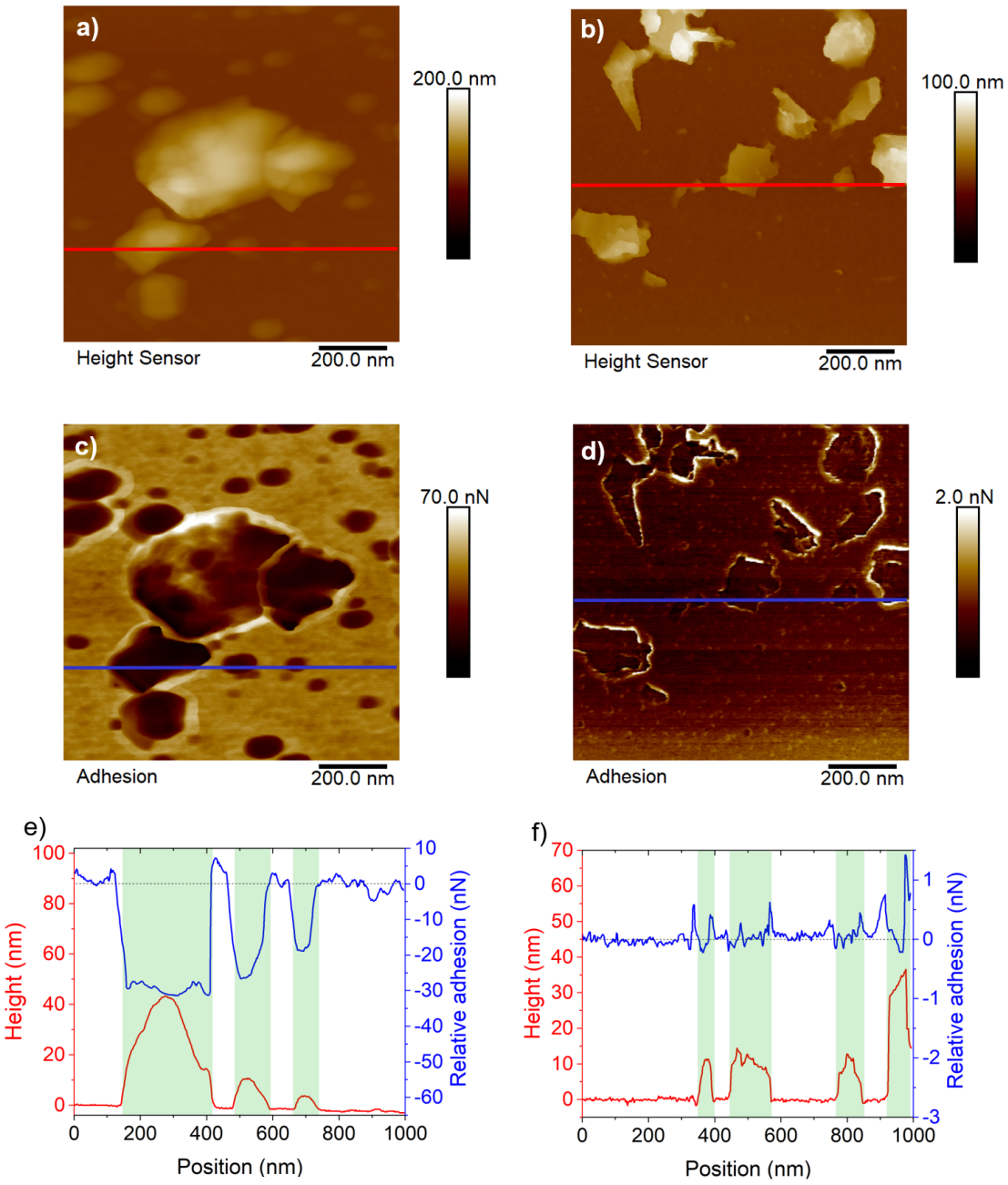

Figure 4.2: AFM data for acetone-exfoliated (**A, C, E**) and IPA-exfoliated (**B, D, F**) nanosheets. **A** and **B** Topography. **C** and **D** Nanomechanical adhesion. **E** and **F** Graph comparing the topological and adhesion information for the line section marked. The nanosheets are highlighted.

calibrated to measure the average layer number. Additionally, the significant effect of the measurement parameters in the resulting thickness has been studied previously [182]. Equally, significantly thicker particles ($\gg 10\,\text{nm}$) are likely to be aggregates introduced

during deposition of the dispersion for characterisation, due to the stochastic nature of the process.

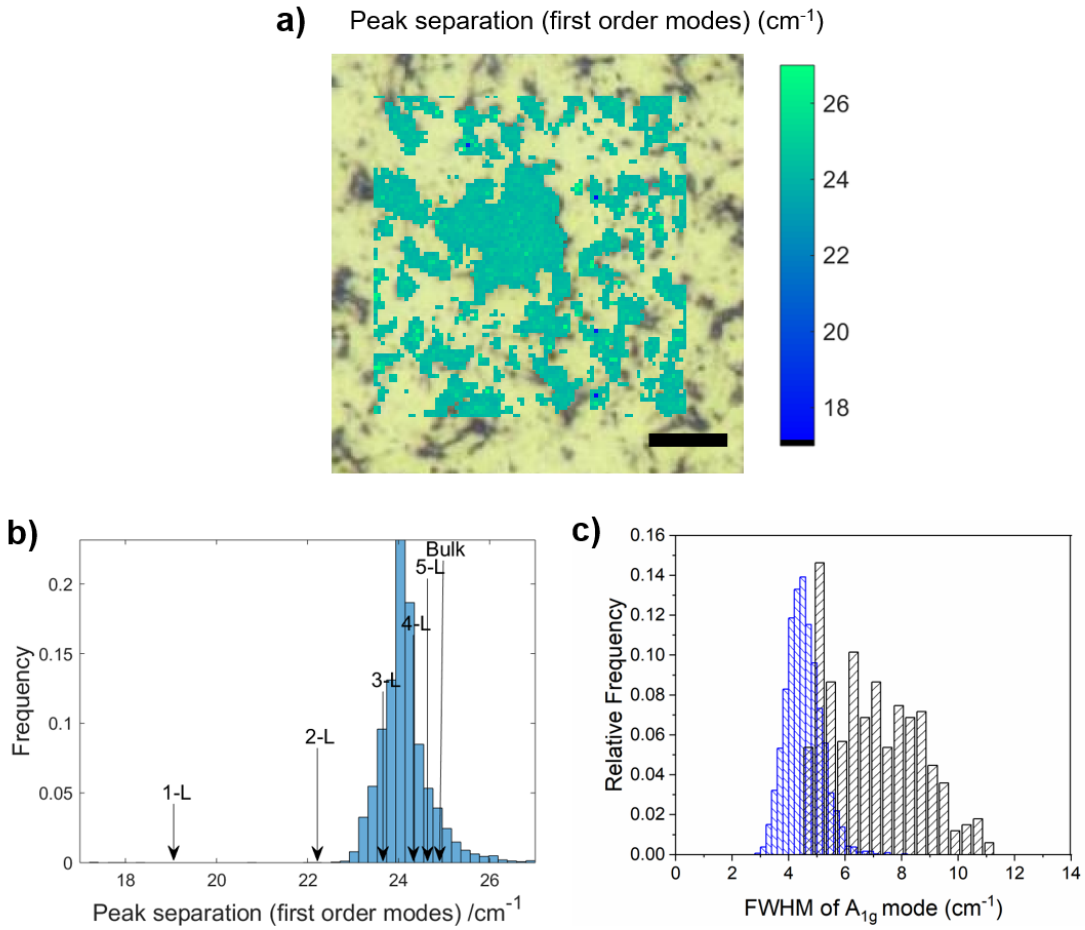

Figure 4.3: Raman spectra mapping. **A:** Peak separation map for resonant excitation. **B:** Histogram of the peak separation and the corresponding average layer number. **C:** Histogram of FWHM of out-of plane (A_{1g}) mode for MoS_2 exfoliated in acetone (black) and IPA (blue).

Resonant Raman mapping was performed to statistically evaluate the degree of exfoliation over a large area. The separation of the two main MoS_2 peaks, the in-plane (E^1_{2g}) and the out-of-plane (A_{1g}) modes [183], for each pixel is plotted as a colour map overlaying the white light micrograph of the same area (Figure 4.3A). The associated histogram of the peak separation, which is correlated with layer number distribution [9], is shown in Figure 4.3B. The histogram features a narrow asymmetric distribution with average peak separation of $24.2\,\mathrm{cm}^{-1}$ (standard deviation of $0.63\,\mathrm{cm}^{-1}$). Indicative values of the mode separation based on measurements of mechanically exfoliated MoS_2 from the literature

suggest that the mean layer number in the sample is $\langle N \rangle \approx 4$, which is consistent with UV-vis measurements made previously. This supports the demonstration of high-quality exfoliation in a low-boiling point solvent.

Raman mapping of acetone-exfoliated nanosheets shows a broader full width at half maximum for the out-of-plane mode when compared to the IPA-exfoliated material (Figure 4.3C). Literature about mechanically cleaved MoS_2 [10] suggests the broadening may be associated with a higher defect density.

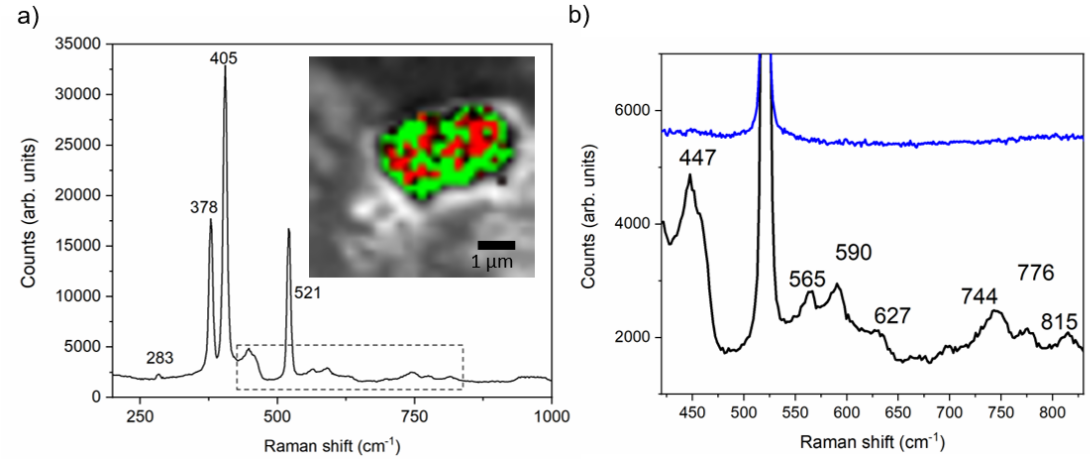

Figure 4.4: **A:** Typical Raman spectrum from the map is shown. Inset corresponds to mapping image. Colour scheme: green represents the MoS_2 peak; grey, silicon and red, molybdenum trioxide. **B:** Zoomed region from panel A showing additional peaks observed for acetone-exfoliated (black) in contrast with IPA-exfoliated nanosheets (blue).

A representative spectrum from a non-resonant Raman mapping (Figure 4.4A shows the expected MoS_2 modes: E^1_{2g} at 378 cm^{-1} and A_{1g} at 405 cm^{-1}. The peak at 521 cm^{-1} is the silicon wafer substrate and the peak at 447 cm^{-1} is silicon oxide. The remaining modes are not present in dispersions of MoS_2 in IPA produced with the same exfoliation parameters (Figure 4.4B). Peaks at 590 and 776 cm^{-1} are vibrational modes of acetone. The samples have been treated above the boiling point of acetone before performing the characterisation to remove any residual solvent. The presence of those modes even after the heat treatment suggest a strong interaction between the nanosheets and solvent. The peaks at 283 and 815 cm^{-1} correspond to known modes of MoO_3, while the peak at 627 cm^{-1} is associated with hydrates of MoO_3 [8, 184]. The peaks at 565 and 744 cm^{-1} are associated with MoO_2 [185]. Mapping of the modes associated with the oxides and

disulfide are shown in the inset of Figure 4.4A (in red and green, respectively). For the agglomerate mapped, the presence of the oxide peak is relatively uniform throughout the disulfide-containing areas, but the two are fundamentally co-localised. This suggests that particles of the oxides do not form in isolation from the disulfide nanosheets.

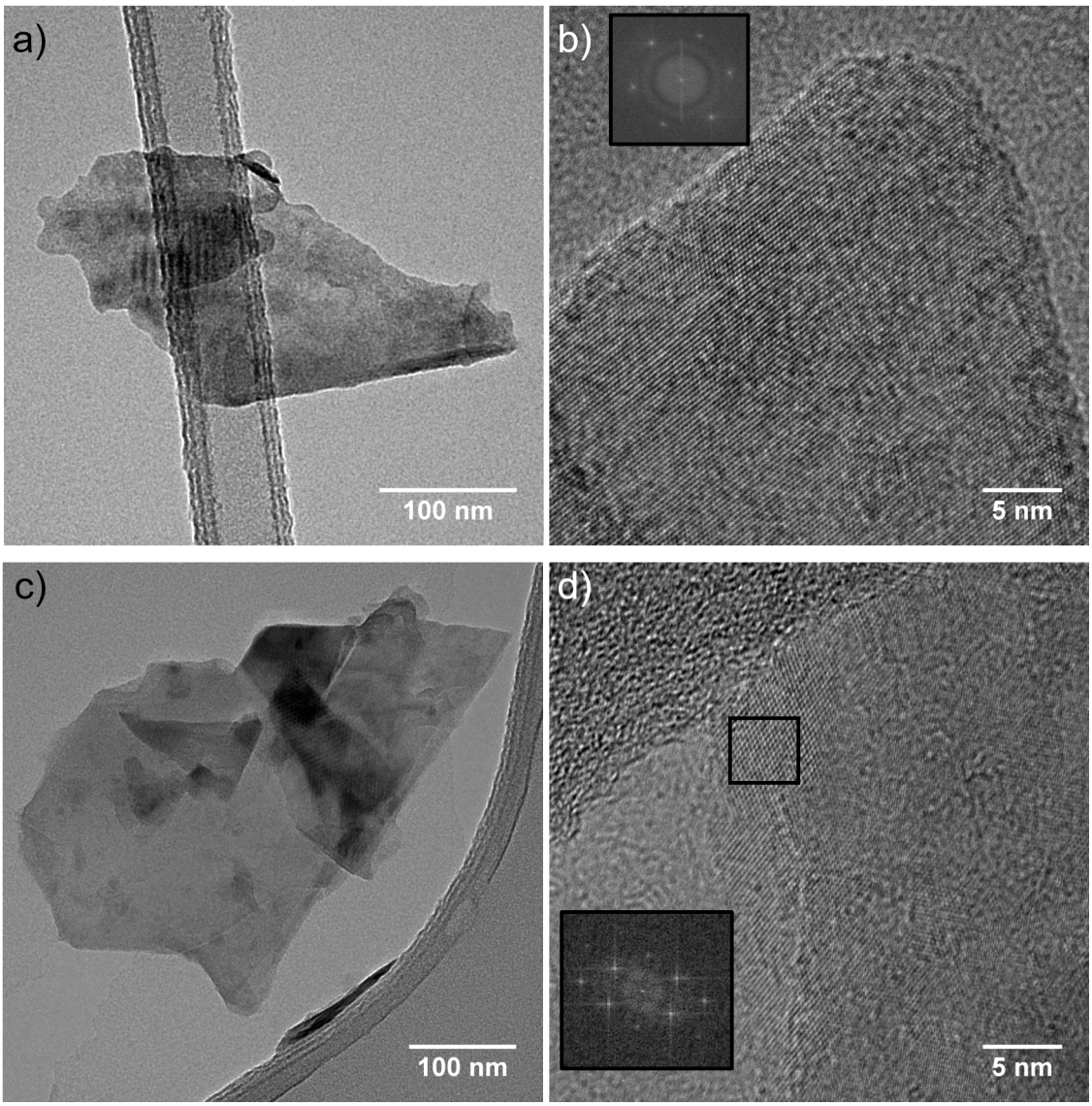

Figure 4.5: **A:** Representative TEM micrograph of MoS_2 exfoliated in isopropanol. **B:** Zoomed in TEM micrograph of the same dispersion with an inset showing the FFT as a regular hexagonal structure. **C:** Representative TEM micrograph of MoS_2 flake casted from the dispersion in acetone. **D:** Edge of an acetone-exfoliated MoS_2 flake. Inset shows a different pattern in the highlighted area corresponding to few-layered molydenum trioxide.

Following this indication of the presence of other molybdenum compounds in the samples, transmission electron microscopy was performed to evaluate the morphology of these additional components. Figure 4.5 shows transmission electron micrographs

comparing MoS_2 nanosheets exfoliated in IPA (A and B) and acetone (C and D) using the same exfoliation process. Experiments were conducted by Dr Aleksey Shmeliov at Trinity College Dublin. Analysing various regions of multiple nanosheets with fast Fourier transform (FFT) it is possible to identify different crystallographic structures. The usual hexagonal structure expected for this nanomaterial is observed for the flakes exfoliated in both solvents, as seen in the inset of figure 4.5B. However, the edges of the acetone-exfoliated nanosheets have an orthorhombic pattern associated with few-layer molybdenum trioxide [186, 187] (Figure 4.5D).

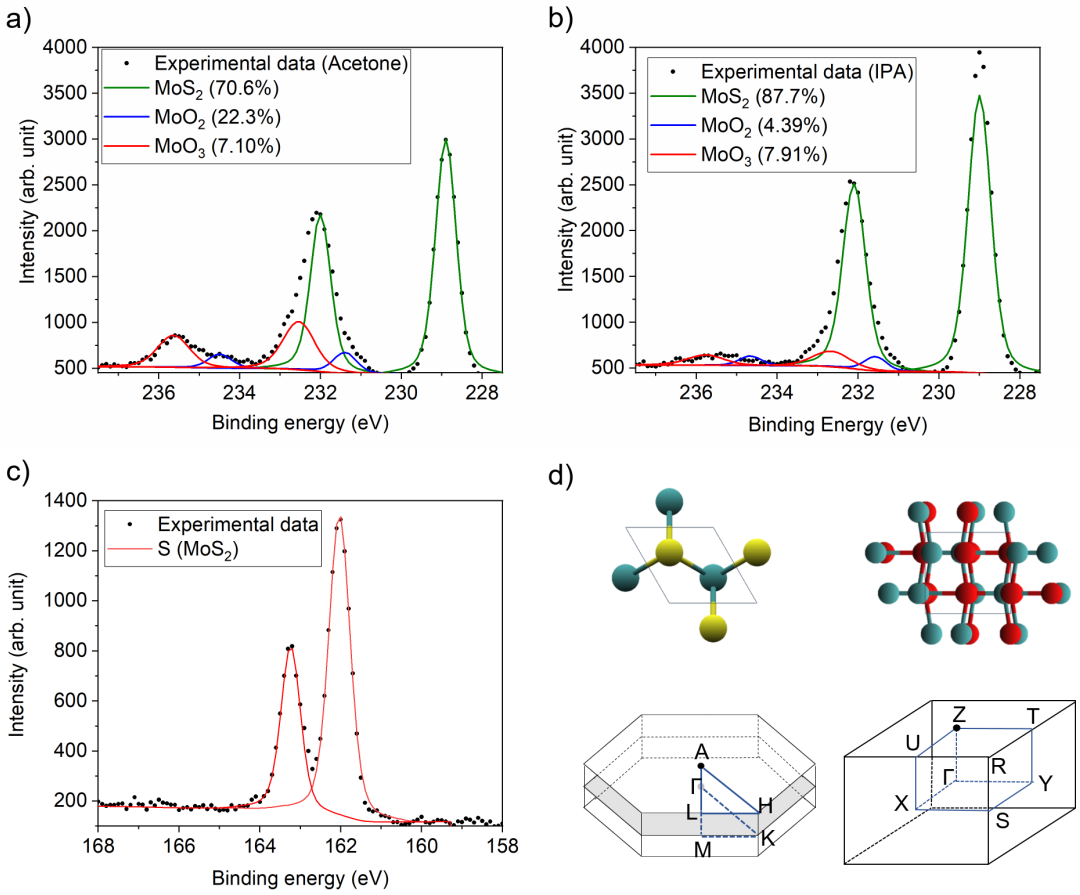

Figure 4.6: **A:** XPS spectrum in the range of sulfur binding energy for acetone-exfoliated nanosheets. **B:** XPS measurement of acetone-exfoliated nanosheets in the range of binding energy for molybdenum show the expected MoS_2 structure with additional molybdenum oxide peaks. **C:** XPS data for IPA-exfoliated nanosheets in the same range. **D:** Ball-and-stick model of MoS_2 and MoO_3, molybdenum atoms are represented in teal, sulfur, yellow, and oxygen, red. At the bottom, schematic representations of the Brillouin zones corresponding to the crystal systems of 2H-MoS_2 and α-MoO_3

In order to confirm that the structural modification at the nanosheet edges corresponds to the chemical modification observed in the Raman spectroscopy, X-ray photoelectron spectroscopy (XPS) was employed by Dr Santanu Ray at the University of Brighton to characterise its composition. The binding energy measurement in the range associated with molybdenum compounds for the MoS_2 nanosheets exfoliated in acetone and IPA are shown in Figure 4.6 (in panels A and B, respectively). Figure 4.6C shows the sulfur range for the nanosheets exfoliated in acetone and the expected presence of MoS_2. The acetone-exfoliated sample was found to have 11.2 at % molybdenum, 18.2 at % sulfur and 16.0 at % oxygen. Even though the equipment used does not allow for spatial resolution, this excess of molybdenum atoms when compared to sulfur atoms (the ratio is greater than 1 : 2) and the significant oxygen presence confirms the formation of other molybdenum-based compounds including MoO_2 and MoO_3. The atomic percentages when analysing just the compounds containing molybdenum atoms are 70.6 % for MoS_2, 22.3 % for MoO_3 and 7.1 % for MoO_2. For IPA-exfoliated nanosheets, the atomic percentages for molybdenum atoms are assigned to each compound as follows: 87.7 % for MoS_2, 7.91 % for MoO_3 and 4.39 % for MoO_2. Even though some oxidation was observed for this sample, oxide content is significantly higher for acetone-exfoliated nanosheets. Figure 4.6D shows the Brillouin zones representation associated with the different compounds; hexagonal for MoS_2 and orthorhombic structures for MoO_3.

In order to get more detailed chemical and structural information of the effects of the dispersion of MoS_2 in different solvents at the local scale, aberration-corrected scanning transmission electron microscopy (STEM) was performed at the University of Zaragoza by Dr Raul Arenal. High-angle annular dark field (HAADF) STEM combined with spatially-resolved electron energy loss spectroscopy (SR-EELS) is a powerful technique for getting this information [188, 189]. Figures 4.7A and 4.7C show two HAADF-STEM images of two of these MoS_2 nanosheets exfoliated in IPA and acetone, respectively. Different EELS spectrum-lines (SPLI, 1D)/-images (SPIM, 2D) were recorded on these flakes. Figures 4.7A and 4.7C display the areas where an EELS SPLI and a SPIM have been collected

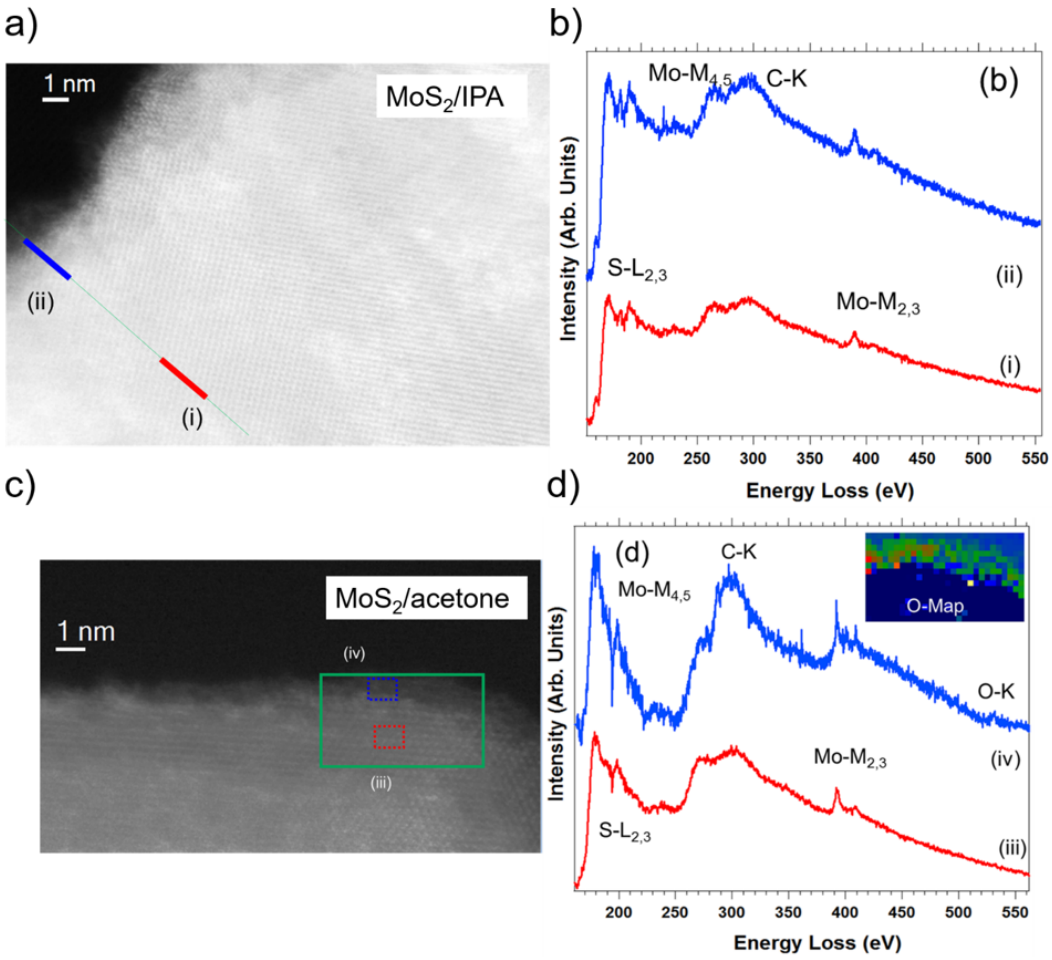

Figure 4.7: Micrographs of two MoS_2 nanosheets exfoliated in **A** IPA and **C** acetone. In the IPA-exfoliated MoS_2 nanosheet an EELS spectrum-line was collected following the green marked line. **B:** Two EELS spectra corresponding to the sum of 12 spectra collected in each of the two highlighted areas (red (i) and blue (ii)). Sulfur and molybdenum (associated to the MoS_2) as well as some carbon are detected in these spectra. **D:** Two EEL spectra corresponding to the addition of 21 spectra recorded in each of the 2 regions highlighted in red (iii) and blue (iv) in the green marked area of C. The inset of this figure shows the O map obtained from this EELS spectrum-image. Oxygen, which is likely associated to molybdenum oxide, is present at the edge of the flake, as clearly observed in this elemental map.

(green highlighted areas). Two different EEL spectra, corresponding to the addition of 12 spectra in the regions marked in Figure 4.7A, are displayed in Figure 4.7B.

The analysis of these EELS data indicates that the flakes from the IPA dispersion are composed of MoS_2 and that their composition is homogeneous and uniform. The C-K feature visible in these spectra probably arises from a small carbon contamination. This situation is different in the case of the MoS_2 in the acetone dispersion sample, as seen in

Figure 4.7C and 4.7D. The edges present an amorphous layer of less than 1 nm. This layer contains some carbon and oxygen (see the O-map, inset of Figure 4.7D). The presence of oxygen at the edges indicates the clear oxidation of these MoS_2 nanosheets in this region agreeing with the other characterisation results performed on these samples.

Thermodynamically, the surface of MoS_2 tends to be oxidised when in contact with oxygen by adsorption or substitution. As seen in the literature, [190, 191, 192] the chemical reaction for oxidation of MoS_2 in presence of oxygen gas is:

$$2\,MoS_2 + 7\,O_2 \longrightarrow 2\,MoO_3 + 4\,SO_2 \tag{4.1}$$

$$MoS_2 + 6\,MoO_3 \longrightarrow 7\,MoO_2 + 2\,SO_2 \tag{4.2}$$

$$2\,MoO_2 + O_2 \longrightarrow 2\,MoO_3 \tag{4.3}$$

Density functional theory calculations show that the kinetic energy barrier for oxidation is lowered when sulfur vacancies, which have a high prevalence at edge sites, are produced during exfoliation [193]. These equations suggest the formation of sulfur dioxide, which would outgas and prevent observation by the characterisation techniques employed here. However, a pungent, sulfur-like odour, different from acetone, was noticed in the as-produced samples. Sulfur dioxide gas is very soluble (reaching several hundred v/v) in several organic solvents, including acetone [194]. This adds some weight, albeit qualitative, to the series of reactions shown above. It suggests that the observed chemical modification to the nanosheets occurs through interaction with atmospheric oxygen rather than with the solvent as acetone has greater propensity to contain or produce dissolved oxygen or oxygen radicals during sonication [195].

In order to study the timescales involved for the spontaneous functionalisation of MoS_2 during exfoliation in acetone, an experiment was performed where the sonication time during exfoliation was varied. Lateral size and concentration values were obtained from recognised metrics [6] using UV-vis spectra. Average nanosheets length decays exponentially while concentration increases until a saturation point is reached (Figure

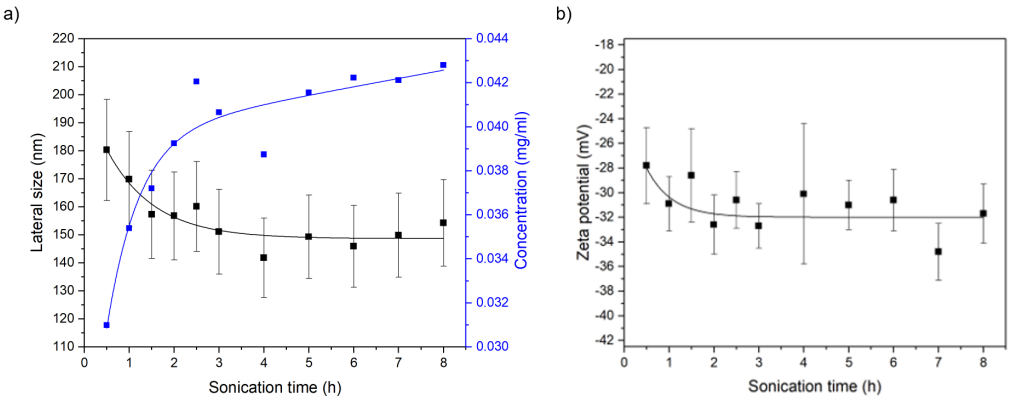

Figure 4.8: **A:** Length, concentration from metrics [6] and **B:** zeta potential plotted for different sonication times.

4.8A). Zeta potential measurements (Figure 4.8B) show that the exfoliated nanosheets are stable in dispersion even after short sonication times.

It is noted that the high stability and concentration originates from a self-limiting process since each measured property of the dispersions has the tendency to plateau after approximately 3 hours of sonication. The electronegativity of oxygen atoms is higher than sulfur, which will result in a stronger Mo-X bond polarisation with the delta-negative charge residing on the chalcogen atoms, producing a negative charge on the particle surface. As the proportion of MoO_n components in the nanosheets increases, one would expect an increase in the magnitude of the negative charge on the particles, as we observe. Also MoO_3 is shown to be readily exfoliable in solvents, which are too polar and/or low surface energy for exfoliation of MoS_2 (i.e. IPA, compared to NMP) [186]. Importantly, adding MoO_3 edge functionality to MoS_2 nanosheets presents the possibility of tuning the solubility across this range of solvents, perhaps improving dispersibility in solvents such as acetone, which are otherwise poor for MoS_2.

Continuing quantifying how microscopic modification of the nanosheets by spontaneous edge functionalisation influence macroscopic properties such as the interaction with the solvent, Hansen and Hildebrand solubility parameters were measured for both supernatant and sediment of the final centrifugation step after the sonication. Acetone-functionalised nanosheets were redispersed in new solvents to test their chemistry. Figures 4.9A and B show the Hildebrand plot for dispersions of MoS_2 nanosheets. Hansen para-

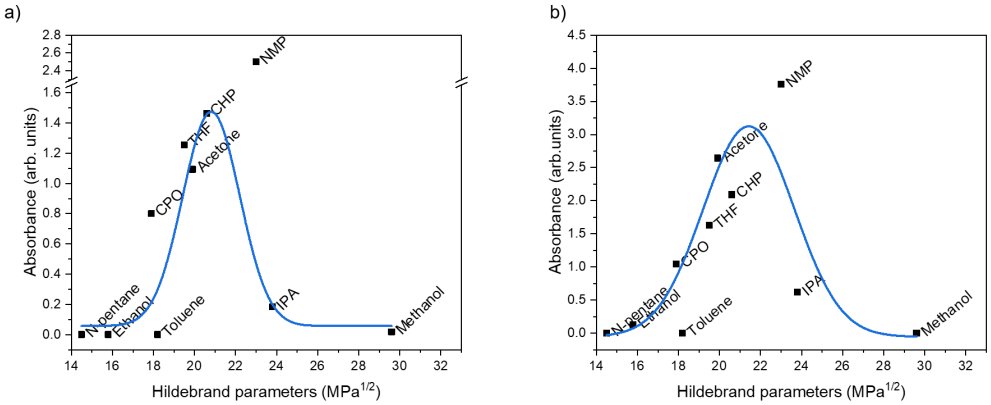

Figure 4.9: Hildebrand solubility parameters for **A** exfoliated nanosheets and **B** bulk MoS_2.

meters for both exfoliated and unexfoliated materials are shown in Figure 4.10. Comparing the results with accepted values, as seen in Table 4.2, show a significant change in the polar component between these two fractions. Hansen solubility parameters for MoO_3 were estimated by analysing data in literature [186].

NMP has the highest concentration which could be explained by its high susceptibility to ambient and sonochemical degradation [48, 51]. The solvent degradation complicates the production of an identical reference sample to the solvent in dispersion for extinction spectroscopy, and may also interfere with the exfoliation and stabilisation processes [50]. Although it is known that good solvents for nanomaterials cannot solely be identified based on Hildebrand parameters [44], it is therefore interesting to note that this exfoliation in acetone produces materials whose solubility is well described by this model, which is inferred by comparing the width of the Gaussian fitting with literature values [44, 43].

The observed modification in Hansen and Hildebrand solubility parameters reported is a direct result of the edge functionalisation of MoS_2 with MoO_3. The Hildebrand parameter for the nanosheets is $20.8 \pm 0.6\,\mathrm{MPa}^{1/2}$. The accepted value of the solubility parameter for MoO_3 is $20.7\,\mathrm{MPa}^{1/2}$ [186] and MoS_2 is $21.1\,\mathrm{MPa}^{1/2}$ [44]. The oxidation processes shift the values of the parameters for the MoS_2 nanosheets closer to the value for acetone ($19.9\,\mathrm{MPa}^{1/2}$). This functionalisation is responsible for the improved dispersability in acetone and appears to make MoS_2 more selective to well Hildebrand matched solvents, as is the case for MoO_3 [186].

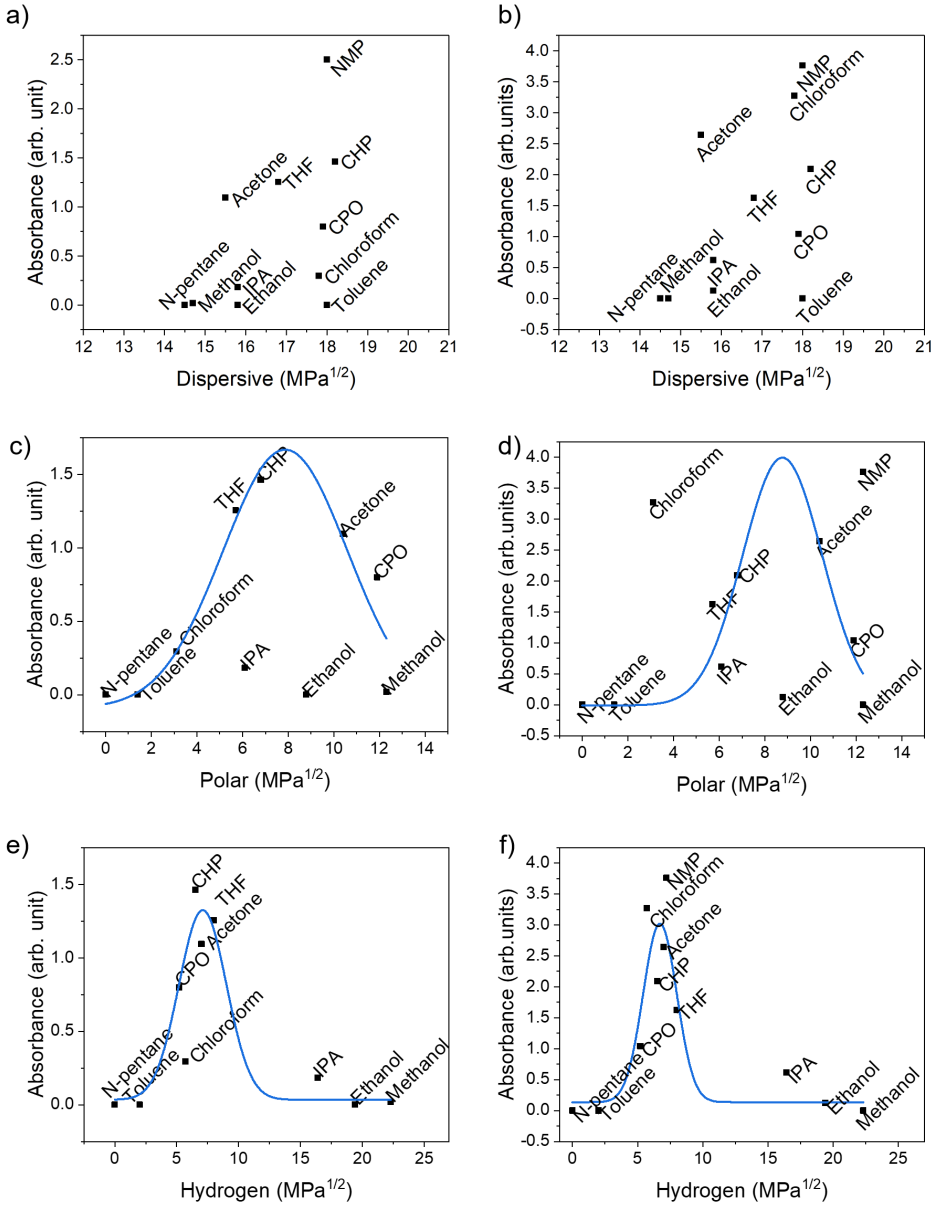

Figure 4.10: Hansen solubility parameters for **A,C,E** nanosheets and **B, D, F** bulk MoS_2.

Material	Dispersive component ($MPa^{1/2}$)	Polar component ($MPa^{1/2}$)	Hydrogen bond component ($MPa^{1/2}$)	Hildebrand parameter ($MPa^{1/2}$)
MoS_2 [44]	18.0	8.5	7.0	21.1
MoO_3 [186]	18.0	7.1	6.4	20.7
Exfoliated MoS_2	17.91	7.87 ± 0.36	7.10 ± 0.38	20.81 ± 0.63
Bulk MoS_2	18.37	8.77 ± 0.23	6.70 ± 0.29	21.43 ± 0.55
Acetone [122]	15.5	10.4	7.0	19.9

Table 4.2: Comparison between measured Hansen and Hildebrand parameters for exfoliated MoS_2 and bulk with literature values for MoS_2, MoO_3 and the solvent.

Hansen parameters for 2-butanone [122], a linear ketone containing one extra carbon than acetone, are 16.0, 9.0 and 5.1 $MPa^{1/2}$, for dispersive, polar and hydrogen bonding components, respectively. Highly concentrated dispersions of TMDs in 2-butanone using bath sonication was obtained by Lobo *et al.* [59]. In this study, a similar degree of exfoliation was obtained, as indicated by peak separation of the in-plane and out-of-plane Raman modes for MoS_2 (24.2 cm^{-1} for acetone and 24.9 cm^{-1} for 2-butanone). However the sedimentation life-time is significantly lower for 2-butanone, despite it having a better Hansen matching (smaller interaction radius) and higher viscosity [196].

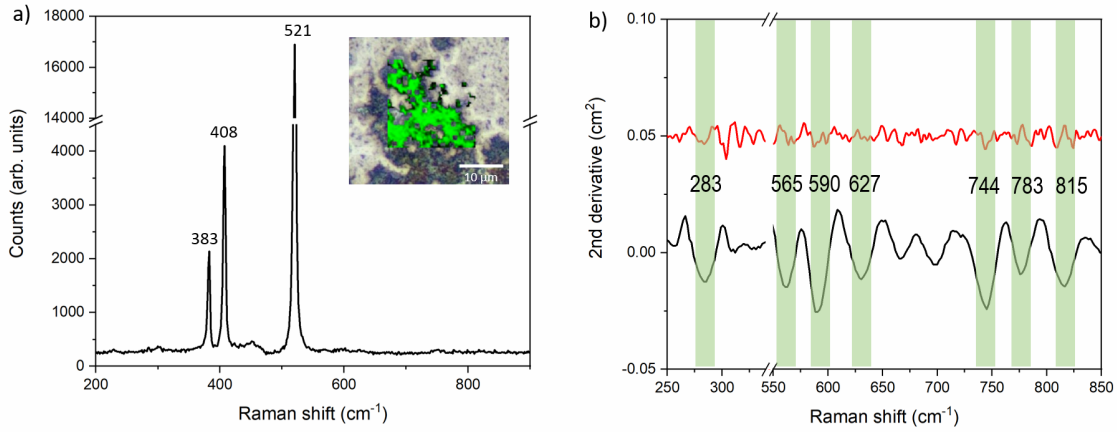

Figure 4.11: **A:** Representative Raman spectrum from a dispersion of MoS_2 exfoliated in 2-butanone map (inset). **B:** Second derivative plot of Raman spectra for MoS_2 exfoliated in acetone (black) and 2-butanone (red) in the range of observed oxide modes. Highlighted areas are correlated to peak assignment done in Figure 4.4.

Chemical characterisation (XPS) and microscopy (HRTEM and AFM micrographs) in that work [59] do not indicate the presence of molybdenum oxides. It is observed that the zeta potential for nanosheets exfoliated in acetone is significantly higher than for those reported in 2-butanone. It is inferred that this is due to edge functionalisation present in the acetone-exfoliated nanosheets, and that this is in turn responsible for the extended sedimentation time. Exfoliation in 2-butanone using the same parameters for acetone was performed and the nanosheets characterised using Raman spectroscopy (4.11A).

Oxides peaks were not observed for the sample, as clearly demonstrated by the second derivative of the Raman spectra in Figure 4.11B. The second derivative clearly shows the position of local minima and maxima points, which can be correlated to Raman modes

positions. The oxide modes identified in Figure 4.4 are highlighted. The high quality and stability observed in acetone-exfoliated MoS_2 nanosheets due to spontaneous edge functionalisation seems to be unique to acetone because of a combination of factors such as dissolved oxygen content, low viscosity and high vapour pressure, independently of surface energy and Hansen parameters matching.

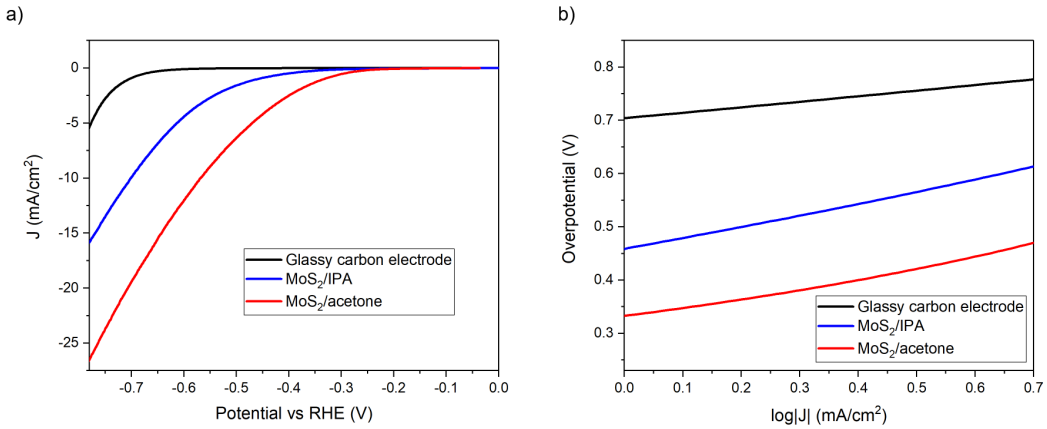

Figure 4.12: **A:** Polarization curves for MoS_2 exfoliated in acetone (red) and IPA (blue). Reference substrate glassy carbon electrode is shown in black. **B:** Corresponding Tafel plots.

Exfoliated MoS_2 has been proposed as an efficient catalyst for the hydrogen evolution reaction (HER). Hydrogen is an environmentally-friendly alternative energy source to fossil fuel, and catalysts are necessary to increase the reaction efficiency to reach mass production levels. Platinum is known to be the best catalyst [197], however its high cost and unavailability in large quantities limit its use [198], prompting searches for alternative materials. Recent work has indicated that the edge sites and active site density on the edges of nanosheets are responsible for this catalytic activity [27, 199]. In order to investigate the effect of edge oxidation on the performance of MoS_2 nanosheets as HER catalysts, MoS_2 exfoliated in acetone was compared against the same mass of MoS_2 prepared in IPA. The measurement was made by supporting the MoS_2 catalyst on a conductive and inert substrate (glassy carbon). Linear sweep voltammetry was used to measure the current against potential. For the HER, it is useful to offset the potential scale to the reversible hydrogen electrode (RHE), while the current is normalised to the electrode area [200],

as seen in Figure 4.12A. A superficial analysis of Figure 4.12 shows that the acetone-exfoliated nanosheets have a higher current density across the entire potential range which indicates its superiority.

	Tafel slope (mV/decade)	Onset potential (V *vs.* RHE)	J @ −0.4 V ($mA\,cm^{-2}$)	Size (from UV-vis metrics) (nm)
MoS_2 /IPA	193	-0.38	0.50	172
MoS_2 /acetone	150	-0.27	2.51	212

Table 4.3: Hydrogen evolution characteristics of MoS_2 exfoliated in IPA and acetone

Deeper analysis shows an onset potential, the potential value for which catalyst current is first observed, for hydrogen evolution at $-0.27\,V$ *vs.* RHE and a current density of $2.51\,mA\,cm^{-2}$ at $-0.4\,V$ for the sample prepared in acetone, shown in Table 4.3. The IPA sample shows a higher onset potential, the potential required to reach $1\,mA\,cm^{-2}$, and a lower current density both of which result in an inferior hydrogen evolution catalyst. Figure 4.12B shows the Tafel curves of the J-V data displayed in Figure 4.12A. From the linear region of this curve we can extract the Tafel slope which is representative of the effectiveness of a material as a HER catalyst (lower is better) and the mechanism by which the H_3O^+ ions are reduced. It measures the potential increase necessary to improve the current density by one order of magnitude [201]. The Tafel slope recorded is in the range attributed to MoS_2 in literature [197, 198]. The same parameter has been reported as low as $40\,mV/decade$ for chemically-exfoliated 1T-MoS_2 nanosheets [202]. In the same work, the 2H-polytype showed an increase in Tafel slope to about $80\,mV/decade$, which could be improved by adding single-wall carbon nanotubes to dope the MoS_2 nanosheets, increasing the conductivity of the network. Chia *et al.* compiled a comprehensive table of electrochemical characterisation of different TMDs [203]. The values obtained for Tafel slope in this present work are comparable to those for commercially available nanosheets [204].

Of primary importance is that across all metrics, shown in Table 4.3, MoS_2 exfoliated in acetone exceeds the performance of that prepared in IPA in terms of hydrogen evolution efficiency. It is also interesting that the MoS_2 nanosheets exfoliated in acetone are

significantly bigger than those prepared in IPA. The turnover frequency of MoS_2 hydrogen evolution has been shown to be inversely proportional to the length and directly to the active site density [201]. This suggests that, while MoS_2 prepared in acetone is larger, it has much more active sites that participate in hydrogen evolution. This could be due to oxide groups having preferential energetics to hydrogen ion adsorption, electron transfer or lower steric hindrance. Also, the MoO_3 hydrophilic edges allow for better contact with electrolyte [205].

4.3 Conclusions

The high concentration and stability of MoS_2 nanosheets dispersed in acetone is not fully explained by the Hansen solubility parameter model. Edge functionalisation occurs spontaneously during ultrasonic exfoliation and produces molybdenum oxide, which fundamentally changes the main interaction of the nanosheets with the solvent. It is also observed that the edge functionalisation significantly modifies macroscopic properties resulting in an improved performance of acetone-exfoliated MoS_2 as a hydrogen evolution reaction catalyst, in comparison with material prepared in the same way using a structural analogue solvent (IPA). Evidence of functionalisation are observed with modification of solubility parameters and HER activity, which are known to be edge sensitive. Microscopic characterisation confirms the presence of oxygen-containing regions at the edges of the nanosheets. The exfoliation in acetone could be generally applied as a pretreatment to modify the solubility of layered materials by edge functionalisation. In particular it is of interest to investigate whether the same chemistry is observed, under exfoliation conditions, for the other transition metal dichalcogenides, possibly bringing out useful properties.

Chapter 5

Metricised Raman mapping analysis of nanosheet size distributions

The growing research interest and uptake of layered nanomaterials for real-world applications require efficient, reliable, high-quality characterisation methods. Liquid phase exfoliation can achieve high production rates and quality despite the small nanosheet size. Liquid-exfoliated graphene has Raman spectroscopic metrics for mean lateral size and layer number. Here it is presented a methodology to create Raman maps in order to reconstruct distributions of the nanosheet properties, by applying the metrics for each pixel, not just averaging the obtained spectra. The method is successfully demonstrated for graphene, so an extention of the approach to MoS_2, the archetypal TMD, was attempted. The only available metric from the literature which describes layer number relies on peak separation between the two main modes: E^1_{2g} and A_{1g}. However, as demonstrated here, both modes shift with increasing defect density, strain, and doping. This metric is useful, however these effects are often neglected, misleading the interpretation of measurements obtained by Raman spectroscopy, especially for LPE MoS_2. The use of metricised Raman mapping analysis, here demonstrated for graphene, facilitates the standardisation of characterisation, allowing the correlation of size- and thickness-sensitive applications' performance with materials properties. The extension to MoS_2 proved to be more challenging as applying

the literature layer number metric can lead to incorrect results and a length metric is still missing in the literature.

5.1 Introduction

As layered nanomaterials become more widespread there has been growing concern over the quality of the materials supply. In particular, there has been increasing demand for standardisation of methods and metrics to ensure reproducibility of materials and results, as well as appropriate definitions of materials [206, 207, 125, 208, 61]. The International Organization for Standardization published a list of vocabulary terms to accelerate the uptake of graphene materials in industry [60]. To date, many efforts to standardise approaches and characterisation have focused on graphene. It is the most widely-recognised archetypal layered material, and has the greatest prospects for short-term acceptance in applications. However, it is clear that other layered nanomaterials, such as hexagonal boron nitride and transition metal dichalcogenides, will eventually suffer the same concerns regarding material quality and reproducibility.

Liquid phase exfoliation of layered materials has been shown to achieve high production rates [42, 128] and high material quality [116, 45, 46], albeit for small lateral particle sizes [43]. Additionally, LPE processes necessarily produce a distribution of particle sizes and thicknesses. Although centrifugation-based size selection can separate particles approximately by layer number [144], robust methods are necessary to characterise the relevant nanosheet properties such as layer number, length and distribution parameters. In particular, the average layer number (and layer number range) are important since accessible surface area is a dominant performance indicator in many applications, such as reinforcement in composites, catalytic activity, and electrochemical energy storage devices, regardless of the specific material properties.

5.2 Metrics for graphene layer number and length

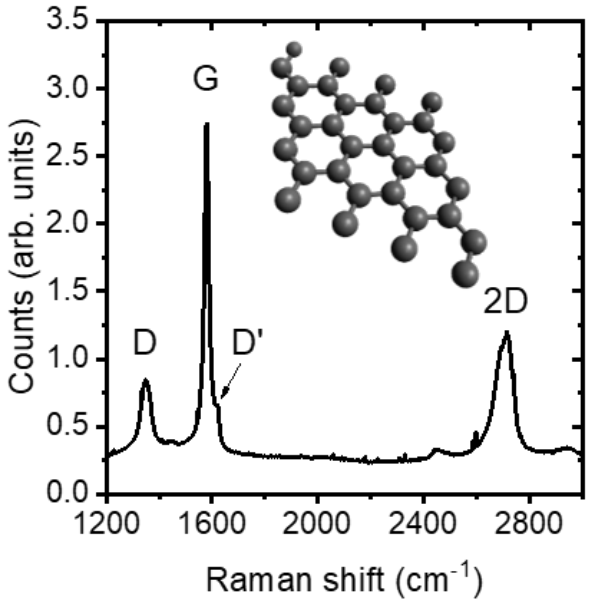

Figure 5.1: Raman spectrum averaged over a large area of an LPE graphene film prepared by drop casting the dispersion on a hot substrate. Graphene Raman modes are labelled.

Graphene has well-established Raman metrics for mean layer number and lateral size for LPE nanosheets. Figure 5.1 shows a typical Raman spectrum of LPE graphene. The main modes of interest are the G (C-C bonding), D (a defect-activated mode indicating presence of grain boundaries, edges, or basal plane defects), and 2D peaks (an overtone of the D peak containing information on inter-layer coupling) [209, 210, 63]. In order to demonstrate how Raman can be used to achieve a more thorough analysis of particle size distributions the Raman metrics of Backes *et al.* [64] were adopted. They relate the average layer number of a graphene nanosheet sample $\langle N \rangle$ to the intensity ratio of the 2D and G peaks:

$$\langle N \rangle = 1.04 \frac{I_{2D}}{I_G}^{-2.32}, \tag{5.1}$$

as well as the average lateral size $\langle L \rangle$ to the ratio of D- and G-peaks:

$$\langle L \rangle = \frac{0.094}{(I_D/I_G)_{\text{graphene}} - (I_D/I_G)_{\text{graphite}}} \tag{5.2}$$

where $(I_D/I_G)_{\text{graphite}}$ is the D/G intensity ratio for the unexfoliated graphite. These metrics were developed by averaging the spectra from a map of filtered dispersions, meaning the nanosheets are distributed randomly over hundreds of nanometers depth and that at each measurement position many nanosheets are present within the volume of the laser spot. Such approach works well for dispersions with narrow distributions of layer number. However, for a broad distribution, the most common result for LPE dispersions, the measurement is skewed towards thicker sheets, as optical transmittance is layer number dependent [211].

5.3 Resolution-limited Raman mapping

Raman mapping is known to be non-destructive technique with high chemical specificity. As opposed to single-point spectra, which provide discrete information at distinct positions within the sample, mapping provides the same information but coupled with spatial resolution [212]. The measurement process described here is to map the Raman spectra of a sample area using high magnification (100x objective, NA 0.85) and pixel size determined by the calculated lateral resolution limit of the objective. Samples were prepared by drop casting dispersions onto silicon wafer heated above the boiling point of water to remove any residual solvent in the analysed sample, and to minimise re-aggregation of the nanosheets during drying. As much as possible, the mass per unit area of material deposited for analysis was kept constant.

In order to determine the uniformity of the samples and the effects on resulting layer number and length distributions, a 20 µm by 20 µm map was divided into four quadrants, as shown in Figure 5.2A. The distributions resulting from the each quadrant were plotted alongside with the total map area in Figure 5.2B-C for layer number and characteristic length, respectively. The histograms are barely distinguishable so the averages obtained from them were plotted with the corresponding standard deviations in Figure 5.2D. This

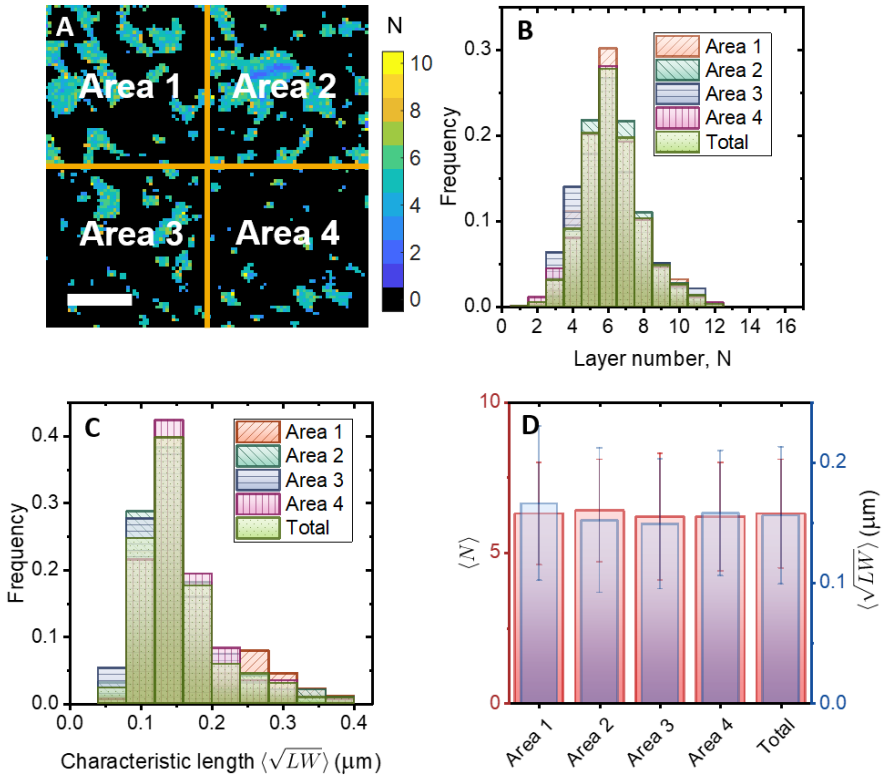

Figure 5.2: **A:** Raman map colour coded according to layer number for the 2h LCC sample. Scale bar is 5 µm. The distributions obtained from the four different areas are shown with the total area for both layer number (panel **B**) and characteristic length (**C**). **D:** Average of the distributions and respective standard deviations are shown.

plot shows great agreement between the different areas, highlighting the uniformity of the samples produced by drop casting on Si wafers. Also, it corroborates the fact that maps of 10 µm by 10 µm give enough statistical data to reconstruct the distributions.

The influence of magnification on the layer number distribution extracted from Raman maps of the same area of a graphene sample using two different objectives was studied and the results are illustrated in Figure 5.3. Figure 5.3A shows the Raman mapping colour-coded according to layer number for the 20x, NA 0.4 objective in comparison to the same plot for the 100x, NA 0.85 objective (Figure 5.3B). Figure 5.3C shows the histogram of layer number for both maps, normalised to the bin with the highest number of counts. High magnification shows a lower average (4.76) when compared to a lower magnification (5.73). Higher magnification means less nanosheets per laser spot. It is clear from the

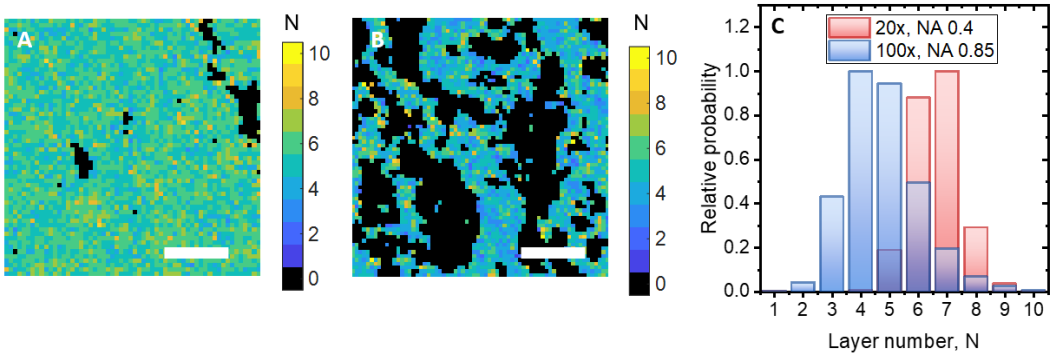

Figure 5.3: Raman map of a graphene sample done on the same area with different objectives: **A:** 20x and **B:** 100x. The scale bar is 10 µm for both plots. **C:** Plot of relative probability for the layer number distributions from the maps.

measurement shown in Figure 5.3 that the distribution is skewed towards thicker sheets when there are more nanosheets per focal spot.

The pixel size for the maps was determined following the procedure below. The size of the focus spot may be calculated using the following equation:

$$\text{Spot size} = \frac{1.22\lambda_{EX}}{NA} \tag{5.3}$$

where λ_{EX} is the excitation wavelength and NA is the numerical aperture of the objective. However, for a confocal Raman system, the lateral resolution is defined as the minimum distance between two points for them to be resolved as two different objects. The equation for lateral resolution is [213]:

$$\text{Lateral resolution} = \frac{1}{\sqrt{1+\beta^2}} \frac{0.61 n \lambda_{EX}}{NA} \tag{5.4}$$

where n is the refractive index of the medium and $\beta = \lambda_{EX}/\lambda_{DT}$, is the ratio between the excitation and detection wavelengths. The silicon mode of the substrate corresponding to the optical branch at the centre of the Brillouin zone at 520 cm^{-1} [214] was used as the reference, corresponding to the lowest resolution, around 300 nm for both lasers (660 nm and 532 nm, wavelength) used in this thesis.

The area being analysed was set to a minimum of 100 μm^2, in order to achieve high statistical power. Laser power and acquisition time varied between graphene and resonant and non-resonant MoS_2 maps to reflect the changes in number of counts for the different materials and excitation energy. Laser power and acquisition time were kept constant for every series of maps; of the order of 1 mW and hundreds of milliseconds, respectively.

Maps were baseline corrected and cosmic rays removed using the WiRE™ software before being analysed using a MATLAB script. Reading the WiRE™ files in MATLAB was possible using an open source code developed by Alex Henderson [215]. For the baseline, the software uses an "intelligent fitting", which automatically excludes regions with peaks and fits the rest of the spectrum using a polynomial approximation. Smoothing was done in two steps, using 3-point median filter first, then a 5-point Gaussian smoothing.

This approach to achieving higher statistical power from a Raman measurement is not unusual, however rather than summing pixels, the individual spectra are processed using the literature metrics. This produces a set of maps representing pixel-wise analysis of layer number and lateral size, from which histograms are plotted. Importantly, this method reconstructs particle size distributions that are close to the population distribution rather than simply measuring averages.

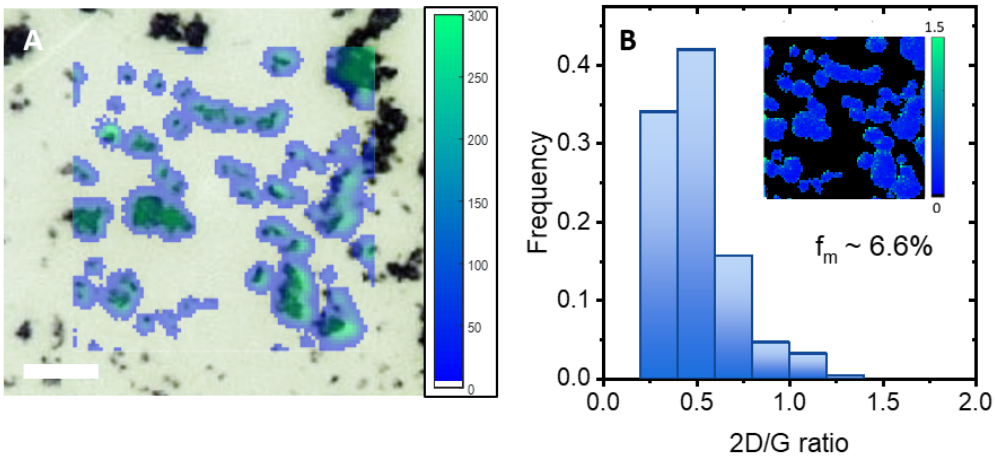

Figure 5.4: **A:** Optical micrograph and associated Raman map of G-peak intensity over a 20 µm x 20 µm area of the sample. The scale bar is 5 µm. **B:** Histogram of the 2D/G peak intensity ratio (evaluated pixel-wise from the inset 2D/G ratio map).

Figure 5.4A shows an optical micrograph of a typical LPE graphene sample with an overlaid Raman map (showing the G peak intensity). This 20 µm by 20 µm area contains 6561 spectra, which have been thresholded based on their G peak intensity using a MATLAB script to eliminate 'empty' pixels. The resulting sample contains 2742 Raman spectra. Figure 5.4B shows a histogram of 2D/G peak ratio derived from the data illustrated in Figure 5.4A. Inset is a map of the 2D/G ratio, showing that higher values (related to lower layer numbers, with a ratio > 1 indicating a monolayer particle) are concentrated at the edges of larger aggregates of particles.

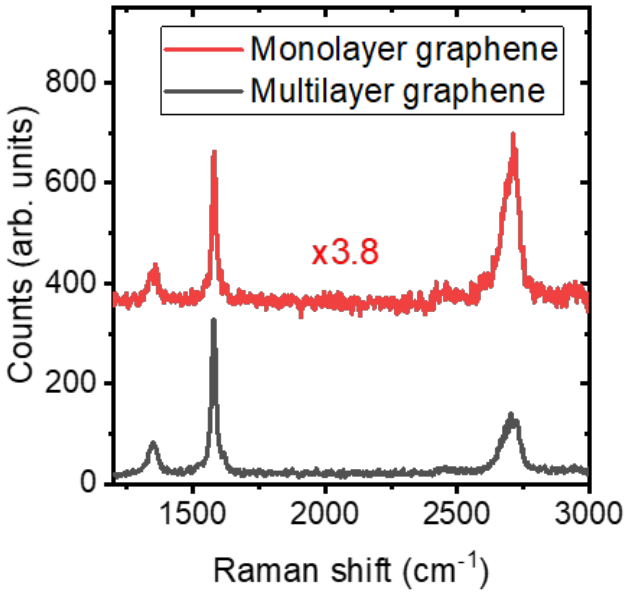

Figure 5.5: Individual pixel spectra for a larger multilayer and a monolayer nanosheet. The monolayer spectrum has been normalised relative to the G peak, and offset, for clarity.

In order to understand this phenomenon, individual pixel spectra are investigated in Figure 5.5. The two spectra shown are one with a 2D/G value greater than 1 (indicative of a monolayer) and one with a value close to the average of the distribution in Figure 5.1. When a monolayer and a multilayer particle are both present in the focal spot, the 'summed' spectrum representing both particles is heavily skewed towards the multilayer, based on the larger particle volume and optical absorption of the multilayer. This effect means that a low-magnification spectrum of a given sample, with a broad layer number distribution, will over-represent thicker multilayers and under-represent any few-layer

content; an effect that is mitigated by mapping analysis. Comparison of the spectrum in Figure 5.5 with the multilayer spectrum in Figure 5.1, and the difference observed in the distributions using different objectives (Figure 5.3) illustrate this volume-weighting effect.

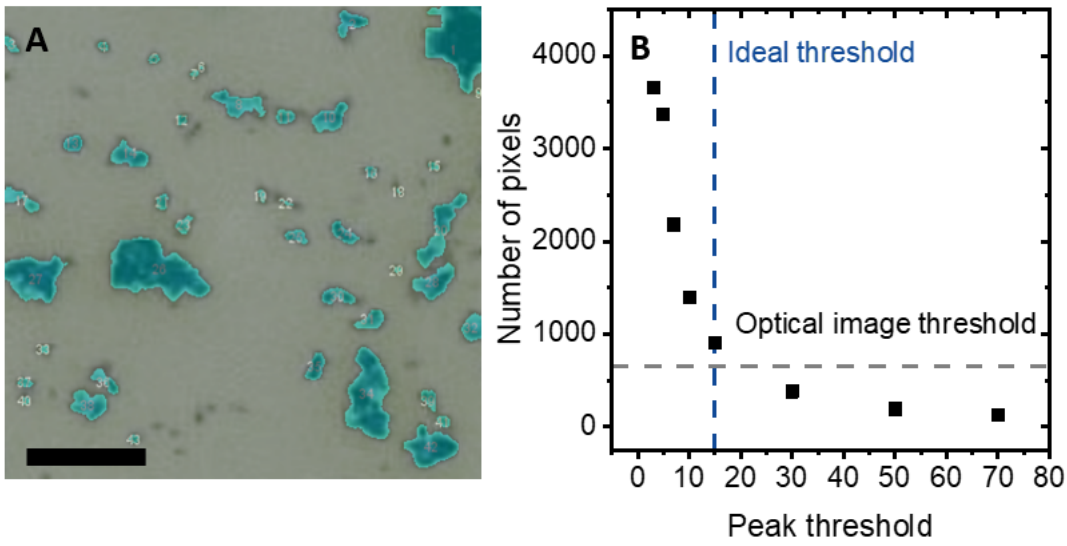

Figure 5.6: **A:** Optical micrograph of the sample region mapped. Overlaid image is the thresholded image used to calculate the area fraction occupied by the nanosheets (blue hue). Scale bar is 5 µm. **B:** Plot of number of pixels containing information used for creating the histogram versus peak threshold set for data extraction.

The peak threshold set for extracting the values corresponding to the necessary Raman modes for graphene influences the resulting distributions. If the threshold is set too low, noise values will be included in the calculations. If the threshold it too high, only multilayer nanosheets will be accounted for and skew the measurements towards higher averages (as discussed in Figure 5.5). The optimal threshold is set based on matching the area fraction of pixels included in the distribution analysis to the area fraction measured from a thresholded version of the optical micrograph for the sample (as seen in Figure 5.6A). The image was thresholded using the software ImageJ 1.51q. Figure 5.6B shows a plot of the number of pixels used for the calculations for each peak threshold. Dashed lines represent the optical image and the ideal thresholds. The optimum value is set lower to the actual optical image threshold as monolayers are often difficult to image due to the low optical contrast on the substrate used (Si wafer).

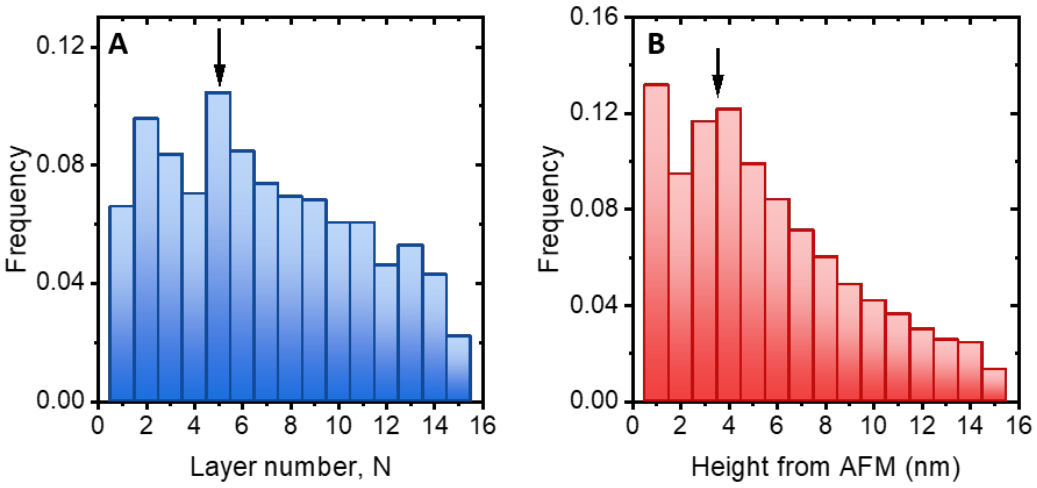

Figure 5.7: Comparison of **A** Raman-derived layer number distribution from the map (Figure 5.4) with **B** pixel height histogram based on AFM data.

Applying appropriate metrics to the data in a pixel-wise fashion, binning the resulting layer numbers and lateral sizes produces distributions representing the population of nanosheets. These are shown in Figure 5.7A and 5.8, and are distributions by particle area rather than number or volume, due to the measurement approach. Figure 5.7 compares the Raman-derived layer number distribution (panel A) to the AFM pixel height distribution (panel B), which suggests that the apparent interlayer spacing is in the range 0.7 to 0.8 nm; agreeing well with previous measurements for LPE graphene [128, 116].

The interlayer spacing measured on this sample differs from the expected value of 0.335 nm for interlayer carbon atom distance in graphite crystals [216]. The conversion between measured height and layer number is known to be both sample and measurement dependent. For example, a layer of surfactant or trapped solvent contribute to the apparent height in nanosheets [128]. An additional factor is the choice in parameters for the AFM measurements. Increasing the peak force set point, which increases the pressure applied by the tip, has been shown to improve accuracy in the measurements for monolayers but the effect is unknown for multilayer nanosheets and additional characterisation is necessary [182, 217].

The average of the layer number distribution in Figure 5.7A is $\langle N \rangle = 6.9$, however applying the metric to the averaged spectrum for the whole map (shown in Figure 5.1)

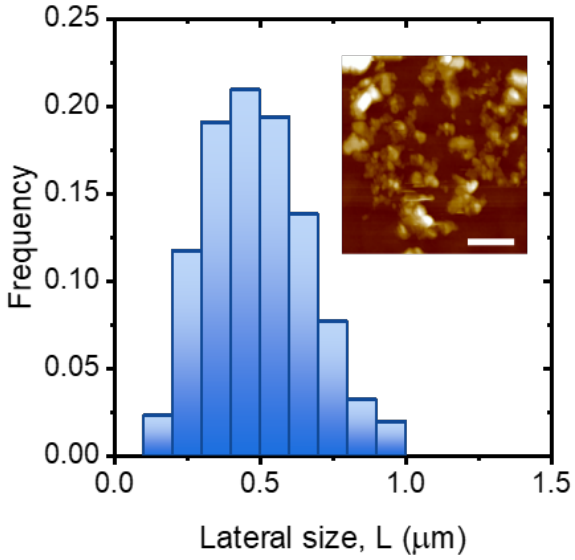

Figure 5.8: Metric-derived nanosheet lateral size distribution based on analogous analysis of the D/G peak intensity ratio (inset) AFM of a 2x2 μm area of the same sample. The scale bar is 500 nm.

the average is $\langle N \rangle = 8.7$. This large over-estimation reflects the idea that, in samples with broad distributions of layer number, the thicker multilayers contribute more significantly to the overall sample signal, thereby skewing results towards greater $\langle N \rangle$. Figure 5.8 shows the distribution of lateral size obtained from the present Raman metric. The inset shows AFM data of the film, where the scale bar is equal to the average lateral size estimated from the Raman-derived distribution (500 nm). Applying the mapping approach described here in association with the metrics calibrated against AFM measurements improves reliability and also extract more information regarding the approximate distributions of length and thickness. Reconstruction of population distributions would require one nanosheet per pixel. The present method obtains the greatest amount of information possible when practical considerations are made, particularly the time required to achieve high enough statistical power and the challenges of producing sparse enough samples for high-quality measurements to be obtained.

5.4 Extension to MoS_2

The same mapping methodology can be applied to MoS_2, the well-studied archetypal TMD [7, 65, 6]. MoS_2 is a layered semiconducting nanomaterial, with an indirect bandgap of 1.2 eV in the bulk that shifts to a direct gap of 1.95 eV in the monolayer [218]. Non-resonant Raman spectroscopy reveals two main vibrational modes: E^1_{2g}, corresponding to in-plane lattice vibrations and A_{1g}, the out-of-plane vibrations (notation used is according to representations of the D_{6H} group used for bulk-like MoS_2 [67]). Additional information can be gained through the use of resonant Raman spectroscopy, where resonance of the excitation with an electronic transition amplifies signal intensity and relaxes the selection rules for Raman scattering, allowing multi-phonon processes [219]. Second-order Raman scattering processes are enhanced by the coupling of phonon modes to optically-excited electronic states [220]. In the case of MoS_2, the presence of an exciton absorption near 670 nm [6] (1.86 eV, very weakly dependent on layer number) facilitates resonant excitation using a 660 nm (1.88 eV) laser. Resonant and non-resonant (532 nm, or 2.33 eV, excitation) spectra of a film prepared from an LPE dispersion are shown in Figure 5.9.

Raman shifts and respective mode assignments are in the Table 5.1. For the non-resonant spectrum, the two expected modes are visible in addition to modes associated with the silicon substrate. The resonant spectrum is more complex; in addition to the main modes, an intense peak usually assigned to the second-order longitudinal acoustic mode at the M point, 2LA(M) (around 460 cm^{-1}), is observed. Other additional vibrations at higher Raman shift are associated with combination modes involving the LA(M) mode [218].

It is known that the E^1_{2g} mode softens for increasing number of layers while the A_{1g} mode stiffens, although only in the few-layer limit ($N <\sim 10$). The resulting increase in peak separation between the main modes with increasing number of layers may be used for characterising MoS_2 nanosheets. Figure 5.10A shows replotted data for mechanically-exfoliated (ME) nanosheets from Lee *et al.* [9] for two different excitation energies. The peak separation saturates quickly hindering the distinction between number of layers

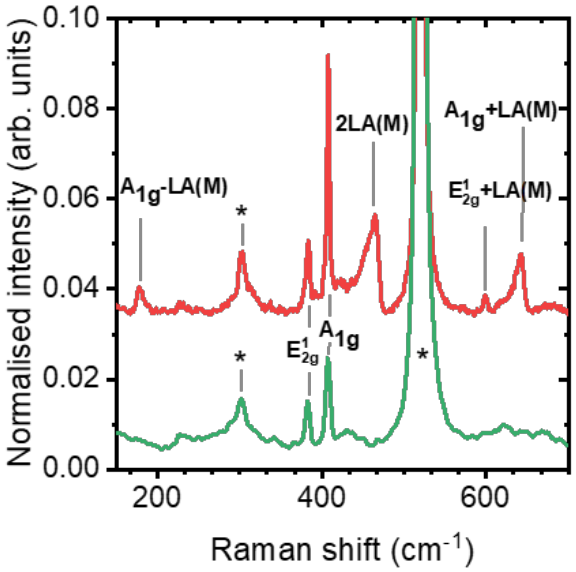

Figure 5.9: Raman spectra of a film of MoS_2 prepared by deposition of a LPE dispersion. Both resonant (red curve) and non-resonant (green) conditions are shown. Peaks were labelled with the associated symmetry group [7, 8]. The peaks attributed to the silicon substrate are indicated with an asterisk (*).

Raman shift (cm^{-1}) (± 0.5)	Mode assignment [8, 7, 65]
178.0	$A_{1g} - LA(M)$
302.2	Substrate
383.2	E^1_{2g}
406.9	A_{1g}
464.7	$2LA(M)$
520.2	Substrate
599.2	$E^1_{2g} + LA(M)$
642.2	$A_{1g} + LA(M)$

Table 5.1: Mode assignment for Raman shift peaks in resonant spectra of MoS_2.

bigger than six. The constants of the fitted functions are laser dependent but the form is the same for both cases: $\Delta\nu = \Delta\nu_{bulk} - Ae^{-N/b}$. Since the fitting relies on characterising the bulk form, Figure 5.10B shows resonant Raman spectra of bulk powder (red) used for LPE experiments and a bulk crystal (black) used for ME. It is noted that the spectra are non-identical even though they are both "bulk" forms of MoS_2. The main difference is that the intensity of the E^1_{2g} mode for the crystal approaches the spectrum baseline. Figures 5.10C and D are optical micrographs, for the crystal and powder, respectively, under the same magnification, highlighting the differences in morphology.

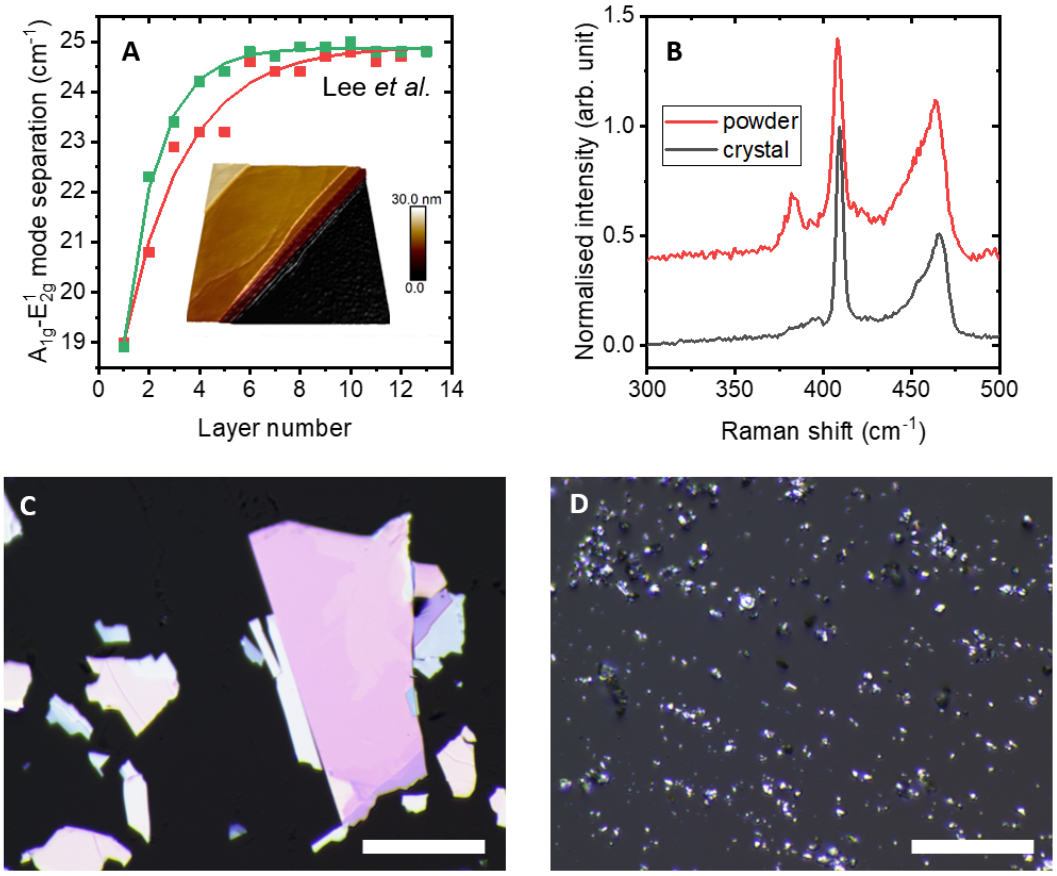

Figure 5.10: **A:** Modification of the A_{1g} and E^1_{2g} modes separation with varying layer number for mechanically-exfoliated MoS_2 (data replotted from Lee *et al.* [9]). Fitted curves are of the form $\Delta\nu = \Delta\nu_{bulk} - Ae^{-N/b}$. Inset includes a 3D plot of an AFM micrograph showing distinct plateaux corresponding to different layers in a mechanically-exfoliated sample. **B:** Raman spectra of bulk MoS_2: crystal used for ME (black) and powder used for LPE (in red). **C:** Optical micrographs of the MoS_2 crystal **D:** and the powder at the same magnification. Scale bar is 20 µm.

Another influence affecting the main mode positions is the defect density. A plot of A_{1g} and E^1_{2g} mode separation for a monolayer with varying inter-defect distance is shown in Figure 5.11A; data replotted from Mignuzzi *et al.* [10]. The region coloured red represents where the literature metric assigns the monolayer as a bulk-like sheet. The orange region is from 1.5 layers up to bulk, representing an inaccurate assignment of layer number for few-layered sheets. Figure 5.11B shows the increase in FWHM for both main MoS_2 modes with increasing inter-defect distance. Mignuzzi *et al.* showed that the peak can no longer be fitted with just one feature but the crystallographic assignment of these modes is unclear. The effect of defects in the Raman spectrum is usually neglected, unless defects

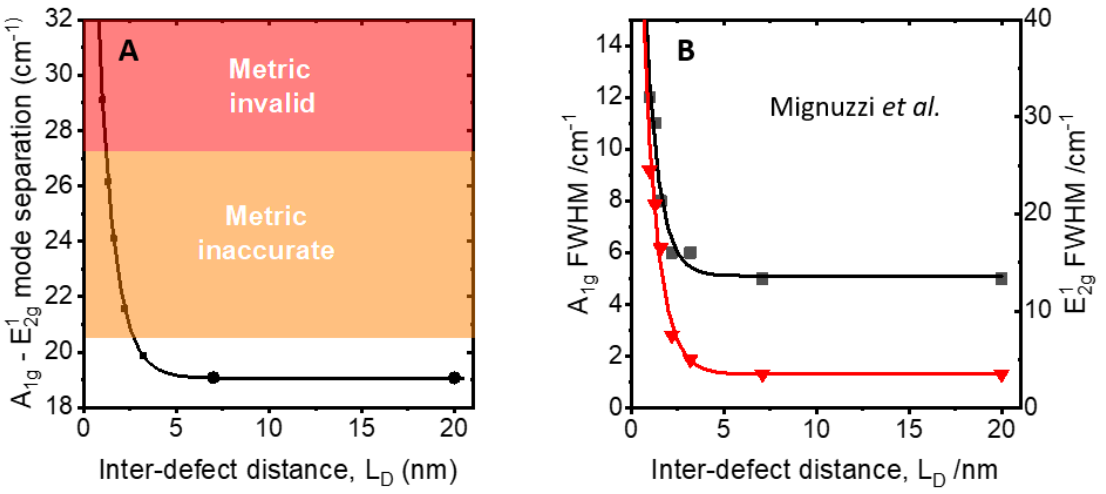

Figure 5.11: **A:** Measure modification to the mode separation in monolayer MoS_2, as a function of inter-defect distance L_D, based on spectra from Mignuzzi *et al.* [10]. Highlighted areas show where the mode separation metric showed in Figure 5.10 becomes inaccurate and invalid. **B** Measurements of the full width at half maximum (FWHM) for the A_{1g} and E^1_{2g} Raman modes with L_D based on the same data.

are the focus of the study. Defects, mainly in the form of single sulfur vacancies, where studied in as-exfoliated ME sheets using Scanning Tunneling Microscopy by Vancsó *et al.* [221]. They found an intrinsic defect concentration in the order of 10^{13} cm^{-2}, resulting in an inter-defect distance of about 2 nm (Appendix A) for samples usually considered defect-free and perfectly stacked crystals. Due to the nature of the ultrasonication process that balances peeling and tearing during exfoliation, it is expected that LPE nanosheets will have an even lower intrinsic inter-defect distance.

Figure 5.12A illustrates the shifts observed as a function of applied uniaxial strain (data replotted from Rice *et al.* [11]). The A_{1g} remains almost unchanged whilst a shift is observed for the E^1_{2g} mode. The E^1_{2g} mode is double degenerate in-plane vibration in the xy-plane. Splitting of this mode under unaxial strain is expected since this effect was observed in the equivalent mode in graphene [67]. However, this splitting is yet to be observed experimentally. Understanding the shifts due to strain can be used to determine the stress transfer to the nanosheets in polymer composites [222], an important factor when incorporating nanomaterials into devices.

Figure 5.12B shows the shifts mainly for the A_{1g} mode with doping (data replotted from Chakraborty *et al.* [12]). They used a top gated single layer MoS_2 transistor on a doped *p*-type silicon substrate and a solid polymer electrolyte comprised of a mixture of $LiClO_4$ and polyethylene oxide. Doping layered nanomaterials is a useful way to tune their optoelectronic and chemical properties by varying dopants, increasing their applications.

Even though the metric using the A_{1g} and E^1_{2g} mode separation is useful, some effects that cause shifts to the peak positions are often neglected, and can significantly complicate the interpretation of measurements, as Figures 5.11 and 5.12 demonstrate.

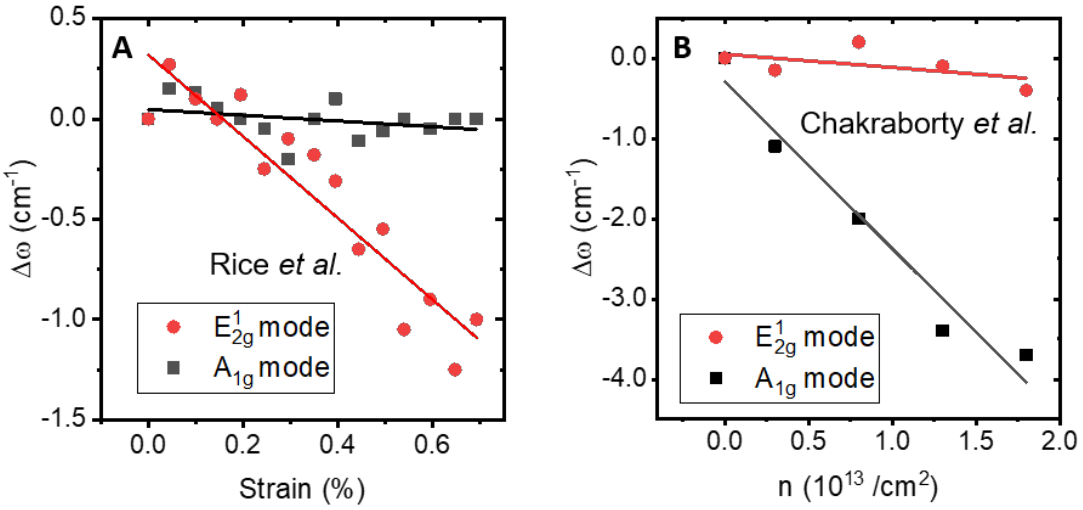

Figure 5.12: The main modes separation is plotted as a function of **A** applied unaxial strain (replotted data from Rice *et al.* [11]) and **B** doping (replotted data from Chakraborty *et al.* [12]).

5.5 Conclusions

Raman spectroscopy is a powerful, non-destructive characterisation technique. Applying microscopic calibrated metrics as a map yields information in the form of histograms that reconstructs distributions of size and thickness, not only averages, as demonstrated for LPE graphene. By decreasing the number of nanosheets under the laser focal spot with resolution-limited pixel size, the resulting spectra are close to the true representations of the sample and not skewed towards thicker multilayer sheets. Therefore, the method

works better even for a broad distribution of sizes. The logical extension of the same pixel-wise analysis to MoS_2 proves to be challenging due to a lack of appropriately robust Raman metrics by which materials can be characterised. Current literature metric for layer number relies on the peak separation between the main modes and those positions shift as a consequence of effects modifying the crystal structure such as defects, strain, and doping. Therefore, a more robust metric is necessary to decouple external stimuli and intrinsic properties of the material. Also, a length metric for LPE MoS_2 is not present in the literature, hindering the direct mapping analysis.

Chapter 6

Development of novel Raman metrics for layer number and size of MoS_2 nanosheets

Accurate size and layer number measurements are crucial for nanomaterials research, especially for applications in which varying those parameters results in different performance. Microscopy characterisation provides information about the distributions of both quantities, however it is time-consuming and dependent on specific sample preparation. Spectroscopic techniques, such as Raman spectroscopy, can be calibrated in association with microscopic measurements. Here, using the mapping analysis developed in the previous chapter, a metric for layer number of both LPE and ME MoS_2 sheets was developed using a ratio of two resonant modes. The influence of focal depth and objective chosen for the maps is evaluated for the present metric. The same mapping approach with microscopic calibration was used to develop a length metric for LPE nanosheets, using a ratio of two Raman modes. The equations can easily reconstruct layer number and size distributions but also be applied to single point spectra. Average scaling was compared to other characterisation techniques for samples of an LCC series. Both metrics were used to re-evaluate the acetone-exfoliated MoS_2 nanosheets studied in a previous chapter. The same approach was applied for a

layered double-hydroxide, $CuOH_2$, which yielded a length metric as well, showing that the analysis is not specific to MoS_2 but it can be extended to other layered materials.

6.1 Introduction

Microscopy-based characterisation provides complete information regarding layer number and length distributions. AFM requires sparse films and isolated nanosheets, which can be achieved by hot plate deposition of diluted dispersions. For proper statistics, at least 100 nanosheets should be measured, and even more for samples known to have a broad distribution of sizes [125]. This approach is laborious as every nanosheet has to be measured individually for length, width, and thickness. TEM is quicker for micrograph acquisition but can only yield thickness measurements for specifically placed few-layered nanosheets [125]. Even though spectroscopy techniques provide volume averages, and not number-averages, more representative analysis can be developed in association with microscopic verification, as has been done for graphene [136, 64, 223] and MoS_2 (using UV-vis spectroscopy) [6]. Raman spectroscopy is a powerful non-destructive characterisation tool with high-throughput and yet Raman-based metrics for various layered materials and different exfoliation techniques are underdeveloped. In this chapter, both metrics and a methodology for understanding nanosheet size and thickness distributions are developed.

6.2 Layer number metric

In order to investigate alternative approaches to current literature metrics, ME MoS_2 was studied. This process is known for producing large and well-exfoliated nanosheets. By investigating this system initially, edge and length effects on the Raman spectra are dismissed and the primary influence comes from the layer number. Figure 6.1 shows resonant spectra of various sheets normalised to the A_{1g} mode for different numbers of layers, measured by AFM. The main variation is associated with the 2LA(M) feature, which is actually comprised of two different modes: one centred at 453 cm^{-1} and the other at 465 cm^{-1}, where their relative intensity appears to be determined by the layer number.

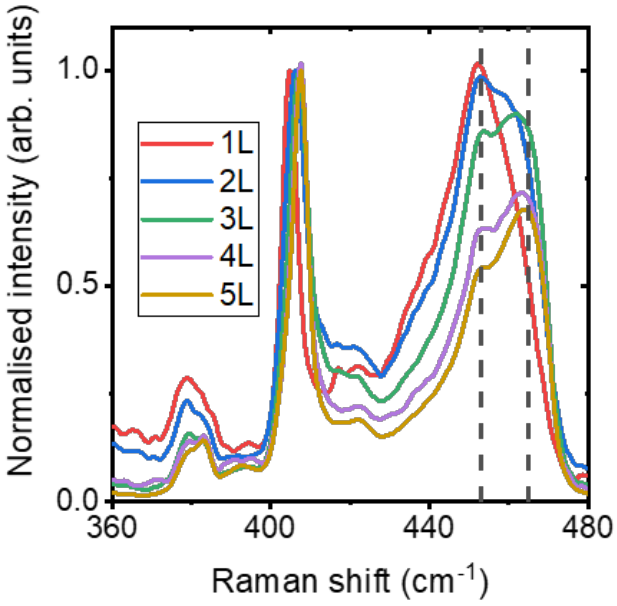

Figure 6.1: Normalised Raman spectra for ME nanosheets of varying layer number. Dashed lines indicate the positions of Raman features at 453 and 465 cm^{-1}.

The first peak is usually associated with the 2LA(M) mode and the second one does not have a formally-agreed assignment in the literature. It might be associated with an infrared active mode (A_{2u}) [218, 224] or a mode involving an acoustic vibration [220, 225]).

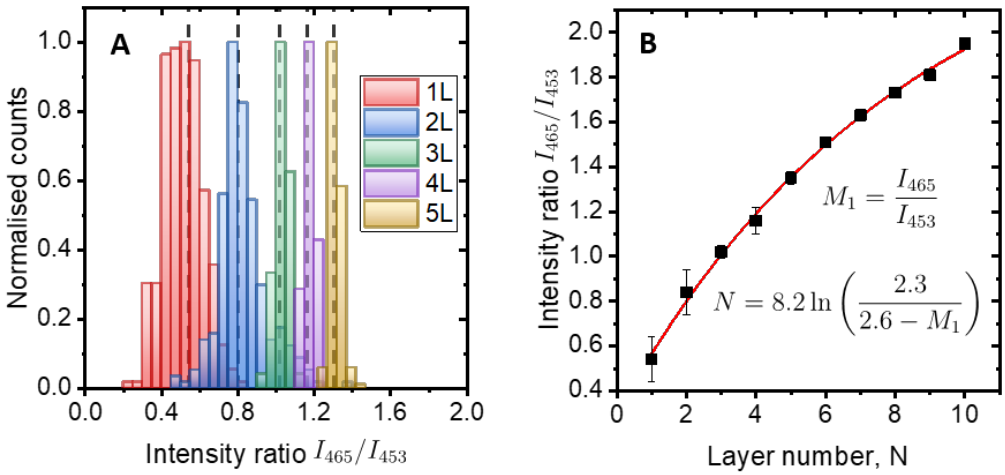

Figure 6.2: **A:** Histograms of the intensity ratio I_{465}/I_{453} plotted from different maps of ME samples with varying number of layers. **B:** Graph of layer number against the centre of the histograms in B. The fitted function is of the same form as peak separation metric, with the inverted equation shown.

Histograms of the intensity ratio I_{465}/I_{453} for maps of several ME sheets with known layer number are shown in Figure 6.2A. The maps were done following the procedure described in Chapter 5. The resulting histograms have a narrow distribution with non-overlapping centres.

Plotting the mean I_{465}/I_{453} ratio of each distribution against the layer number for the corresponding sample allows a metric equation fitting of the same form as the A_{1g} and E^1_{2g} mode separation ($\Delta\nu = \Delta\nu_{bulk} - Ae^{-N/b}$) but with the advantage of avoiding effects that influence peak positions by using an intensity ratio; this is shown in 6.2B. Having measured the ratio I_{465}/I_{453}, the following equation returns the layer number:

$$N = 8.2 \ln\left(\frac{2.3}{2.6 - I_{465}/I_{453}}\right) \tag{6.1}$$

This equation was developed using a mapping analysis and it can reconstruct the approximate distribution this way, however it can determine layer number accurately for single-point spectra as well. The fitting parameters and respective uncertainties are: (8.2 ± 1.1); (2.30 ± 0.13); (2.60 ± 0.16).

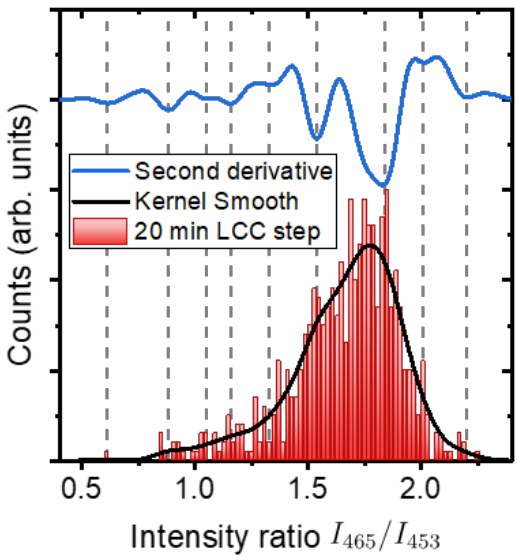

Figure 6.3: Histogram of the I_{465}/I_{453} ratio for an LCC step of LPE nanosheets with a broad distribution of layer number. Second derivative curve (blue) of smoothed histogram (black) is shown. Dashed lines indicate peak positions, in agreement with data for ME sheets.

Histograms of the I_{465}/I_{453} ratio were plotted for every sample in a liquid cascade centrifugation (LCC) experiment using LPE MoS_2 and the mapping methodology described in Chapter 5. LCC selects different fractions from the broad distribution of sizes and thicknesses produced by LPE using sequential centrifugation steps (from 9 min to 12 h, at 3000 g) [47], as described in Chapter 3. The histograms were smoothed using a weighted average of adjacent points (kernel smooth technique). The second derivative of the resulting curve indicates, from the local minima, the position of underlying peaks in the data, even if they are not resolved. Figure 6.3 shows the raw histogram, kernel-smoothed curve, and second derivative for one LPE sample with a broad distribution of I_{465}/I_{453} ratios.

Layer number	Metric value	Second derivative measurement
1	0.54	0.61
2	0.84	0.88
3	1.02	1.05
4	1.16	1.16
5	1.35	1.33
6	1.51	1.54
7	1.63	-
8	1.73	-
9	1.81	1.84
10	1.95	-
11	2.00	2.01
12	2.07	-
13	2.13	-
14	2.18	2.20

Table 6.1: Table for Figure 6.3 (20 min LCC step) sample.

Table 6.1 shows the peak positions identified in the histogram analysis. There is exceptional agreement between the ratios for both LPE and ME techniques, as seen in Figure 6.4. The LCC series of a LPE MoS_2 dispersion produced ten different histograms of the intensity ratio I_{465}/I_{453} with varying distributions. The histograms were smoothed (kernel-smooth technique using Origin, OriginLab) and then the second derivative was plotted to determine every underlying feature in the distributions. The centre of every maximum found for the LCC series is plotted, in ascending order, in Figure 6.4. The points representing LPE features are clustered around the ME features (solid lines) forming a step-like plot analogous to those seen when analysing inter-layer spacing by AFM.

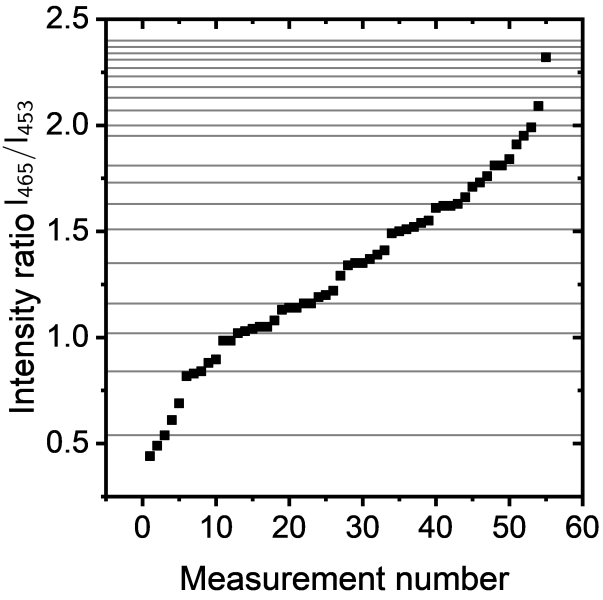

Figure 6.4: Plot of the peak positions for the intensity ratio I_{465}/I_{453} in a LCC series of LPE samples. Lines represent the position for the peaks in ME nanosheets.

The agreement between ME and LPE samples highlights that even though the exfoliation processes are different, the same variation in the Raman spectra is observed with layer number. Also, it indicates the robustness of the metric in comparison to the literature approach because ME sheets will have varying degrees and orientation of strain, which should be different for solution-processed nanosheets.

Figure 6.5A shows a large data set which comprises many isolated ME nanosheets. Sample has a broad distribution of size and layer number (Figure 6.5B). Figure 6.5C shows an analysis of the feature positions within the 2LA(M) band. There are two clear features normally-distributed about the centre positions ~ 465 and $\sim 453\,\mathrm{cm}^{-1}$. ME sheets should have different degrees and orientations of strain due to the process by which they are transferred to the substrate. The fact that the feature positions are approximately the same as those observed for LPE nanosheets highlights the robustness of the present metric.

This allows the I_{465}/I_{453} intensity ratio to be used as a metric to analyse layer number distributions for both LPE and ME nanosheets. The fitting constant multiplying the independent variable in the exponential form $y = y_0 - Ae^{-(x-x_0)/b}$ indicates the applicable range for our metric. This constant is 8.2 for our fitting, allowing measurement up to $\sim$ 16

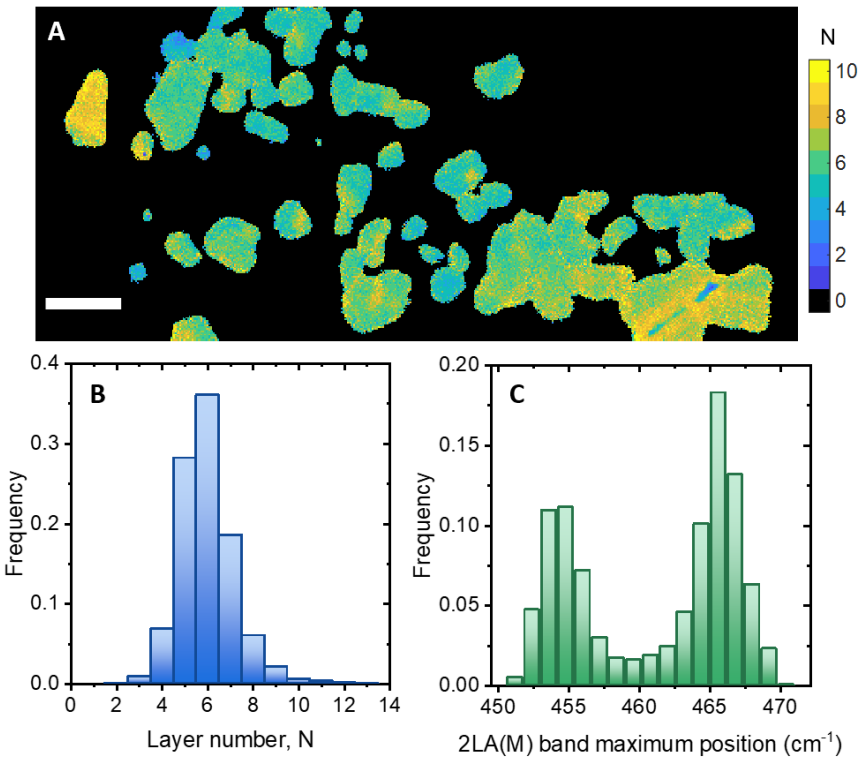

Figure 6.5: **A:** Raman map colour coded according to layer number for a large area of a ME sample. Scale bar is 10 µm. **B:** Histogram of layer number using present metric and **C:** position of maximum around the 2LA(M) feature.

layers before the exponential scaling makes layer numbers indistinguishable. The same constant for the literature metrics presented in Chapter 5 is 2.2, so that limit is closer to 5.

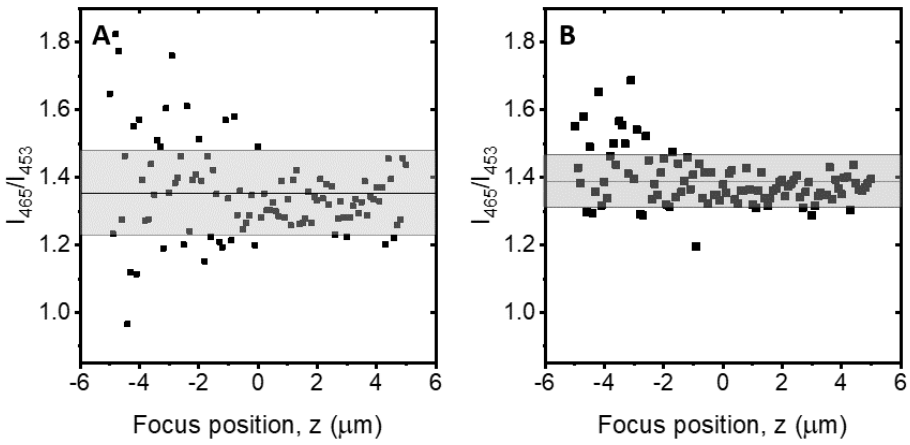

Figure 6.6: The intensity ratio I_{465}/I_{453} plotted as a function of focus position for **A:** baseline-subtracted spectra and **B:** additional smoothing. Y-axis scale is the same for both plots.

It is interesting to note that the relative intensities of these modes is fully independent of laser focus, as seen in the Figure 6.6. The Raman spectra were always baselined and smoothed before the MATLAB analysis, as explained in Chapter 5. The baseline was removed using the software provided by the manufacturer with the spectrometer and it is useful to compare only the differences in the modes, removing any ratio shifts caused by different baselines. Figure 6.6A shows the intensity ratio I_{465}/I_{453} used for the layer number metric as a function of focus position in the z-direction for spectra that had the baseline subtracted. Figure 6.6B is the same data set but with further smoothing to remove any discrepancies caused by noise in the measurement. For the non-smoothed plot, the average intensity ratio is 1.35 ± 0.14, whilst the average for the smoothed plot is 1.388 ± 0.077. For both plots, there is a larger spread in the data for negative positions in the z-direction, which means the focus was below the sample. Since the spectrometer is confocal, the depth of focus, excluding any sample specific effects, can be calculated using the following equation [226]:

$$\text{Depth of focus} = \frac{4\lambda}{NA^2} \tag{6.2}$$

For the laser and objective combination used in this experiment, the depth of focus is 3.65 µm, explaining the noise for those negative positions. It is interesting to note that the layer number associated with the intensity ratio I_{465}/I_{453} is 5 layers for both plots, showing that the smoothing approach used does not compromise the accuracy of the layer number interpretations based on this metric quantity.

Figure 6.7A shows an optical micrograph and overlaid Raman map colour coded according to the number of layers. The Raman layer number distribution is compared with AFM measurements for the same sample in Figure 6.7B and the agreement is very good.

Figure 6.8 is a plot of average layer number for Raman (from present metric) and AFM statistics. Both techniques show good agreement for few-layered nanosheets. The average for AFM measurements is higher than 10 layers for the first three steps in the LCC series. One factor to consider is the metric limit. Since it was determined that it can measure up to

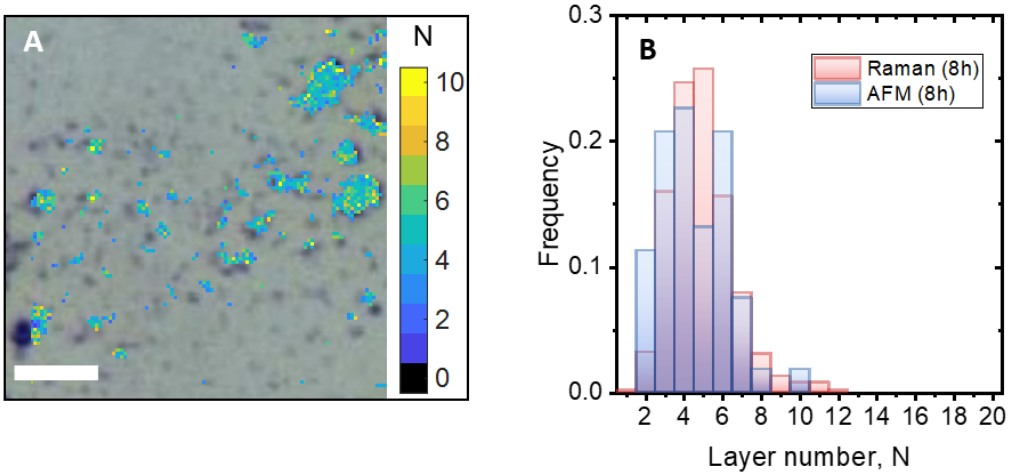

Figure 6.7: **A:** Optical micrograph overlaid with corresponding Raman map of a 20 µm by 20 µm area of an LPE sample. Raman map is colour coded according to the layer number metric in **D**. Scale bar is 5 µm. **B:** Plots of layer number distribution from AFM (red) and the present Raman metric (blue) for the same LPE sample shown in panel **A**.

16 layers, for broad distributions, which tend to be approximately symmetrical, the average will be around 8 layers, as the figure shows.

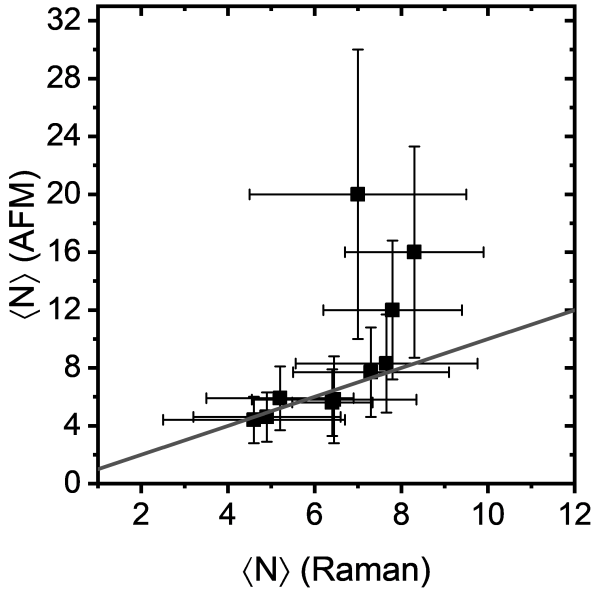

Figure 6.8: Plot of average layer number for Raman and AFM. Solid line is the $y = x$ curve.

The same magnification study performed in Chapter 5 for graphene was repeated with the newly developed MoS_2 metric. The same area of a 12 min LCC MoS_2 sample was mapped and the results are shown in Figure 6.9. Figure 6.9A is the Raman mapping for the 20x, NA 0.4 objective and Figure 6.9B is the 100x, NA 0.85 objective. The loss in mapping resolution is obvious, as features easily resolvable using a high magnification are not clear for the other. Figure 6.9C shows the histogram of layer number for both maps. They were normalised to the bin with highest number of counts to highlight the observed difference. Both histograms have the same general trend for layer number near the histogram average; however, high magnification has higher counts for thin nanosheets. The highest resolution possible ensures the correct estimation of layer number. Incorrect measurements may influence the judgement on performance for thickness-sensitive applications and any dominated by available surface area.

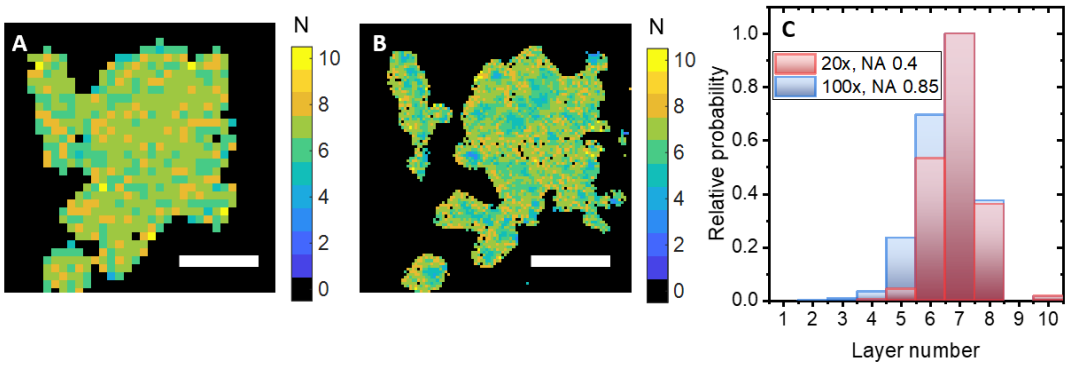

Figure 6.9: Raman mapping of the same area of a MoS_2 sample using different objectives: **A:** 20x, NA 0.4 and **B:** 100x, NA 0.85. The scale bar is 5 µm for both panels. **C:** Comparison between the layer number distributions obtained from those maps.

6.3 Length metric

A length metric for MoS_2 may be developed based on an analogous analysis to that employed for graphene [64]. For graphene, the intensity ratio of the G and D modes is used. The G mode written as an irreducible representation is of the form E_{2g}, which may be compared to the E^1_{2g} mode in TMDs since they both involve in-plane vibrations [67].

The D band in graphene is a disorder-induced vibration and a similar feature in TMDs is the LA(M) mode, around 225 cm^{-1}. However, this vibration is absent in our measurements of pristine MoS_2. This mode is observed in the literature when there are defects with dangling bonds [227].

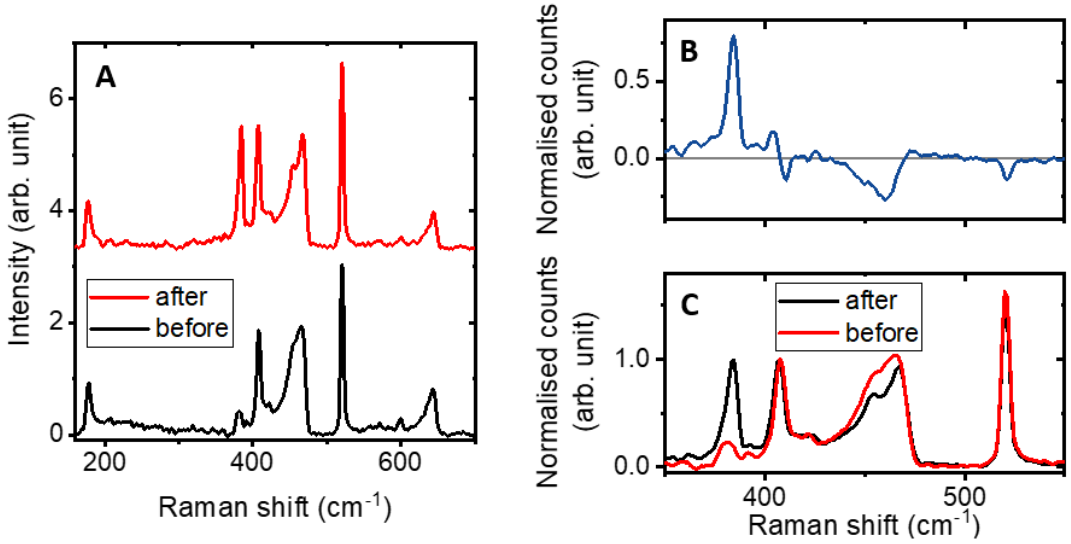

Figure 6.10: **A:** Raman spectra before (black) and after (red) inducing defects on a ME nanosheets with a laser. The relative increase in intensity of the E^1_{2g} mode is correlated with an increasing number of defects. **B:** Resulting spectrum when subtracting the before from the after spectrum. **C:** Before and after spectra normalised to the A_{1g} mode.

In order to find an alternative defect-enhanced mode, a study based on laser damage was performed on ME nanosheets and the results shown in Figure 6.10A. Spectra were taken before and after the laser was left on for 1 s at high power, an approach seen in literature to study laser-induced damage [153, 154, 155]. There is a significant change in the relative intensity of the A_{1g} and E^1_{2g} modes, with the E^1_{2g} intensity increasing significantly as the laser induces basal plane damage. In order to investigate any other changes to the spectrum, the normalised to the A_{1g} mode black spectrum was subtracted from the red, resulting in the blue curve shown in Figure 6.10B.

The most prominent change is the obvious variation in the E^1_{2g} mode intensity. The A_{1g} mode shifts whilst the Si mode at 520 cm^{-1} becomes more intense after the laser treatment. It is also clear that both modes near the 2LA(M) peak change in intensity. The normalised spectra are shown in Figure 6.10C. Evaluating the peak shifts of the main modes, it is noted

that they peak difference varies from 26.6 to 23.6 cm^{-1}. Applying the newly-developed metric using the intensity ratio I_{465}/I_{453}, it is possible to see a change in layer number from 5.2 to 4.6. The Si peak intensity variation can be correlated with thickness of the MoS_2 nanosheet through the absorption coefficient [228]. The calculation is shown in Appendix B but the result is a difference comparable to one interlayer spacing in MoS_2. However, the laser ablation does not explain the difference in E^1_{2g} mode intensity. Therefore, defects must have been induced to the nanosheet as well.

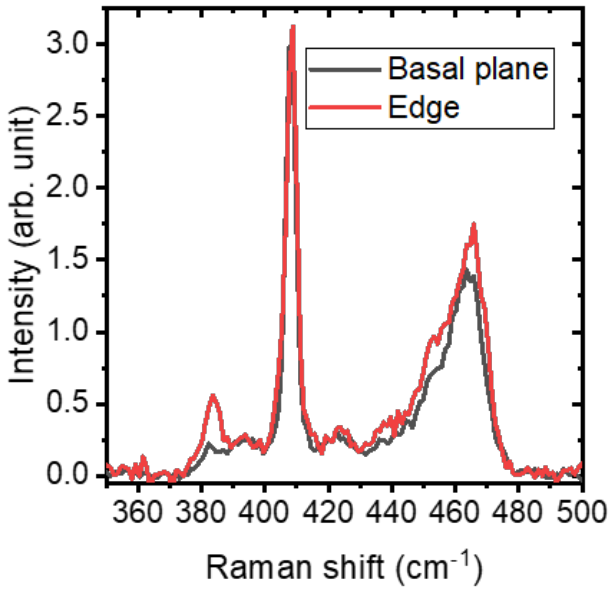

Figure 6.11: Raman spectra after electrochemical oxidation at different regions of an ME sheet: basal plane and edges. An increase in the E^1_{2g} mode intensity is clear.

An experiment of electrochemical oxidation of ME sheets was performed, following a similar approach seen in literature [82, 203]. The ME sheets exfoliated using the Scotch tape method and were transferred to a gold substrate, covered in ionic liquid (lithium perchlorate dissolved in ethylene glycol) and a voltage of 3.0 V was applied to the sample. Figure 6.11 shows the difference between spectra taken at the edges and on the basal plane of the sheet after bias was applied. The two obvious differences on the raw data shown there, are the changes in the E^1_{2g} mode and the 2LA(M). The first one corroborates the result observed with the laser damage study, an increase in the mode intensity with

increasing defects. Applying the metric for layer number on those two spectra shows a change of 9.4 to 7.3 layers. Therefore, sheets are exfoliated at the edges with this treatment, as this was not observed pre-treatment. The same increase in E^1_{2g} intensity at the edges of untreated ME sheets is not observed, however the relative increase for an electrochemical oxidation experiment potentially allude to differences in spectral behaviour with defect type.

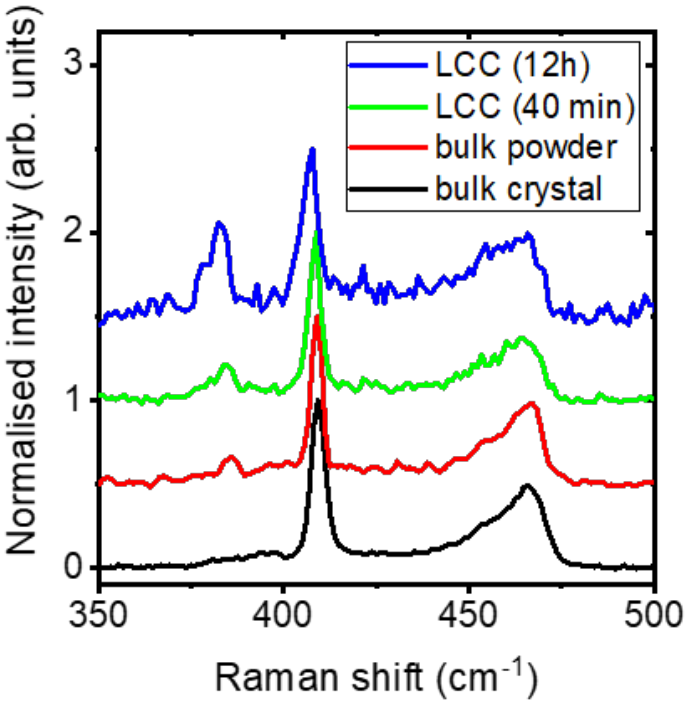

Figure 6.12: Raman spectra of samples with different sizes are shown. The smallest length shown here is represented by the blue curve, followed by the green one. They are both steps in a LCC. LPE bulk powder is in red and ME bulk, black. Decreasing nanosheet size shows increase in relative intensity of the E^1_{2g} mode.

Figure 6.12 illustrates the A_{1g} and E^1_{2g} mode intensity variation for different nanosheet lengths. The average length according to AFM measurements is 85 nm for the smallest fraction in the LCC series, and 171 nm for an intermediate step. Bulk powder used for the LPE experiment is ∼340 nm, while the bulk crystal used for ME is at least two orders of magnitude larger. The intensity of the E^1_{2g} mode increases monotonically with decreasing nanosheet length, corroborating measurements by Huang *et al.* [227] at the edges and

basal planes of mono and bilayer MoS_2. Considering the nanosheet edges to have a higher defect density than the basal plane, it is clear that defect-related modes would be more prominent for smaller sheets, where the ratio of perimeter to basal plane area is greater [64]. The resulting enhancement of the in-plane vibration, in principle, should allow the use of the A_{1g} and E^1_{2g} mode intensities as an analogous sheet length metric to that for graphene.

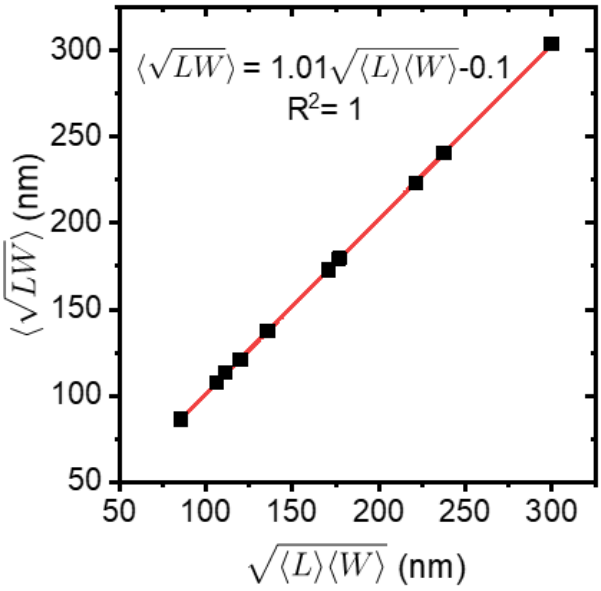

Figure 6.13: Plot of characteristic length defined as the square root of the averages versus the average of the square root.

For nanosheets, neither length nor width are representative of the actual size, since they tend to have an aspect ratio that deviates from unity. Therefore, a better representation of the nanosheets is a characteristic length defined as $\langle\sqrt{LW}\rangle$, where L is the nanosheet length and W is the width [106]. Both dimensions are correlated through an average lateral aspect ratio [144]. Since both quantities are not independent, it was tested defining the average characteristic length by doing the square root before or after averaging the particle-wise product LW. The results are shown in Figure 6.13. The data show that, although L and W are known to share an average relationship $\langle L\rangle \sim \alpha\langle W\rangle$, the two are still to a large extent statistically independent.

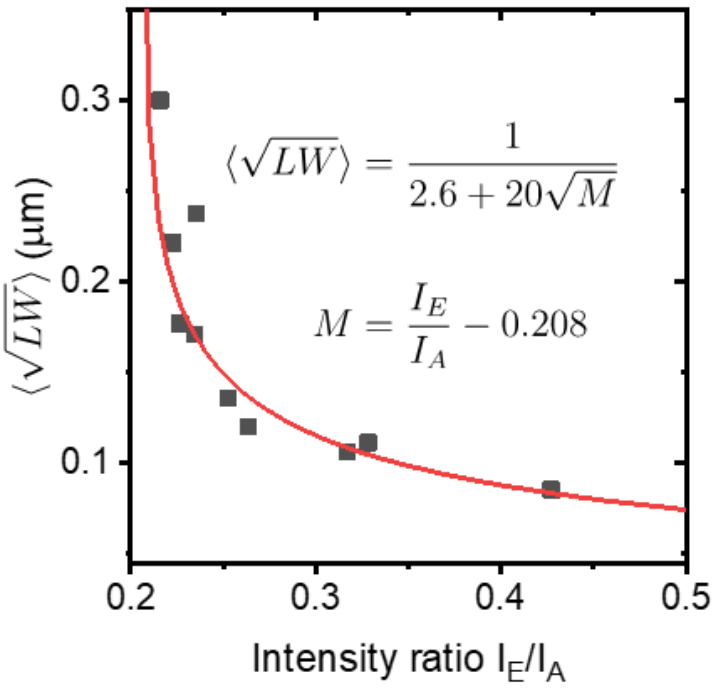

Figure 6.14: Plot of the main modes intensity ratio (I_E/I_A) against the inverse of the characteristic length.

A plot of the relative intensity ratio between the main modes (I_E/I_A) against the characteristic length, obtained from AFM micrographs, is shown in Figure 6.14. The fitted equation is:

$$\langle\sqrt{LW}\rangle = \frac{1}{2.6 + 20\sqrt{\frac{I_E}{I_A} - 0.208}} \tag{6.3}$$

In a similar manner to the layer number metric described, this length metric can be used to reconstruct approximate size distributions in association with the mapping analysis described previously but also determine the dimensions for single-point spectrum of LPE MoS_2. The fitting parameters and respective uncertainties are: (2.6 ± 1.3) µm^{-1}; (20.0 ± 4.0) µm^{-1}; (0.208 ± 0.011). This metric cannot measure nanosheets with characteristic length larger than approximately 385 nm (intensity ratio of 0.208), which is equivalent to the bulk powder used for exfoliation, as seen in Figure 6.15.

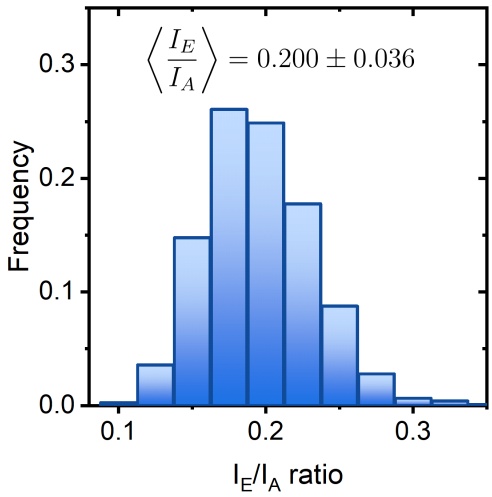

Figure 6.15: Intensity ratio (I_E/I_A) of MoS_2 bulk powder.

A Raman map (20 µm by 20 µm) of a deposited film of LPE MoS_2 is shown in Figure 6.16A with a corresponding optical micrograph. The colour scale indicates the characteristic length determined using equation (6.3). Figure 6.16B shows the length distributions measured by AFM and Raman of the same sample. Appendix C compares the histograms for both characteristic length and layer number using Raman metrics and AFM measurements for every LCC step.

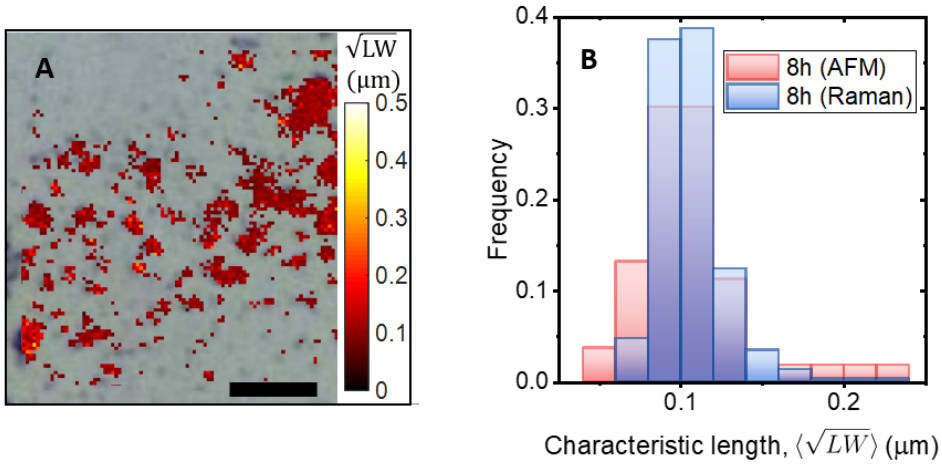

Figure 6.16: **A:** Optical micrograph overlaid with corresponding Raman map of a 20 µm by 20 µm area of a LPE sample. Scale bar is 5 µm. **B:** Histogram of length distribution from AFM (red) and Raman metrics (blue) for the same sample in **A**.

A correlation plot of the averages measured by both techniques for the different fractions is shown in Figure 6.17A, where the error bars are the standard deviations of the measured distributions. These data points indicate strong agreement between the two techniques ($R^2 = 0.71$, excluding the outlier point). Figure 6.17B shows the correlation between distribution standard deviation measurements done using our Raman metric and AFM. The standard deviation of both techniques fall closely around the line $y = x$, except for the first step in the LCC series. Since it has the broadest distribution of the series, the standard deviation is also higher, especially for the AFM measurements, where the presence of aggregates might skew the measurements. These results indicate that the mapping analysis approach is able to correctly capture aspects of the particle size distribution beyond the average value (as is the case with other metric approaches present in the literature to-date) [64, 6, 170].

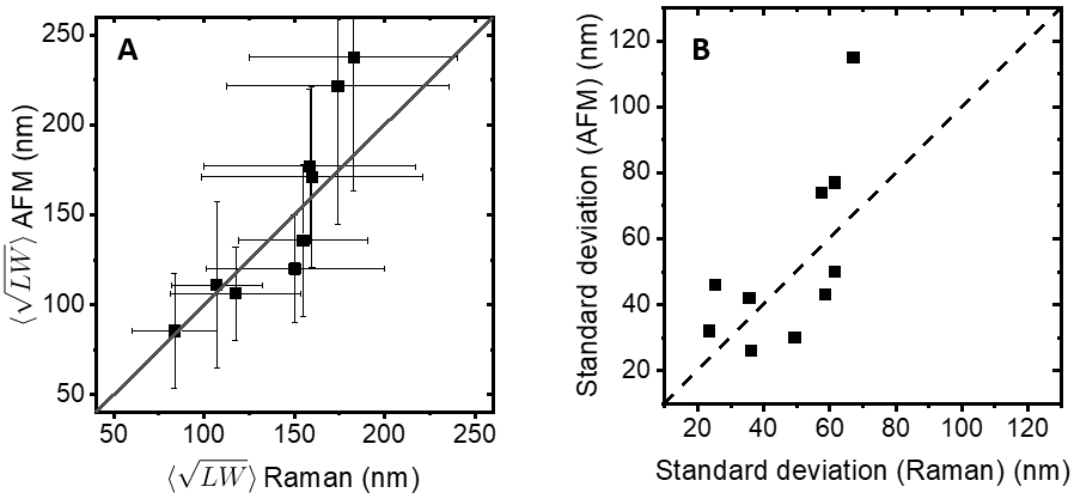

Figure 6.17: **A**: Plot of nanosheets length measured from AFM micrographs and Raman maps showing good correlation between the techniques. **B**: Standard deviation of characteristic length measured by Raman metric and AFM statistics.

The indicative scaling of average layer number and nanosheet volume with increased centrifugation times is shown in Figure 6.18 measured by several different techniques. Both plots show good agreement between spectroscopic and microscopic measurements for few-layered nanosheets, even considering the limitations of the comparison. UV-vis metric is not calibrated above the 10-layer limit [6] and the presence of aggregates skew the

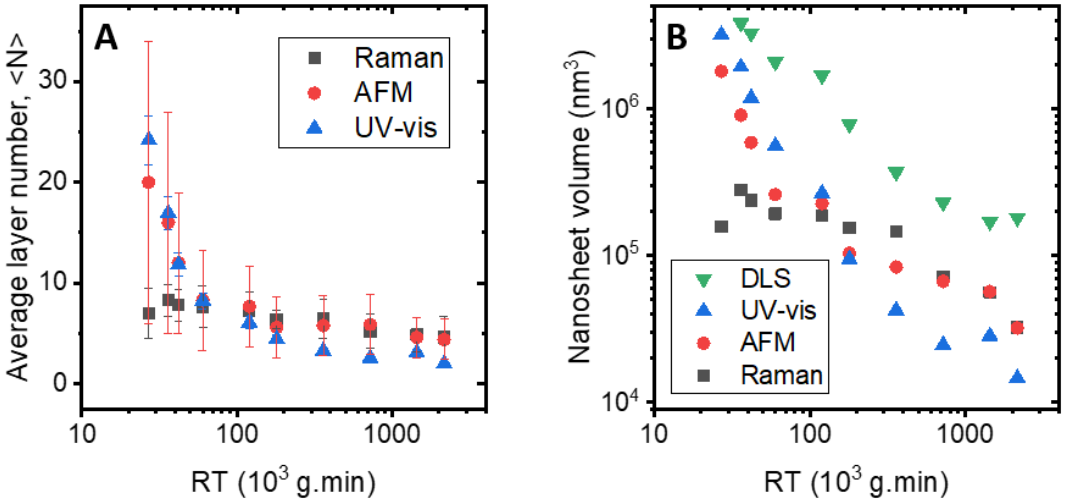

Figure 6.18: **A:** Plot of average layer number and **B:** nanosheet volume as a function of centrifugation parameter using different techniques.

AFM results. In addition to this fact, it is difficult to define a nanosheet volume precisely, based on average length, width, and thickness obtained from layer number.

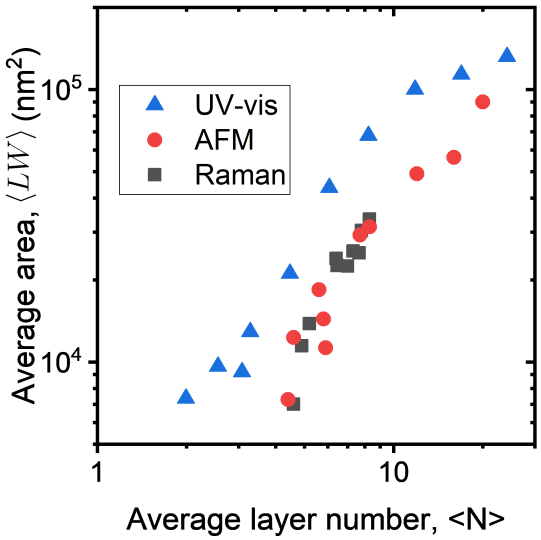

Figure 6.19: Scaling of average nanosheet area with average layer number.

The scaling of average nanosheet area with average layer number using different techniques (Figure 6.19) follows the expected dependence related to the equipartition of energy between tearing and peeling during liquid-phase exfoliation [106].

6.4 Analysis of acetone-exfoliated nanosheets using new metrics

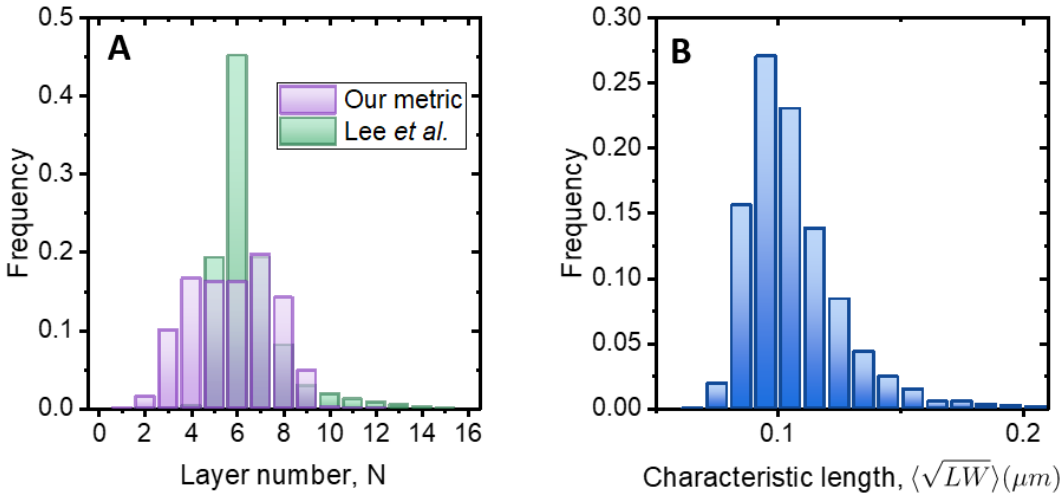

Figure 6.20: **A.** Comparison of layer number distributions obtained using different Raman metrics for the same sample area of acetone-exfoliated nanosheets. **B.** Characteristic length distribution for the same sample, using metric developed in this Chapter.

Figure 6.20 shows the re-evaluation of the acetone-exfoliated MoS_2 nanosheets studied in Chapter 4 using the newly developed Raman metrics. Histograms for layer number are shown in Figure 6.20A using two different Raman metrics. Data in green was obtained using the metric developed by Lee *et al.* [66]. The average layer number for the literature metric is 6.5 ± 1.4, whilst the present metric is 5.8 ± 1.8. For comparison, the UV-vis metric [6] for the same dispersion gives an average of 5.94 ± 0.59. The average values agree within error, however the literature metric fails to detect a substantial proportion of the few-layered nanosheets (two to four layers) and has a higher contribution from bulk-like sheets. This could be explained by the interaction between MoS_2 and the molybdenum oxides. A *p*-doping on MoS_2 was observed for a MoS_2/MoO_3 heterostructure [229], for laser-oxidised MoS_2 monolayer [230], and for few-layer MoS_2 obtained directly from MoO_3 crystals [231]. This type of doping shifts the A_{1g} mode to a higher Raman shift, increasing the peak separation measured.

The characteristic length distribution plot is shown in Figure 6.20B. The average characteristic length $\langle LW \rangle$ is 127 nm, and with a measured L-W aspect ratio of 0.66, the average length $\langle L \rangle$ is estimated to be 156 nm. This value should be comparable to that produced by the UV-vis metric, although the value measured here is 221 nm. Such discrepancy could be explained by the highly-defective oxidised edges of the nanosheets. For this sample, due to the edge-functionalisation, the pure MoS_2 domain is actually smaller than the physical size of the nanosheet. Another effect is that doping affects the FWHM of the A_{1g} mode. The FWHM increases with increasing doping which results in a decrease in mode intensity [12]. Such effect changes the intensity ratio I_E/I_A used for the length calculation, shifting the characteristic length to a smaller value.

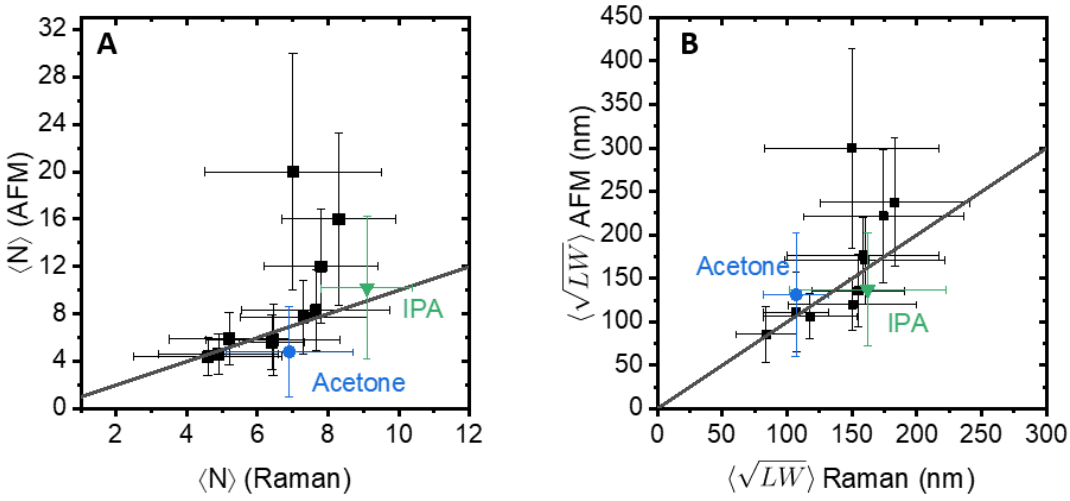

Figure 6.21: **A.** Comparison of average layer number and **B.** characteristic length obtained using the present Raman metrics and AFM characterisation for nanosheets exfoliated in TX-100, acetone, and IPA.

The IPA-exfoliated nanosheets were also re-evaluated the same way. Both Raman and UV-vis metrics length averages were compared to size statistics from AFM micrographs. The obtained characteristic length $\langle \sqrt{LW} \rangle$ was 131, or $\langle L \rangle$ of 161 nm. The resulting average layer number and characteristic length for both solvents were added to the plots mentioned previously containing nanosheets exfoliated in TX-100, as seen in Figure 6.21. The average values follow the $y = x$ curve regardless of the chosen solvent. The only data

point that does not seem to follow the trend is the first step of the LCC of the nanosheets exfoliated in TX-100. This sample has the broadest distribution of sizes and thickness, which is symmetrical around the centre of the metrics range. IPA has a higher average but also a narrower distribution, which can be seen by comparing the standard deviation of the points.

It is worth noting that the acetone-exfoliated nanosheets do not behave the same way as the usual LPE dispersions, due to the edge oxidation. However, the layer number and length estimation obtained from present metrics can yield not only the expected average but a better description of the distribution, as shown for the surfactant-exfoliated nanosheets (see Appendix C). Future work includes exfoliating MoS_2 in other solvents, surfactants, and polymer solutions to test the limits of the developed metrics.

6.5 Extension of Raman analysis to other layered materials

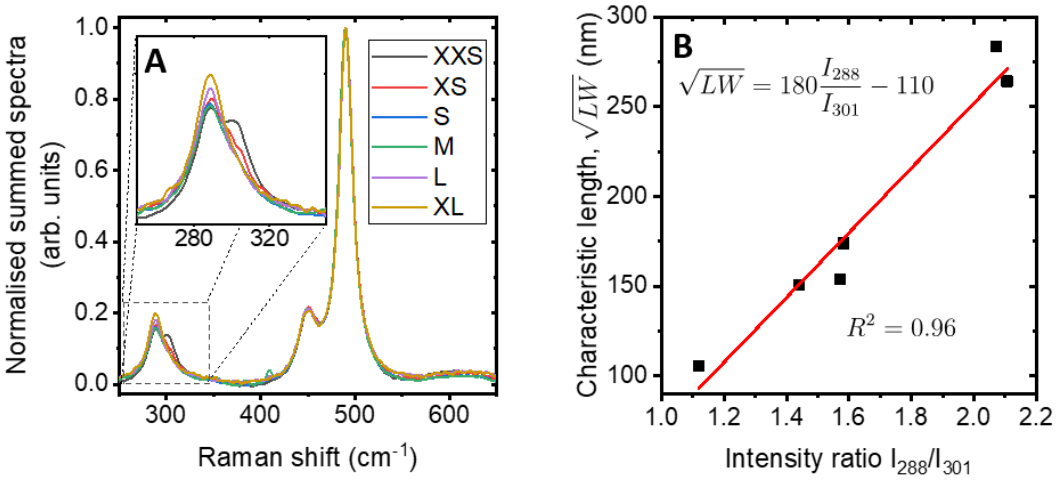

Figure 6.22: **A:** Normalised summed spectra for different nanocuboid samples. Inset highlights the change in the peak around 290 cm^{-1} with size. **B:** Plot of the characteristic length versus the intensity ratio I_{288}/I_{301}.

Glucose concentration sensing is used for diagnosis and monitoring of a various medical conditions, particularly diabetes [232]. While enzymatic glucose sensors are

capable of operating in physiological conditions, they suffer from being relatively expensive and also, with stability issues [232, 233]. This has led to research on non-enzymatic detectors [233], which are mainly comprised of metal oxides and associated compounds. A promising material is copper hydroxide as studied by Lynch *et al.* [234].

The same mapping analysis explained in Chapter 5 was performed on nanocuboid copper hydroxide. Figure 6.22A shows the normalised summed spectra of different fractions of an LCC series. Review of the literature reveals little analysis on $Cu(OH)_2$ and, due to the corrugated structure and different symmetry to other layered double-hydroxides, it is challenge to draw comparisons [235, 236]. However, they compare favourably to reference spectra from geological samples and the Raman of both bulk CuO and Cu_2O have modes at lower wavenumbers near the $290\,cm^{-1}$ peak, with the layered structure likely responsible for stiffening of the peak. Nanoparticulate copper oxides also experience a similar shift [237]. Further work is required to ascertain the surface functionality of the material. Close analysis of the peak (inset) shows that as the size fraction sample reduces, an additional mode becomes clear. This, in conjunction with AFM data, leads to a spectroscopic metric for $Cu(OH)_2$, as shown in figure 6.22B. The size characterisation developed here, is important since it was observed that as the size of the nanocuboids decreases, the electrochemical sensitivity of the material increases.

6.6 Conclusions

Robust spectroscopic metrics were developed for the layer number and length of MoS_2 nanosheets, which to this point have been absent in the literature. A new metric for MoS_2 layer number was developed based on an intensity ratio (I_{465}/I_{453}) of resonant Raman modes, avoiding any mischaracterisation caused by mode shifts resulting from external physical effects such as strain and doping. This metric can be applied to both LPE and ME nanosheets since the correlation between the intensity ratio and layer number is the same in both cases. A metric for LPE nanosheet length using the resonant laser was developed based on the intensity ratio between the two main Raman modes of MoS_2. The Raman mapping analysis combined with both metrics allows a quick and reliable characterisation

approximate of size and thickness distributions, paving the way for standardisation of novel nanomaterials and their diverse applications at different scales. This approach to the development of these metrics can be extended to the other TMDs, by virtue of their analogous crystal structures, and even to other layered materials such as the double-layered hydroxides, as demonstrated for copper hydroxide.

Chapter 7

Conclusions and future work

This research aimed to understand the liquid exfoliation of MoS_2 in a non-standard solvent. Common solvents used for exfoliation of layered nanomaterials yield highly-concentrated and well-exfoliated dispersions but have major drawbacks such as toxicity and high boiling point, which hinders further processing for some applications. The presence of residues, especially for NMP [48] and surfactant-exfoliated nanosheets, also affects characterisation. For example, it modifies thickness as measured by AFM [128, 116] and it affects photoluminescence spectrocopic measurements [50]. The main disadvantage, however, is related to applications such as for conductive networks where a further processing optimisation is needed [3].

The significantly increase in predicted concentration and stability of acetone-exfoliated MoS_2 nanosheets cannot be explained by applying the Hansen solubility parameter framework directly. This model predicts accurately the solvents that yield the best dispersions based on the interaction between the nanomaterial and the solvent. However, during ultrasonic exfoliation in acetone, a spontaneous edge functionalisation in the form of molybdenum oxides occurs and modifies this interaction. As a result of this change, the macroscopic properties are also improved, as shown by using MoS_2 as a catalyst for the hydrogen evolution reaction and comparing its performance with nanosheets exfoliated in an analogous solvent, IPA. Further spectroscopic characterisation confirmed the edges contained oxides. Therefore, the effects of the ultrasonication processing on the nanosheets was evaluated by a range of different characterisation techniques.

This specific system yields better spontaneous functionalisation when compared to the most common solvents reported in the literature. However, the same enhancement in macroscopic properties is likely to be general to other solvents used for exfoliation of TMDs. Since the functionalisation occurs at the edges of the nanosheets, smaller sheets should have a more prominent change, as seen in the literature previously [201]. Further study coupled with a LCC series to produce narrow size distributions could confirm this fact. Also, it is of interest to investigate if the same spontaneous edge-oxidation occurs under the same conditions for other similarly structured TMDs. Specifically, testing WS_2 and $MoSe_2$, for example, could give the insight whether the observed chemistry is general to all TMDs, or limited to materials containing either sulfur or molybdenum. Liu *et al.* [238] studied the oxidation of various TMD monolayers. They modelled different energy barriers for the formation of sulfur vacancies and also compared the changes to the band structure for pristine, defective and oxidised sheets. Even though the edge functionalisation studied in Chapter 4 is a different process, their work highlights the variation between TMDs, which leads to varied potential applications. For example, $MoTe_2$ and WTe_2 suffer the least oxidation under ambient conditions, making them more robust to influences in their electronic properties due to oxidation in devices.

The second aim was related to Raman spectroscopy, a non-destructive technique that yields detailed information about sample composition and functionalisation. It has the potential to provide macroscopic information due to phonon confinement effects and spectral changes due to intrinsic properties, in association with microscopic calibration. Motivated by the need for standardised and reliable characterisation of the nanosheets, a new appproach based on Raman microscopic mapping was investigated to determine whether it expands the amount of information obtained while characterising layer number and length.

Backes *et al.* [64] developed metrics for length and layer number of LPE graphene by examining spectral changes in comparison to quantitative microscopic analysis of nanosheets. In Chapter 5, these metrics were applied using a mapping approach in an attempt to evaluate the distributions of nanosheet size and thickness. The literature

metrics were developed by measuring single-point spectra at various points of a thick film. Hundreds of randomly-oriented nanosheets are analysed within the laser spot. The mapping process described here (Chapter 5) relies on decreasing the number of nanosheets per laser focal spot and, instead of averaging the results, applying the metrics on a resolution-limited pixel-wise fashion and binning the values. This was shown to reconstruct approximate distributions of size and thickness that differ from the true distribution but still yield enough information when considering practical factors. Importantly, distribution parameters such as the mean and standard deviation are accurately recovered, which has not been possible previously. The method works well even for broad distributions, as the results are not skewed towards thicker multilayer sheets, which is observed when there are several nanosheets under the laser spot due to varying contributions to the total Raman signal with layer number.

Applying the same mapping approach to MoS_2 proved to be challenging. The only existing current literature metric for layer number of MoS_2 relies on the peak separation between the main Raman modes, which are known to shift due to defects, strain, and doping. Also, a length metric was absent in the literature, motivating the development of more robust metrics. They were developed for both length and layer number, based on intensity ratios of Raman modes under resonant excitation. The use of intensity ratios of known modes avoids any mischaracterisation due to mode shifts. The layer number metric can be applied to LPE and also ME sheets. Even though the two techniques produce different nanosheets, the same correlation between layer number and intensity ratio was observed. The length metric for LPE nanosheets uses the main MoS_2 Raman modes. Combining the mapping approach with the newly-developed metrics allows a quick and reliable characterisation of the approximate macroscopic distributions. Due to its general nature, the extension of the framework to other layered materials is possible, as shown for copper hydroxide in Chapter 6. This work paves the way to a much-needed standardisation in characterisation of nanomaterials for both laboratory-based research and industrial-scale applications.

Re-evaluating the acetone-exfoliated nanosheets using the present metrics raised the question about their robustness against choice of solvent. Preliminary results show excellent agreement between solvent-exfoliated and the surfactant-exfoliated nanosheets used to calibrate the metrics and are presented in Chapter 6. Future work will compare the values obtained using the metrics with microscopic verification for exfoliation of MoS_2 using different types of surfactant, organic solvents, and polymer solutions to determine the extent to which these process modifications influence the metric analysis. Also, the influence of strain and doping on the 2LA(M) mode and the quantification of those effects on LPE samples is unclear. A comprehensive study of these extrinsic effects would be beneficial to fully characterise the samples and evaluate the limitations of both metrics more clearly. In addition to that, an extension to the metrics for LPE WS_2, still absent in the literature, should be possible due to the similar crystal structure to MoS_2 and the common availability of a resonant laser [239].

Bibliography

[1] Rou Jun Toh, Zdeněk Sofer, Jan Luxa, David Sedmidubský, and Martin Pumera. 3R phase of MoS $_2$ and WS $_2$ outperforms the corresponding 2H phase for hydrogen evolution. *Chemical Communications*, 53(21):3054–3057, February 2017. ix, 8, 9

[2] Zong-Yan Zhao and Qing-Lu Liu. Study of the layer-dependent properties of MoS $_2$ nanosheets with different crystal structures by DFT calculations. *Catalysis Science & Technology*, 8(7):1867–1879, February 2018. ix, 9, 11, 12, 13

[3] Matthew J. Large, Sean P. Ogilvie, Aline Amorim Graf, Peter J. Lynch, Marcus A. O'Mara, Thomas Waters, Izabela Jurewicz, Jonathan P. Salvage, and Alan B. Dalton. Large-Scale Surfactant Exfoliation of Graphene and Conductivity-Optimized Graphite Enabling Wireless Connectivity. *Advanced Materials Technologies*, page 2000284, May 2020. ix, 17, 22, 97

[4] A. Molina-Sánchez and L. Wirtz. Phonons in single-layer and few-layer MoS 2 and WS 2. *Physical Review B*, 84(15), October 2011. ix, 25, 26, 27

[5] Izhar Medalsy, Ulf Hensen, and Daniel J. Muller. Imaging and Quantifying Chemical and Physical Properties of Native Proteins at Molecular Resolution by Force-Volume AFM. *Angewandte Chemie International Edition*, 50(50):12103–12108, December 2011. x, 32

[6] Claudia Backes, Ronan J. Smith, Niall McEvoy, Nina C. Berner, David McCloskey, Hannah C. Nerl, Arlene O'Neill, Paul J. King, Tom Higgins, Damien Hanlon, Nils Scheuschner, Janina Maultzsch, Lothar Houben, Georg S. Duesberg, John F. Donegan, Valeria Nicolosi, and Jonathan N. Coleman. Edge and confinement effects

allow in situ measurement of size and thickness of liquid-exfoliated nanosheets. *Nature Communications*, 5(1):4576, December 2014. xi, 29, 31, 40, 41, 49, 50, 68, 75, 90, 92

[7] T. J. Wieting and J. L. Verble. Infrared and Raman Studies of Long-Wavelength Optical Phonons in Hexagonal Mo S 2. *Physical Review B*, 3(12):4286–4292, June 1971. xii, 4, 8, 68, 69, 136

[8] Bret C. Windom, W. G. Sawyer, and David W. Hahn. A Raman Spectroscopic Study of MoS2 and MoO3: Applications to Tribological Systems. *Tribology Letters*, 42(3):301–310, June 2011. xii, 44, 69

[9] Jae-Ung Lee, Jaesung Park, Young-Woo Son, and Hyeonsik Cheong. Anomalous excitonic resonance Raman effects in few-layered MoS $_2$. *Nanoscale*, 7(7):3229–3236, January 2015. xii, 43, 68, 70

[10] Sandro Mignuzzi, Andrew J. Pollard, Nicola Bonini, Barry Brennan, Ian S. Gilmore, Marcos A. Pimenta, David Richards, and Debdulal Roy. Effect of disorder on Raman scattering of single-layer Mo S 2. *Physical Review B*, 91(19):1954111–7, May 2015. xii, 44, 70, 71

[11] C. Rice, R. J. Young, R. Zan, U. Bangert, D. Wolverson, T. Georgiou, R. Jalil, and K. S. Novoselov. Raman-scattering measurements and first-principles calculations of strain-induced phonon shifts in monolayer MoS 2. *Physical Review B*, 87(8), February 2013. xii, 71, 72

[12] Biswanath Chakraborty, Achintya Bera, D. V. S. Muthu, Somnath Bhowmick, U. V. Waghmare, and A. K. Sood. Symmetry-dependent phonon renormalization in monolayer MoS 2 transistor. *Physical Review B*, 85(16), April 2012. xii, 72, 93

[13] Bharat Bhushan, editor. *Springer Handbook of Nanotechnology*. Springer Handbooks. Springer, Berlin, 3., rev. and extended ed edition, April 2010. 1

[14] Mihail C. Roco. The long view of nanotechnology development: The National Nanotechnology Initiative at 10 years. *Journal of Nanoparticle Research*, 13(2):427–445, February 2011. 1

[15] Alexander A. Balandin, Suchismita Ghosh, Wenzhong Bao, Irene Calizo, Desalegne Teweldebrhan, Feng Miao, and Chun Ning Lau. Superior Thermal Conductivity of Single-Layer Graphene. *Nano Letters*, 8(3):902–907, March 2008. 1

[16] C. Lee, X. Wei, J. W. Kysar, and J. Hone. Measurement of the Elastic Properties and Intrinsic Strength of Monolayer Graphene. *Science*, 321(5887):385–388, July 2008. 1

[17] K. S. Novoselov. Electric Field Effect in Atomically Thin Carbon Films. *Science*, 306(5696):666–669, October 2004. 1, 4, 7, 13

[18] J. Scott Bunch, Scott S. Verbridge, Jonathan S. Alden, Arend M. van der Zande, Jeevak M. Parpia, Harold G. Craighead, and Paul L. McEuen. Impermeable Atomic Membranes from Graphene Sheets. *Nano Letters*, 8(8):2458–2462, August 2008. 1

[19] R. R. Nair, H. A. Wu, P. N. Jayaram, I. V. Grigorieva, and A. K. Geim. Unimpeded Permeation of Water Through Helium-Leak-Tight Graphene-Based Membranes. *Science*, 335(6067):442–444, January 2012. 1

[20] J.A. Wilson and A.D. Yoffe. The transition metal dichalcogenides discussion and interpretation of the observed optical, electrical and structural properties. *Advances in Physics*, 18(73):193–335, May 1969. 1, 7

[21] Qing Hua Wang, Kourosh Kalantar-Zadeh, Andras Kis, Jonathan N. Coleman, and Michael S. Strano. Electronics and optoelectronics of two-dimensional transition metal dichalcogenides. *Nature Nanotechnology*, 7(11):699–712, November 2012. 1

[22] Rudren Ganatra and Qing Zhang. Few-Layer MoS_2: A Promising Layered Semiconductor. *ACS Nano*, 8(5):4074–4099, May 2014. 1, 26

[23] A.D. Yoffe. Low-dimensional systems: Quantum size effects and electronic properties of semiconductor microcrystallites (zero-dimensional systems) and some quasi-two-dimensional systems. *Advances in Physics*, 42(2):173–262, April 1993. 1

[24] Andrea Splendiani, Liang Sun, Yuanbo Zhang, Tianshu Li, Jonghwan Kim, Chi-Yung Chim, Giulia Galli, and Feng Wang. Emerging Photoluminescence in Monolayer MoS $_2$. *Nano Letters*, 10(4):1271–1275, April 2010. 1, 7

[25] Humberto R. Gutiérrez, Nestor Perea-López, Ana Laura Elías, Ayse Berkdemir, Bei Wang, Ruitao Lv, Florentino López-Urías, Vincent H. Crespi, Humberto Terrones, and Mauricio Terrones. Extraordinary Room-Temperature Photoluminescence in Triangular WS $_2$ Monolayers. *Nano Letters*, 13(8):3447–3454, August 2013. 1, 7

[26] Claudia Ruppert, Ozgur Burak Aslan, and Tony F. Heinz. Optical Properties and Band Gap of Single- and Few-Layer MoTe $_2$ Crystals. *Nano Letters*, 14(11):6231–6236, November 2014. 1, 7

[27] T. F. Jaramillo, K. P. Jorgensen, J. Bonde, J. H. Nielsen, S. Horch, and I. Chorkendorff. Identification of Active Edge Sites for Electrochemical H2 Evolution from MoS2 Nanocatalysts. *Science*, 317(5834):100–102, July 2007. 1, 7, 54

[28] Hannu-Pekka Komsa, Jani Kotakoski, Simon Kurasch, Ossi Lehtinen, Ute Kaiser, and Arkady V. Krasheninnikov. Two-Dimensional Transition Metal Dichalcogenides under Electron Irradiation: Defect Production and Doping. *Physical Review Letters*, 109(3), July 2012. 1, 7

[29] Nicolas Onofrio, David Guzman, and Alejandro Strachan. Novel doping alternatives for single-layer transition metal dichalcogenides. *Journal of Applied Physics*, 122(18):185102, November 2017. 1, 7

[30] Wenwu Shi, Kaimin Fan, and Zhiguo Wang. Catalytic activity for the hydrogen evolution reaction of edges in Janus monolayer MoXY (X/Y = S, Se, and Te). *Physical Chemistry Chemical Physics*, 20(46):29423–29429, October 2018. 1, 7

[31] Rusen Yan, Jeffrey R. Simpson, Simone Bertolazzi, Jacopo Brivio, Michael Watson, Xufei Wu, Andras Kis, Tengfei Luo, Angela R. Hight Walker, and Huili Grace Xing. Thermal Conductivity of Monolayer Molybdenum Disulfide Obtained from Temperature-Dependent Raman Spectroscopy. *ACS Nano*, 8(1):986–993, January 2014. 1

[32] Xiangjun Liu and Yong-Wei Zhang. Thermal properties of transition-metal dichalcogenide. *Chinese Physics B*, 27(3):034402, March 2018. 1

[33] Mojtaba Ahmadi, Omid Zabihi, Seokwoo Jeon, Mitra Yoonessi, Aravind Dasari, Seeram Ramakrishna, and Minoo Naebe. 2D transition metal dichalcogenide nanomaterials: Advances, opportunities, and challenges in multi-functional polymer nanocomposites. *Journal of Materials Chemistry A*, 8(3):845–883, October 2019. 1

[34] L. F. Mattheiss. Band Structures of Transition-Metal-Dichalcogenide Layer Compounds. *Physical Review B*, 8(8):3719–3740, October 1973. 1

[35] Manish Chhowalla, Hyeon Suk Shin, Goki Eda, Lain-Jong Li, Kian Ping Loh, and Hua Zhang. The chemistry of two-dimensional layered transition metal dichalcogenide nanosheets. *Nature Chemistry*, 5(4):263–275, April 2013. 1

[36] European Commission. *Communication from the Commission: Towards a European Strategy for Nanotechnology.* Publications Office, Luxembourg, 2004. 2

[37] European Commission and Directorate General for Research. *Nanosciences and Nanotechnologies: An Action Plan for Europe 2005-2009.* Office for Official Publications of the European Communities, Luxembourg, 2005. 2

[38] European Commission and Directorate General for Research. *Commission Recommendation on a Code of Conduct for Responsible Nanosciences and Nano-*

technologies Research & Council Conclusions on Responsible Nanosciences and Nanotechnologies Research. Publications Office, Luxembourg, 2009. 2

[39] European Union and Directorate-General for Research and Innovation. *Nanotechnology: The Invisible Giant Tackling Europe's Future Challenge*. Publications Office of the European Union, Luxembourg, 2013. 2

[40] FAO and Weltgesundheitsorganisation, editors. *State of the Art on the Initiatives and Activities Relevant to Risk Assessment and Risk Management of Nanotechnologies in the Food and Agriculture Sectors*. FAO WHO Technical Paper. FAO, Rome, 2013. 2

[41] Eun-Jung Park, Eunjoo Bae, Jongheop Yi, Younghun Kim, Kyunghee Choi, Sang Hee Lee, Junheon Yoon, Byung Chun Lee, and Kwangsik Park. Repeated-dose toxicity and inflammatory responses in mice by oral administration of silver nanoparticles. *Environmental Toxicology and Pharmacology*, 30(2):162–168, September 2010. 2

[42] Yenny Hernandez, Valeria Nicolosi, Mustafa Lotya, Fiona M. Blighe, Zhenyu Sun, Sukanta De, I. T. McGovern, Brendan Holland, Michele Byrne, Yurii K. Gun'Ko, John J. Boland, Peter Niraj, Georg Duesberg, Satheesh Krishnamurthy, Robbie Goodhue, John Hutchison, Vittorio Scardaci, Andrea C. Ferrari, and Jonathan N. Coleman. High-yield production of graphene by liquid-phase exfoliation of graphite. *Nature Nanotechnology*, 3(9):563–568, September 2008. 3, 14, 58

[43] J. N. Coleman, M. Lotya, A. O'Neill, S. D. Bergin, P. J. King, U. Khan, K. Young, A. Gaucher, S. De, R. J. Smith, I. V. Shvets, S. K. Arora, G. Stanton, H.-Y. Kim, K. Lee, G. T. Kim, G. S. Duesberg, T. Hallam, J. J. Boland, J. J. Wang, J. F. Donegan, J. C. Grunlan, G. Moriarty, A. Shmeliov, R. J. Nicholls, J. M. Perkins, E. M. Grieveson, K. Theuwissen, D. W. McComb, P. D. Nellist, and V. Nicolosi. Two-Dimensional Nanosheets Produced by Liquid Exfoliation of Layered Materials. *Science*, 331(6017):568–571, February 2011. 3, 15, 39, 40, 51, 58

[44] Graeme Cunningham, Mustafa Lotya, Clotilde S. Cucinotta, Stefano Sanvito, Shane D. Bergin, Robert Menzel, Milo S. P. Shaffer, and Jonathan N. Coleman. Solvent Exfoliation of Transition Metal Dichalcogenides: Dispersibility of Exfoliated Nanosheets Varies Only Weakly between Compounds. *ACS Nano*, 6(4):3468–3480, April 2012. 3, 40, 51, 52

[45] Arlene O'Neill, Umar Khan, and Jonathan N Coleman. Preparation of High Concentration Dispersions of Exfoliated MoS $_2$ with Increased Flake Size. *Chemistry of Materials*, 24(12):2414–2421, June 2012. 3, 22, 39, 58

[46] Jonathan N Coleman. Liquid Exfoliation of Defect-Free Graphene. *Accounts of Chemical Research*, 46(1):14–22, January 2013. 3, 15, 39, 58

[47] Claudia Backes, Beata M. Szydłowska, Andrew Harvey, Shengjun Yuan, Victor Vega-Mayoral, Ben R. Davies, Pei-liang Zhao, Damien Hanlon, Elton J. G. Santos, Mikhail I. Katsnelson, Werner J. Blau, Christoph Gadermaier, and Jonathan N. Coleman. Production of Highly Monolayer Enriched Dispersions of Liquid-Exfoliated Nanosheets by Liquid Cascade Centrifugation. *ACS Nano*, 10(1):1589–1601, January 2016. 3, 22, 41, 78

[48] Hin Chun Yau, Mustafa K. Bayazit, Joachim H. G. Steinke, and Milo S. P. Shaffer. Sonochemical degradation of N-methylpyrrolidone and its influence on single walled carbon nanotube dispersion. *Chemical Communications*, 51(93):16621–16624, September 2015. 3, 51, 97

[49] Amit Gupta, Vaishali Arunachalam, and Sukumaran Vasudevan. Liquid-Phase Exfoliation of MoS $_2$ Nanosheets: The Critical Role of Trace Water. *The Journal of Physical Chemistry Letters*, 7(23):4884–4890, December 2016. 3

[50] Sean P. Ogilvie, Matthew J. Large, Giuseppe Fratta, Manuela Meloni, Ruben Canton-Vitoria, Nikos Tagmatarchis, Florian Massuyeau, Christopher P. Ewels, Alice A. K. King, and Alan B. Dalton. Considerations for spectroscopy of liquid-exfoliated

2D materials: Emerging photoluminescence of N-methyl-2-pyrrolidone. *Scientific Reports*, 7(1):16706, December 2017. 3, 51, 97

[51] Ali Jawaid, Dhriti Nepal, Kyoungweon Park, Michael Jespersen, Anthony Qualley, Peter Mirau, Lawrence F. Drummy, and Richard A. Vaia. Mechanism for Liquid Phase Exfoliation of MoS $_2$. *Chemistry of Materials*, 28(1):337–348, January 2016. 3, 51

[52] Amit Gupta and Sukumaran Vasudevan. Understanding Surfactant Stabilization of MoS $_2$ Nanosheets in Aqueous Dispersions from Zeta Potential Measurements and Molecular Dynamics Simulations. *The Journal of Physical Chemistry C*, 122(33):19243–19250, August 2018. 3, 36, 41

[53] Bengt Åkesson. *N-Methyl-2-Pyrrolidone*. Number 35 in Concise International Chemical Assessment Document. World Health Organization, Geneva, 2001. 3

[54] Han Ma and Zhigang Shen. Exfoliation of graphene nanosheets in aqueous media. *Ceramics International*, June 2020. 3

[55] Viviane Forsberg, Renyun Zhang, Joakim Bäckström, Christina Dahlström, Britta Andres, Magnus Norgren, Mattias Andersson, Magnus Hummelgård, and Håkan Olin. Exfoliated MoS2 in Water without Additives. *PLOS ONE*, 11(4):e0154522, April 2016. 3, 39

[56] Arlene O'Neill, Umar Khan, Peter N. Nirmalraj, John Boland, and Jonathan N Coleman. Graphene Dispersion and Exfoliation in Low Boiling Point Solvents. *The Journal of Physical Chemistry C*, 115(13):5422–5428, April 2011. 3, 39

[57] Udayabagya Halim, Chu Ran Zheng, Yu Chen, Zhaoyang Lin, Shan Jiang, Rui Cheng, Yu Huang, and Xiangfeng Duan. A rational design of cosolvent exfoliation of layered materials by directly probing liquid–solid interaction. *Nature Communications*, 4(1), December 2013. 3

[58] Xing Juan Chua and Martin Pumera. The effect of varying solvents for MoS $_2$ treatment on its catalytic efficiencies for HER and ORR. *Physical Chemistry Chemical Physics*, 19(9):6610–6619, January 2017. 3

[59] Kenneth Lobo, Shivam Trivedi, and H S S Ramakrishna Matte. Highly Concentrated and Stabilizer-free Transition Metal Dichalcogenide Dispersions in Low Boiling Point Solvent for Flexible Electronics. *Nanoscale*, 11:10746–10755, April 2019. 3, 53

[60] Technical commitee ISO/TC 229. ISO/TS 80004-13:2017, Nanotechnologies - Vocabulary - Part 13: Graphene and related two dimensional (2D) materials. Technical report, International Organization for Standardization, Geneva, 2017. 3, 58

[61] Andrew J. Pollard, Keith R. Paton, Charles A. Clifford, and Elizabeth Legge. *NPL Good Practice Guide 145*. National Physical Laboratory, Teddington, 2007. 3, 58

[62] F. Tuinstra and J. L. Koenig. Raman Spectrum of Graphite. *The Journal of Chemical Physics*, 53(3):1126–1130, August 1970. 4

[63] A. C. Ferrari, J. C. Meyer, V. Scardaci, C. Casiraghi, M. Lazzeri, F. Mauri, S. Piscanec, D. Jiang, K. S. Novoselov, S. Roth, and A. K. Geim. Raman Spectrum of Graphene and Graphene Layers. *Physical Review Letters*, 97(18), October 2006. 4, 59

[64] Claudia Backes, Keith R. Paton, Damien Hanlon, Shengjun Yuan, Mikhail I. Katsnelson, James Houston, Ronan J. Smith, David McCloskey, John F. Donegan, and Jonathan N. Coleman. Spectroscopic metrics allow in situ measurement of mean size and thickness of liquid-exfoliated few-layer graphene nanosheets. *Nanoscale*, 8(7):4311–4323, January 2016. 4, 29, 59, 75, 83, 87, 90, 98

[65] J. L. Verble and T. J. Wieting. Lattice Mode Degeneracy in Mo S 2 and Other Layer Compounds. *Physical Review Letters*, 25(6):362–365, August 1970. 4, 68, 69

[66] Changgu Lee, Hugen Yan, Louis E. Brus, Tony F. Heinz, James Hone, and Sunmin Ryu. Anomalous Lattice Vibrations of Single- and Few-Layer MoS $_2$. *ACS Nano*, 4(5):2695–2700, May 2010. 4, 92

[67] Marcos A. Pimenta, Elena del Corro, Bruno R. Carvalho, Cristiano Fantini, and Leandro M. Malard. Comparative Study of Raman Spectroscopy in Graphene and MoS $_2$ -type Transition Metal Dichalcogenides. *Accounts of Chemical Research*, 48(1):41–47, January 2015. 4, 27, 68, 71, 83

[68] Richard Rennie, editor. *A Dictionary of Physics*. Oxford Quick Reference. Oxford University Press, Oxford, seventh edition edition, 2015. 6, 9, 10, 13, 23, 26, 27, 29

[69] Zahra Rafiei-Sarmazdeh, Seyed Morteza Zahedi-Dizaji, and Aniseh Kafi Kang. Two-Dimensional Nanomaterials. In Sadia Ameen, M. Shaheer Akhtar, and Hyung-Shik Shin, editors, *Nanostructures*. IntechOpen, February 2020. 6

[70] H. W. Kroto, J. R. Heath, S. C. O'Brien, R. F. Curl, and R. E. Smalley. C60: Buckminsterfullerene. *Nature*, 318(6042):162–163, November 1985. 6

[71] Sumio Iijima. Helical microtubules of graphitic carbon. *Nature*, 354(6348):56–58, November 1991. 6

[72] Xuewen Wang, Yinghui Sun, and Kai Liu. Chemical and structural stability of 2D layered materials. *2D Materials*, 6(4):042001, July 2019. 7

[73] Morasae Samadi, Navid Sarikhani, Mohammad Zirak, Hua Zhang, Hao-Li Zhang, and Alireza Z. Moshfegh. Group 6 transition metal dichalcogenide nanomaterials: Synthesis, applications and future perspectives. *Nanoscale Horizons*, 3(2):90–204, December 2017. 7

[74] W.O. Winer. Molybdenum disulfide as a lubricant: A review of the fundamental knowledge. *Wear*, 10(6):422–452, November 1967. 7

[75] E. Furimsky. Role of MoS $_2$ and WS $_2$ in Hydrodesulfuritation. *Catalysis Reviews*, 22(3):371–400, January 1980. 7

[76] M.Stanley Whittingham. Chemistry of intercalation compounds: Metal guests in chalcogenide hosts. *Progress in Solid State Chemistry*, 12(1):41–99, January 1978. 7

[77] Per Joensen, R.F. Frindt, and S.Roy Morrison. Single-layer MoS2. *Materials Research Bulletin*, 21(4):457–461, April 1986. 7

[78] Kin Fai Mak, Changgu Lee, James Hone, Jie Shan, and Tony F. Heinz. Atomically Thin MoS 2 : A New Direct-Gap Semiconductor. *Physical Review Letters*, 105(13), September 2010. 7, 12

[79] B. Radisavljevic, A. Radenovic, J. Brivio, V. Giacometti, and A. Kis. Single-layer MoS2 transistors. *Nature Nanotechnology*, 6(3):147–150, March 2011. 8

[80] Yifu Yu, Gwang-Hyeon Nam, Qiyuan He, Xue-Jun Wu, Kang Zhang, Zhenzhong Yang, Junze Chen, Qinglang Ma, Meiting Zhao, Zhengqing Liu, Fei-Rong Ran, Xingzhi Wang, Hai Li, Xiao Huang, Bing Li, Qihua Xiong, Qing Zhang, Zheng Liu, Lin Gu, Yonghua Du, Wei Huang, and Hua Zhang. High phase-purity 1T′-MoS2- and 1T′-MoSe2-layered crystals. *Nature Chemistry*, 10(6):638–643, June 2018. 8

[81] Weijie Zhao, Zohreh Ghorannevis, Kiran Kumar Amara, Jing Ren Pang, Minglin Toh, Xin Zhang, Christian Kloc, Ping Heng Tan, and Goki Eda. Lattice dynamics in mono- and few-layer sheets of WS2 and WSe2. *Nanoscale*, 5(20):9677, August 2013. 8

[82] Alex Yong Sheng Eng, Adriano Ambrosi, Zdeněk Sofer, Petr Šimek, and Martin Pumera. Electrochemistry of Transition Metal Dichalcogenides: Strong Dependence on the Metal-to-Chalcogen Composition and Exfoliation Method. *ACS Nano*, 8(12):12185–12198, December 2014. 8, 85

[83] Judith W. Frondel and Frans E. Wickman. Molybdenite polytypes in theory and occurrence. II. Some naturally-occurring polytypes of molybdenite. *American Mineralogist: Journal of Earth and Planetary Materials*, 55(11-12):1857–1875, December 1970. 8

[84] M. A. Py and R. R. Haering. Structural destabilization induced by lithium intercalation in MoS $_2$ and related compounds. *Canadian Journal of Physics*, 61(1):76–84, January 1983. 8

[85] Yung-Chang Lin, Hideaki Nakajima, Chung-Wei Tseng, Shisheng Li, Zheng Liu, Toshiya Okazaki, Po-Wen Chiu, and Kazu Suenaga. Does the metallic 1T phase WS2 really exist? *arXiv:1907.11398 [cond-mat]*, July 2019. 9

[86] J. Michael Hollas. *Modern Spectroscopy*. J. Wiley, Chichester ; Hoboken, NJ, 4th ed edition, November 2003. 10, 23, 25, 26

[87] Adrianus J. Dekker. *Solid State Physics*. Macmillan, London, first edition, 1970. 10

[88] Leonid V. Azároff and James J. Brophy. *Electronic Processes in Materials*. McGraw-Hill, New York, 1963. 10

[89] Charles Kittel. *Introduction to Solid State Physics*. Wiley, Hoboken, NJ, 8th ed edition, 2005. 10, 29

[90] Manijeh Razeghi. *Fundamentals of Solid State Engineering*. Springer, Cham, fourth edition edition, 2019. 10

[91] A. Kuc, N. Zibouche, and T. Heine. Influence of quantum confinement on the electronic structure of the transition metal sulfide T S 2. *Physical Review B*, 83(24), June 2011. 12

[92] S.S. Coutinho, M.S. Tavares, C.A. Barboza, N.F. Frazão, E. Moreira, and David L. Azevedo. 3R and 2H polytypes of MoS2: DFT and DFPT calculations of structural, optoelectronic, vibrational and thermodynamic properties. *Journal of Physics and Chemistry of Solids*, 111:25–33, December 2017. 12

[93] S. Anghel, Yu Chumakov, V. Kravtsov, A. Mitioglu, P. Plochocka, K. Sushkevich, G. Volodina, A. Colev, and L. Kulyuk. Identification of 2H and 3R polytypes of MoS2 layered crystals using photoluminescence spectroscopy. *arXiv:1411.3850 [cond-mat]*, November 2014. 12

[94] Kristin Persson. Materials Data on MoS2 (SG:160) by Materials Project, 2014. 12

[95] Basant A. Ali, Asmaa M. A. Omar, Ahmed S. G. Khalil, and Nageh K. Allam. Untapped Potential of Polymorph MoS $_2$: Tuned Cationic Intercalation for High-Performance Symmetric Supercapacitors. *ACS Applied Materials & Interfaces*, 11(37):33955–33965, September 2019. 13

[96] Jia Shi, Peng Yu, Fucai Liu, Peng He, Rui Wang, Liang Qin, Junbo Zhou, Xin Li, Jiadong Zhou, Xinyu Sui, Shuai Zhang, Yanfeng Zhang, Qing Zhang, Tze Chien Sum, Xiaohui Qiu, Zheng Liu, and Xinfeng Liu. 3R MoS $_2$ with Broken Inversion Symmetry: A Promising Ultrathin Nonlinear Optical Device. *Advanced Materials*, 29(30):1701486, August 2017. 13

[97] Chenzhang Zhou and Kofi Adu. Why Phonon Behaviors in Transition Metal Dichalcogenides Matter. *MRS Advances*, 4(10):629–634, February 2019. 13

[98] Hari Singh Nalwa, editor. *Encyclopedia of Nanoscience and Nanotechnology. v. 1-10*. American Scientific Publishers, Stevenson Ranch, Calif, 2004. 13, 25

[99] Kristen Kaasbjerg, Kristian S. Thygesen, and Karsten W. Jacobsen. Phonon-limited mobility in n -type single-layer MoS 2 from first principles. *Physical Review B*, 85(11), March 2012. 13

[100] Yanyan Xu, Huizhe Cao, Yanqin Xue, Biao Li, and Weihua Cai. Liquid-Phase Exfoliation of Graphene: An Overview on Exfoliation Media, Techniques, and Challenges. *Nanomaterials*, 8(11):942, November 2018. 13

[101] K. S. Novoselov, D. Jiang, F. Schedin, T. J. Booth, V. V. Khotkevich, S. V. Morozov, and A. K. Geim. Two-dimensional atomic crystals. *Proceedings of the National Academy of Sciences*, 102(30):10451–10453, July 2005. 13

[102] Hai Li, Jumiati Wu, Zongyou Yin, and Hua Zhang. Preparation and Applications of Mechanically Exfoliated Single-Layer and Multilayer MoS $_2$ and WSe $_2$ Nanosheets. *Accounts of Chemical Research*, 47(4):1067–1075, April 2014. 14

[103] Min Yi and Zhigang Shen. A review on mechanical exfoliation for the scalable production of graphene. *Journal of Materials Chemistry A*, 3(22):11700–11715, March 2015. 14

[104] A. K. Geim and K. S. Novoselov. The rise of graphene. *Nature Materials*, 6(3):183–191, March 2007. 14

[105] Achilleas Sesis, Mark Hodnett, Gianluca Memoli, Andrew J. Wain, Izabela Jurewicz, Alan B. Dalton, J. David Carey, and Gareth Hinds. Influence of Acoustic Cavitation on the Controlled Ultrasonic Dispersion of Carbon Nanotubes. *The Journal of Physical Chemistry B*, 117(48):15141–15150, December 2013. 14

[106] Claudia Backes, Davide Campi, Beata M. Szydlowska, Kevin Synnatschke, Ezgi Ojala, Farnia Rashvand, Andrew Harvey, Aideen Griffin, Zdenek Sofer, Nicola Marzari, Jonathan N. Coleman, and David D. O'Regan. Equipartition of Energy Defines the Size–Thickness Relationship in Liquid-Exfoliated Nanosheets. *ACS Nano*, 13(6):7050–7061, June 2019. 14, 22, 87, 91

[107] Goki Eda, Giovanni Fanchini, and Manish Chhowalla. Large-area ultrathin films of reduced graphene oxide as a transparent and flexible electronic material. *Nature Nanotechnology*, 3(5):270–274, May 2008. 14

[108] Sasha Stankovich, Dmitriy A. Dikin, Geoffrey H. B. Dommett, Kevin M. Kohlhaas, Eric J. Zimney, Eric A. Stach, Richard D. Piner, SonBinh T. Nguyen, and Rodney S. Ruoff. Graphene-based composite materials. *Nature*, 442(7100):282–286, July 2006. 14

[109] Sasha Stankovich, Dmitriy A. Dikin, Richard D. Piner, Kevin A. Kohlhaas, Alfred Kleinhammes, Yuanyuan Jia, Yue Wu, SonBinh T. Nguyen, and Rodney S. Ruoff. Synthesis of graphene-based nanosheets via chemical reduction of exfoliated graphite oxide. *Carbon*, 45(7):1558–1565, June 2007. 14

[110] Sandip Niyogi, Elena Bekyarova, Mikhail E. Itkis, Jared L. McWilliams, Mark A. Hamon, and Robert C. Haddon. Solution Properties of Graphite and Graphene. *Journal of the American Chemical Society*, 128(24):7720–7721, June 2006. 14

[111] Brian J. Landi, Herbert J. Ruf, James J. Worman, and Ryne P. Raffaelle. Effects of Alkyl Amide Solvents on the Dispersion of Single-Wall Carbon Nanotubes. *The Journal of Physical Chemistry B*, 108(44):17089–17095, November 2004. 14

[112] Tawfique Hasan, Vittorio Scardaci, PingHeng Tan, Aleksey G. Rozhin, William I. Milne, and Andrea C. Ferrari. Stabilization and "Debundling" of Single-Wall Carbon Nanotube Dispersions in *N* -Methyl-2-pyrrolidone (NMP) by Polyvinylpyrrolidone (PVP). *The Journal of Physical Chemistry C*, 111(34):12594–12602, August 2007. 14

[113] Héctor A. Becerril, Jie Mao, Zunfeng Liu, Randall M. Stoltenberg, Zhenan Bao, and Yongsheng Chen. Evaluation of Solution-Processed Reduced Graphene Oxide Films as Transparent Conductors. *ACS Nano*, 2(3):463–470, March 2008. 14

[114] G.S Duesberg, W.J Blau, H.J Byrne, J Muster, M Burghard, and S Roth. Experimental observation of individual single-wall nanotube species by Raman microscopy. *Chemical Physics Letters*, 310(1-2):8–14, August 1999. 14

[115] Peter Blake, Paul D. Brimicombe, Rahul R. Nair, Tim J. Booth, Da Jiang, Fred Schedin, Leonid A. Ponomarenko, Sergey V. Morozov, Helen F. Gleeson, Ernie W. Hill, Andre K. Geim, and Kostya S. Novoselov. Graphene-Based Liquid Crystal Device. *Nano Letters*, 8(6):1704–1708, June 2008. 14

[116] Mustafa Lotya, Yenny Hernandez, Paul J. King, Ronan J. Smith, Valeria Nicolosi, Lisa S. Karlsson, Fiona M. Blighe, Sukanta De, Zhiming Wang, I. T. McGovern, Georg S. Duesberg, and Jonathan N. Coleman. Liquid Phase Production of Graphene by Exfoliation of Graphite in Surfactant/Water Solutions. *Journal of the American Chemical Society*, 131(10):3611–3620, March 2009. 14, 39, 41, 58, 66, 97

[117] Victor Vega-Mayoral, Claudia Backes, Damien Hanlon, Umar Khan, Zahra Gholamvand, Maria O'Brien, Georg S. Duesberg, Christoph Gadermaier, and Jonathan N. Coleman. Photoluminescence from Liquid-Exfoliated WS_2 Monomers in Poly(Vinyl Alcohol) Polymer Composites. *Advanced Functional Materials*, 26(7):1028–1039, February 2016. 14

[118] J. Marguerite Hughes, Damian Aherne, and Jonathan N. Coleman. Generalizing solubility parameter theory to apply to one- and two-dimensional solutes and to incorporate dipolar interactions. *Journal of Applied Polymer Science*, 127(6):4483–4491, March 2013. 15

[119] Matthew J. Large, Sean P. Ogilvie, Alice A. K. King, and Alan B. Dalton. Understanding Solvent Spreading for Langmuir Deposition of Nanomaterial Films: A Hansen Solubility Parameter Approach. *Langmuir*, 33(51):14766–14771, December 2017. 15

[120] Fred W. Billmeyer. *Textbook of Polymer Science*. Wiley-Interscience, New York, 2d ed edition, 1971. 15

[121] Charles M. Hansen. *The Three Dimensional Solubility Parameter and Solvent Diffusion Coefficient: Their Importance in Surface Coating Formulation*. PhD thesis, August 1967. 15

[122] Charles M. Hansen. *Hansen Solubility Parameters: A User's Handbook*. CRC Press, Boca Raton, 2nd ed edition, 2007. 16, 40, 52, 53

[123] Aideen Griffin, Katharina Nisi, Joshua Pepper, Andrew Harvey, Beata M. Szydlowska, Jonathan N Coleman, and Claudia Backes. The Effect of Surfactant Choice and Concentration on the Dimensions and Yield of Liquid Phase Exfoliated Nanosheets. *Chemistry of Materials*, March 2020. 16

[124] Steffen Ott, Nadja Wolff, Farnia Rashvand, Vaishnavi J. Rao, Jana Zaumseil, and Claudia Backes. Impact of the MoS_2 Starting Material on the Dispersion Quality

and Quantity after Liquid Phase Exfoliation. *Chemistry of Materials*, 31(20):8424–8431, October 2019. 16

[125] Claudia Backes, Thomas M. Higgins, Adam Kelly, Conor Boland, Andrew Harvey, Damien Hanlon, and Jonathan N. Coleman. Guidelines for Exfoliation, Characterization and Processing of Layered Materials Produced by Liquid Exfoliation. *Chemistry of Materials*, 29(1):243–255, January 2017. 16, 31, 58, 75

[126] Zheling Li, Robert J. Young, Claudia Backes, Wen Zhao, Xun Zhang, Alexander Zhukov, Evan Tillotson, Aidan P. Conlan, Feng Ding, Sarah J. Haigh, Kostya S. Novoselov, and Jonathan N. Coleman. Mechanisms of Liquid-Phase Exfoliation for the Production of Graphene. *ACS Nano*, July 2020. 16

[127] Hengcong Tao, Yuqin Zhang, Yunnan Gao, Zhenyu Sun, Chao Yan, and John Texter. Scalable exfoliation and dispersion of two-dimensional materials – an update. *Physical Chemistry Chemical Physics*, 19(2):921–960, November 2016. 16, 18

[128] Keith R. Paton, Eswaraiah Varrla, Claudia Backes, Ronan J. Smith, Umar Khan, Arlene O'Neill, Conor Boland, Mustafa Lotya, Oana M. Istrate, Paul King, Tom Higgins, Sebastian Barwich, Peter May, Pawel Puczkarski, Iftikhar Ahmed, Matthias Moebius, Henrik Pettersson, Edmund Long, João Coelho, Sean E. O'Brien, Eva K. McGuire, Beatriz Mendoza Sanchez, Georg S. Duesberg, Niall McEvoy, Timothy J. Pennycook, Clive Downing, Alison Crossley, Valeria Nicolosi, and Jonathan N. Coleman. Scalable production of large quantities of defect-free few-layer graphene by shear exfoliation in liquids. *Nature Materials*, 13(6):624–630, June 2014. 17, 41, 58, 66, 97

[129] Sonia Biccai, Sebastian Barwich, Daniel Boland, Andrey Harvey, Damien Hanlon, Niall McEvoy, and Jonathan N Coleman. Exfoliation of 2D materials by high shear mixing. *2D Materials*, 6(1):015008, October 2018. 17

[130] A. E. Del Rio Castillo, V. Pellegrini, A. Ansaldo, F. Ricciardella, H. Sun, L. Marasco, J. Buha, Z. Dang, L. Gagliani, E. Lago, N. Curreli, S. Gentiluomo, F. Palazon, M. Prato, R. Oropesa-Nuñez, P. S. Toth, E. Mantero, M. Crugliano, A. Gamucci, A. Tomadin, M. Polini, and F. Bonaccorso. High-yield production of 2D crystals by wet-jet milling. *Materials Horizons*, 5(5):890–904, July 2018. 17

[131] Sebastiano Bellani, Elisa Petroni, Antonio Esau Del Rio Castillo, Nicola Curreli, Beatriz Martín-García, Reinier Oropesa-Nuñez, Mirko Prato, and Francesco Bonaccorso. Scalable Production of Graphene Inks via Wet-Jet Milling Exfoliation for Screen-Printed Micro-Supercapacitors. *Advanced Functional Materials*, 29(14):1807659, April 2019. 17

[132] Panagiotis G. Karagiannidis, Stephen A. Hodge, Lucia Lombardi, Flavia Tomarchio, Nicolas Decorde, Silvia Milana, Ilya Goykhman, Yang Su, Steven V. Mesite, Duncan N. Johnstone, Rowan K. Leary, Paul A. Midgley, Nicola M. Pugno, Felice Torrisi, and Andrea C. Ferrari. Microfluidization of Graphite and Formulation of Graphene-Based Conductive Inks. *ACS Nano*, 11(3):2742–2755, March 2017. 17

[133] Matthew J. Large, Sean P. Ogilvie, Aline Amorim Graf, Peter J. Lynch, Marcus A. O'Mara, Thomas Waters, Izabela Jurewicz, Jonathan P. Salvage, and Alan B. Dalton. Large-Scale Surfactant Exfoliation of Graphene and Conductivity-Optimized Graphite Enabling Wireless Connectivity. *Advanced Materials Technologies*, page 2000284, May 2020. 17

[134] Na Liu, Paul Kim, Ji Heon Kim, Jun Ho Ye, Sunkook Kim, and Cheol Jin Lee. Large-Area Atomically Thin MoS $_2$ Nanosheets Prepared Using Electrochemical Exfoliation. *ACS Nano*, 8(7):6902–6910, July 2014. 18

[135] Adriano Ambrosi and Martin Pumera. Electrochemical Exfoliation of MoS $_2$ Crystal for Hydrogen Electrogeneration. *Chemistry – A European Journal*, 24(69):18551–18555, December 2018. 18

[136] Vaiva Nagyte, Daniel James Kelly, Alexandre Felten, Gennaro Picardi, Yuyoung Shin, Adriana Alieva, Robyn E. Worsley, Khaled Parvez, Simone Dehm, Ralph Krupke, Sarah J. Haigh, Antonios Oikonomou, Andrew J. Pollard, and Cinzia Casiraghi. Raman Fingerprints of Graphene Produced by Anodic Electrochemical Exfoliation. *Nano Letters*, April 2020. 18, 75

[137] Pei Yu, Sean E. Lowe, George P. Simon, and Yu Lin Zhong. Electrochemical exfoliation of graphite and production of functional graphene. *Current Opinion in Colloid & Interface Science*, 20(5-6):329–338, October 2015. 18

[138] Yingchang Yang, Hongshuai Hou, Guoqiang Zou, Wei Shi, Honglei Shuai, Jiayang Li, and Xiaobo Ji. Electrochemical exfoliation of graphene-like two-dimensional nanomaterials. *Nanoscale*, 11(1):16–33, November 2018. 18

[139] X. Li, W. Cai, J. An, S. Kim, J. Nah, D. Yang, R. Piner, A. Velamakanni, I. Jung, E. Tutuc, S. K. Banerjee, L. Colombo, and R. S. Ruoff. Large-Area Synthesis of High-Quality and Uniform Graphene Films on Copper Foils. *Science*, 324(5932):1312–1314, June 2009. 18

[140] Yumeng Shi, Henan Li, and Lain-Jong Li. Recent advances in controlled synthesis of two-dimensional transition metal dichalcogenides via vapour deposition techniques. *Chemical Society Reviews*, 44(9):2744–2756, October 2014. 18

[141] Lisanne Peters, Cormac Ó Coileáin, Patryk Dluzynski, Rita Siris, Georg S. Duesberg, and Niall McEvoy. Directing the Morphology of Chemical Vapor Deposition-Grown MoS $_2$ on Sapphire by Crystal Plane Selection. *physica status solidi (a)*, page 2000073, May 2020. 18

[142] Siwei Luo, Conor P. Cullen, Gencai Guo, Jianxin Zhong, and Georg S. Duesberg. Investigation of growth-induced strain in monolayer MoS2 grown by chemical vapor deposition. *Applied Surface Science*, 508:145126, April 2020. 18

[143] John B. Mc Manus, Graeme Cunningham, Niall McEvoy, Conor P. Cullen, Farzan Gity, Michael Schmidt, David McAteer, Daragh Mullarkey, Igor V. Shvets, Paul K.

Hurley, Toby Hallam, and Georg S. Duesberg. Growth of 1T′ $MoTe_2$ by Thermally Assisted Conversion of Electrodeposited Tellurium Films. *ACS Applied Energy Materials*, 2(1):521–530, January 2019. 18

[144] Sean P Ogilvie, Matthew J Large, Marcus A O'Mara, Peter J Lynch, Cheuk Long Lee, Alice A K King, Claudia Backes, and Alan B Dalton. Size selection of liquid-exfoliated 2D nanosheets. *2D Materials*, 6(3):031002, April 2019. 22, 58, 87

[145] C. V. Raman and K. S. Krishnan. A New Type of Secondary Radiation. *Nature*, 121(3048):501–502, March 1928. 23

[146] Gustavo M. Do Nascimento. Introductory Chapter: The Multiple Applications of Raman Spectroscopy. In Gustavo Morari do Nascimento, editor, *Raman Spectroscopy*. InTech, April 2018. 23, 27

[147] Kazuki Hashimoto, Venkata Ramaiah Badarla, Akira Kawai, and Takuro Ideguchi. Complementary vibrational spectroscopy. *Nature Communications*, 10(1), December 2019. 25

[148] Mingxiao Ye, Dustin Winslow, Dongyan Zhang, Ravindra Pandey, and Yoke Yap. Recent Advancement on the Optical Properties of Two-Dimensional Molybdenum Disulfide (MoS2) Thin Films. *Photonics*, 2(1):288–307, March 2015. 26

[149] Martin T. Dove. *Structure and Dynamics: An Atomic View of Materials*. Oxford Master Series in Condensed Matter Physics. Oxford University Press, Oxford ; New York, 2003. 27

[150] Masahiro Kitajima. Defects in crystals studied by Raman scattering. *Critical Reviews in Solid State and Materials Sciences*, 22(4):275–349, December 1997. 27

[151] Andreas C. Albrecht. On the Theory of Raman Intensities. *The Journal of Chemical Physics*, 34(5):1476–1484, May 1961. 27

[152] J. M. Friedman and R. M. Hochstrasser. Approximate selection rules for resonance Raman spectroscopy. *Journal of the American Chemical Society*, 98(14):4043–4048, July 1976. 27

[153] L. David, A. Feldman, E. Mansfield, J. Lehman, and G. Singh. Evaluating the thermal damage resistance of graphene/carbon nanotube hybrid composite coatings. *Scientific Reports*, 4(1), May 2015. 28, 84

[154] Abdullah Alrasheed, Justin M. Gorham, Bien Cuong Tran Khac, Fadhel Alsaffar, Frank W. DelRio, Koo-Hyun Chung, and Moh. R. Amer. Surface Properties of Laser-Treated Molybdenum Disulfide Nanosheets for Optoelectronic Applications. *ACS Applied Materials & Interfaces*, 10(21):18104–18112, May 2018. 28, 84

[155] Jan Overbeck, Gabriela Borin Barin, Colin Daniels, Mickael L. Perrin, Oliver Braun, Qiang Sun, Rimah Darawish, Marta De Luca, Xiao-Ye Wang, Tim Dumslaff, Akimitsu Narita, Klaus Müllen, Pascal Ruffieux, Vincent Meunier, Roman Fasel, and Michel Calame. A Universal Length-Dependent Vibrational Mode in Graphene Nanoribbons. *ACS Nano*, 13(11):13083–13091, November 2019. 28, 84

[156] Kaito Sunamura, Tamon R. Page, Keisuke Yoshida, Taka-aki Yano, and Yuhei Hayamizu. Laser-induced electrochemical thinning of MoS $_2$. *Journal of Materials Chemistry C*, 4(15):3268–3273, 2016. 28

[157] H. C. van de Hulst. *Light Scattering by Small Particles*. Dover Publications, New York, 1981. 28

[158] Sulabha K Kulkarni. *Nanotechnology: Principles and Practices*. Cham, 2015. 28, 32

[159] Aideen Griffin, Andrew Harvey, Brian Cunningham, Declan Scullion, Tian Tian, Chih-Jen Shih, Myrta Gruening, John F Donegan, Elton J. G. Santos, Claudia Backes, and Jonathan N. Coleman. Spectroscopic Size and Thickness Metrics for Liquid-Exfoliated *h* -BN. *Chemistry of Materials*, 30(6):1998–2005, March 2018. 29

[160] Kevin Synnatschke, Patrick Arthur Cieslik, Andrew Harvey, Andres Castellanos-Gomez, Tian Tian, Chih-Jen Shih, Alexey Chernikov, Elton J. G. Santos, Jonathan N. Coleman, and Claudia Backes. Length- and Thickness-Dependent Optical Response of Liquid-Exfoliated Transition Metal Dichalcogenides. *Chemistry of Materials*, 31(24):10049–10062, December 2019. 29

[161] Hsiao-Lu Lee and Nolan T. Flynn. X-ray Photoelectron Spectroscopy. In D. R. Vij, editor, *Handbook of Applied Solid State Spectroscopy*, pages 485–507. Springer US, Boston, MA, 2006. 29

[162] O. I. Klyushnikov. Method to determine the work function using X-ray photoelectron spectroscopy. *Journal of Structural Chemistry*, 39(6):944–947, November 1998. 29

[163] D. Ganta, S. Sinha, and Richard T. Haasch. 2-D Material Molybdenum Disulfide Analyzed by XPS. *Surface Science Spectra*, 21(1):19–27, December 2014. 30

[164] Ali Syari'ati, Sumit Kumar, Amara Zahid, Abdurrahman Ali El Yumin, Jianting Ye, and Petra Rudolf. Photoemission spectroscopy study of structural defects in molybdenum disulfide (MoS_2) grown by chemical vapor deposition (CVD). *Chemical Communications*, 55(70):10384–10387, August 2019. 30

[165] Tomasz Tański, Marcin Staszuk, and Bogusław Ziębowicz, editors. *Atomic-Force Microscopy and Its Applications*. IntechOpen, January 2019. 30

[166] Robert W. Carpick and Miquel Salmeron. Scratching the Surface: Fundamental Investigations of Tribology with Atomic Force Microscopy. *Chemical Reviews*, 97(4):1163–1194, June 1997. 30

[167] David B. Williams and C. Barry Carter. *Transmission Electron Microscopy: A Textbook for Materials Science*. Springer, New York, 2. ed edition, 2009. 34

[168] Stéphane Badaire, Philippe Poulin, Maryse Maugey, and Cécile Zakri. In Situ Measurements of Nanotube Dimensions in Suspensions by Depolarized Dynamic Light Scattering. *Langmuir*, 20(24):10367–10370, November 2004. 34

[169] George D. J. Phillies. Translational diffusion coefficient of macroparticles in solvents of high viscosity. *The Journal of Physical Chemistry*, 85(19):2838–2843, September 1981. 34

[170] Mustafa Lotya, Aliaksandra Rakovich, John F Donegan, and Jonathan N Coleman. Measuring the lateral size of liquid-exfoliated nanosheets with dynamic light scattering. *Nanotechnology*, 24(26):265703, July 2013. 34, 90

[171] Jeffrey D. Clogston and Anil K. Patri. Zeta Potential Measurement. In Scott E. McNeil, editor, *Characterization of Nanoparticles Intended for Drug Delivery*, volume 697, pages 63–70. Humana Press, Totowa, NJ, 2011. 35

[172] Gregory V. Lowry, Reghan J. Hill, Stacey Harper, Alan F. Rawle, Christine Ogilvie Hendren, Fred Klaessig, Ulf Nobbmann, Philip Sayre, and John Rumble. Guidance to improve the scientific value of zeta-potential measurements in nanoEHS. *Environmental Science: Nano*, 3(5):953–965, August 2016. 35

[173] Ronan J Smith, Mustafa Lotya, and Jonathan N Coleman. The importance of repulsive potential barriers for the dispersion of graphene using surfactants. *New Journal of Physics*, 12(12):125008, December 2010. 35, 41

[174] Allen J. Bard and Larry R. Faulkner. *Electrochemical Methods: Fundamentals and Applications*. Wiley, New York, 2nd ed edition, 2001. 36

[175] Paul S. Nnamchi and Camillus S. Obayi. Electrochemical Characterization of Nanomaterials. In *Characterization of Nanomaterials*, pages 103–127. Elsevier, 2018. 36

[176] Kai-Ge Zhou, Nan-Nan Mao, Hang-Xing Wang, Yong Peng, and Hao-Li Zhang. A Mixed-Solvent Strategy for Efficient Exfoliation of Inorganic Graphene Analogues. *Angewandte Chemie International Edition*, 50(46):10839–10842, November 2011. 39

[177] Lixin Xu, John-Wesley McGraw, Fan Gao, Mark Grundy, Zhibin Ye, Zhiyong Gu, and Jeffrey L. Shepherd. Production of High-Concentration Graphene Dispersions

in Low-Boiling-Point Organic Solvents by Liquid-Phase Noncovalent Exfoliation of Graphite with a Hyperbranched Polyethylene and Formation of Graphene/Ethylene Copolymer Composites. *The Journal of Physical Chemistry C*, 117(20):10730–10742, May 2013. 39

[178] Xiaoyan Zhang, Anthony C. Coleman, Nathalie Katsonis, Wesley R. Browne, Bart J. van Wees, and Ben L. Feringa. Dispersion of graphene in ethanol using a simple solvent exchange method. *Chemical Communications*, 46(40):7539, September 2010. 39

[179] Huaizhi Liu, Liao Xu, Weixu Liu, Bo Zhou, Yinyan Zhu, Lihua Zhu, and Xiaoqing Jiang. Production of mono- to few-layer MoS2 nanosheets in isopropanol by a salt-assisted direct liquid-phase exfoliation method. *Journal of Colloid and Interface Science*, 515:27–31, April 2018. 40

[180] Jianfeng Shen, Yongmin He, Jingjie Wu, Caitian Gao, Kunttal Keyshar, Xiang Zhang, Yingchao Yang, Mingxin Ye, Robert Vajtai, Jun Lou, and Pulickel M. Ajayan. Liquid Phase Exfoliation of Two-Dimensional Materials by Directly Probing and Matching Surface Tension Components. *Nano Letters*, 15(8):5449–5454, August 2015. 40

[181] Kathleen M. McCreary, Aubrey T. Hanbicki, Saujan V. Sivaram, and Berend T. Jonker. A- and B-exciton photoluminescence intensity ratio as a measure of sample quality for transition metal dichalcogenide monolayers. *APL Materials*, 6(11):111106, November 2018. 41

[182] P. Nemes-Incze, Z. Osváth, K. Kamarás, and L.P. Biró. Anomalies in thickness measurements of graphene and few layer graphite crystals by tapping mode atomic force microscopy. *Carbon*, 46(11):1435–1442, September 2008. 42, 66

[183] Hong Li, Qing Zhang, Chin Chong Ray Yap, Beng Kang Tay, Teo Hang Tong Edwin, Aurelien Olivier, and Dominique Baillargeat. From Bulk to Monolayer

MoS2: Evolution of Raman Scattering. *Advanced Functional Materials*, 22(7):1385–1390, April 2012. 43

[184] L Seguin, M Figlarz, R Cavagnat, and J.-C Lassègues. Infrared and Raman spectra of MoO3 molybdenum trioxides and MoO3 · xH2O molybdenum trioxide hydrates. *Spectrochimica Acta Part A: Molecular and Biomolecular Spectroscopy*, 51(8):1323–1344, July 1995. 44

[185] M. Dieterle and G. Mestl. Raman spectroscopy of molybdenum oxides. *Physical Chemistry Chemical Physics*, 4(5):822–826, February 2002. 44

[186] Damien Hanlon, Claudia Backes, Thomas M. Higgins, Marguerite Hughes, Arlene O'Neill, Paul King, Niall McEvoy, Georg S. Duesberg, Beatriz Mendoza Sanchez, Henrik Pettersson, Valeria Nicolosi, and Jonathan N. Coleman. Production of Molybdenum Trioxide Nanosheets by Liquid Exfoliation and Their Application in High-Performance Supercapacitors. *Chemistry of Materials*, 26(4):1751–1763, February 2014. 46, 50, 51, 52

[187] A. Chithambararaj, N. Rajeswari Yogamalar, and A. Chandra Bose. Hydrothermally Synthesized h-MoO $_3$ and α-MoO $_3$ Nanocrystals: New Findings on Crystal-Structure-Dependent Charge Transport. *Crystal Growth & Design*, 16(4):1984–1995, April 2016. 46

[188] Raul Arenal, Katia March, Chris P. Ewels, Xavier Rocquefelte, Mathieu Kociak, Annick Loiseau, and Odile Stéphan. Atomic Configuration of Nitrogen-Doped Single-Walled Carbon Nanotubes. *Nano Letters*, 14(10):5509–5516, October 2014. 47

[189] Francis Leonard Deepak, Alvaro Mayoral, and Raul Arenal, editors. *Advanced Transmission Electron Microscopy: Applications to Nanomaterials*. Springer, Cham, 2015. 47

[190] Prabhat Kumar, Megha Singh, and G B Reddy. Oxidation of core–shell MoO $_2$ –MoS $_2$ nanoflakes in different O $_2$ ambience. *Materials Research Express*, 4(3):036405, March 2017. 49

[191] Prachi Budania, Paul Baine, John Montgomery, Conor McGeough, Tony Cafolla, Mircea Modreanu, David McNeill, Neil Mitchell, Greg Hughes, and Paul Hurley. Long-term stability of mechanically exfoliated MoS2 flakes. *MRS Communications*, 7(04):813–818, December 2017. 49

[192] Y. Shigegaki, S. K. Basu, M. Wakihara, and M. Taniguchi. Thermal analysis and kinetics of oxidation of molybdenum sulfides. *Journal of Thermal Analysis*, 34(5-6):1427–1440, September 1988. 49

[193] Santosh Kc, Roberto C. Longo, Robert M. Wallace, and Kyeongjae Cho. Surface oxidation energetics and kinetics on MoS $_2$ monolayer. *Journal of Applied Physics*, 117(13):135301, April 2015. 49

[194] David Flaxbart. Kirk-Othmer Encyclopedia of Chemical Technology, Fourth Edition, 27-Volume Set Wiley Interscience: New York, 1992-1998. $7884. ISBN 0-471-52704-1. *Journal of the American Chemical Society*, 121(10):2339–2339, March 1999. 49

[195] Chris Franco and John Olmsted III. Photochemical determination of the solubility of oxygen in various media. *Talanta*, 37(9):905–909, September 1990. 49

[196] John A. Dean and Norbert Adolph Lange, editors. *Lange's Handbook of Chemistry*. McGraw-Hill Handbooks. McGraw-Hill, New York, NY, 15. ed edition, 1999. 53

[197] David McAteer, Zahra Gholamvand, Niall McEvoy, Andrew Harvey, Eoghan O'Malley, Georg S Duesberg, and Jonathan N Coleman. Thickness Dependence and Percolation Scaling of Hydrogen Production Rate in MoS $_2$ Nanosheet and Nanosheet–Carbon Nanotube Composite Catalytic Electrodes. *ACS Nano*, 10(1):672–683, January 2016. 54, 55

[198] Yifei Yu, Sheng-Yang Huang, Yanpeng Li, Stephan N. Steinmann, Weitao Yang, and Linyou Cao. Layer-Dependent Electrocatalysis of MoS $_2$ for Hydrogen Evolution. *Nano Letters*, 14(2):553–558, February 2014. 54, 55

[199] Berit Hinnemann, Poul Georg Moses, Jacob Bonde, Kristina P. Jørgensen, Jane H. Nielsen, Sebastian Horch, Ib Chorkendorff, and Jens K. Nørskov. Biomimetic Hydrogen Evolution: MoS $_2$ Nanoparticles as Catalyst for Hydrogen Evolution. *Journal of the American Chemical Society*, 127(15):5308–5309, April 2005. 54

[200] Jesse D. Benck, Thomas R. Hellstern, Jakob Kibsgaard, Pongkarn Chakthranont, and Thomas F. Jaramillo. Catalyzing the Hydrogen Evolution Reaction (HER) with Molybdenum Sulfide Nanomaterials. *ACS Catalysis*, 4(11):3957–3971, November 2014. 54

[201] Zahra Gholamvand, David McAteer, Andrew Harvey, Claudia Backes, and Jonathan N. Coleman. Electrochemical Applications of Two-Dimensional Nanosheets: The Effect of Nanosheet Length and Thickness. *Chemistry of Materials*, 28(8):2641–2651, April 2016. 55, 56, 98

[202] Damien Voiry, Maryam Salehi, Rafael Silva, Takeshi Fujita, Mingwei Chen, Tewodros Asefa, Vivek B. Shenoy, Goki Eda, and Manish Chhowalla. Conducting MoS $_2$ Nanosheets as Catalysts for Hydrogen Evolution Reaction. *Nano Letters*, 13(12):6222–6227, December 2013. 55

[203] Xinyi Chia, Alex Yong Sheng Eng, Adriano Ambrosi, Shu Min Tan, and Martin Pumera. Electrochemistry of Nanostructured Layered Transition-Metal Dichalcogenides. *Chemical Reviews*, 115(21):11941–11966, November 2015. 55, 85

[204] Xinyi Chia, Adriano Ambrosi, David Sedmidubský, Zdeněk Sofer, and Martin Pumera. Precise Tuning of the Charge Transfer Kinetics and Catalytic Properties of MoS $_2$ Materials via Electrochemical Methods. *Chemistry - A European Journal*, 20(52):17426–17432, December 2014. 55

[205] Ganesh R. Bhimanapati, Trevor Hankins, Yu Lei, Rafael A. Vilá, Ian Fuller, Mauricio Terrones, and Joshua A. Robinson. Growth and Tunable Surface Wettability of Vertical MoS $_2$ Layers for Improved Hydrogen Evolution Reactions. *ACS Applied Materials & Interfaces*, 8(34):22190–22195, August 2016. 56

[206] Peter Bøggild. The war on fake graphene. *Nature*, 562(7728):502–503, October 2018. 58

[207] Alan P. Kauling, Andressa T. Seefeldt, Diego P. Pisoni, Roshini C. Pradeep, Ricardo Bentini, Ricardo V. B. Oliveira, Konstantin S. Novoselov, and Antonio H. Castro Neto. The Worldwide Graphene Flake Production. *Advanced Materials*, 30(44):1803784, November 2018. 58

[208] Peter Wick, Anna E. Louw-Gaume, Melanie Kucki, Harald F. Krug, Kostas Kostarelos, Bengt Fadeel, Kenneth A. Dawson, Anna Salvati, Ester Vázquez, Laura Ballerini, Mauro Tretiach, Fabio Benfenati, Emmanuel Flahaut, Laury Gauthier, Maurizio Prato, and Alberto Bianco. Classification Framework for Graphene-Based Materials. *Angewandte Chemie International Edition*, 53(30):7714–7718, July 2014. 58

[209] L.M. Malard, M.A. Pimenta, G. Dresselhaus, and M.S. Dresselhaus. Raman spectroscopy in graphene. *Physics Reports*, 473(5-6):51–87, April 2009. 59

[210] Andrea C. Ferrari and Denis M. Basko. Raman spectroscopy as a versatile tool for studying the properties of graphene. *Nature Nanotechnology*, 8(4):235–246, April 2013. 59

[211] Shou-En Zhu, Shengjun Yuan, and G. C. A. M. Janssen. Optical transmittance of multilayer graphene. *EPL (Europhysics Letters)*, 108(1):17007, October 2014. 60

[212] Cristina Coman and Loredana Florina Leopold. Raman Mapping: Emerging Applications. In Khan Maaz, editor, *Raman Spectroscopy and Applications*. InTech, February 2017. 60

[213] Youngbum Kim, Eun Ji Lee, Shrawan Roy, Anir S. Sharbirin, Lars-Gunnar Ranz, Thomas Dieing, and Jeongyong Kim. Measurement of lateral and axial resolution of confocal Raman microscope using dispersed carbon nanotubes and suspended graphene. *Current Applied Physics*, 20(1):71–77, October 2019. 62

[214] J. F. Morhange, R. Beserman, and M. Balkanski. Raman study of the vibrational properties of implanted silicon. *Physica Status Solidi (a)*, 23(2):383–391, June 1974. 62

[215] Alex Henderson. Renishaw File Reader. Zenodo, April 2017. 63

[216] Z. H. Ni, H. M. Wang, J. Kasim, H. M. Fan, T. Yu, Y. H. Wu, Y. P. Feng, and Z. X. Shen. Graphene Thickness Determination Using Reflection and Contrast Spectroscopy. *Nano Letters*, 7(9):2758–2763, September 2007. 66

[217] Cameron J Shearer, Ashley D Slattery, Andrew J Stapleton, Joseph G Shapter, and Christopher T Gibson. Accurate thickness measurement of graphene. *Nanotechnology*, 27(12):125704, March 2016. 66

[218] Gitti L. Frey, Reshef Tenne, Manyalibo J. Matthews, M. S. Dresselhaus, and G. Dresselhaus. Raman and resonance Raman investigation of MoS 2 nanoparticles. *Physical Review B*, 60(4):2883–2892, July 1999. 68, 76

[219] Jia-He Fan, Po Gao, An-Min Zhang, Bai-Ren Zhu, Hua-Ling Zeng, Xiao-Dong Cui, Rui He, and Qing-Ming Zhang. Resonance Raman scattering in bulk 2H-MX $_2$ (M = Mo, W; X = S, Se) and monolayer MoS $_2$. *Journal of Applied Physics*, 115(5):053527, February 2014. 68

[220] K. Gołasa, M. Grzeszczyk, R. Bożek, P. Leszczyński, A. Wysmołek, M. Potemski, and A. Babiński. Resonant Raman scattering in MoS 2 —From bulk to monolayer. *Solid State Communications*, 197:53–56, November 2014. 68, 76

[221] Péter Vancsó, Gábor Zsolt Magda, János Pető, Ji-Young Noh, Yong-Sung Kim, Chanyong Hwang, László P. Biró, and Levente Tapasztó. The intrinsic defect struc-

ture of exfoliated MoS2 single layers revealed by Scanning Tunneling Microscopy. *Scientific Reports*, 6(1), September 2016. 71, 134

[222] Lei Gong, Ian A. Kinloch, Robert J. Young, Ibtsam Riaz, Rashid Jalil, and Konstantin S. Novoselov. Interfacial Stress Transfer in a Graphene Monolayer Nanocomposite. *Advanced Materials*, 22(24):2694–2697, May 2010. 71

[223] Diego L. Silva, João Luiz E. Campos, Thales F.D. Fernandes, Jeronimo N. Rocha, Lucas R.P. Machado, Eder M. Soares, Douglas R. Miquita, Hudson Miranda, Cassiano Rabelo, Omar P. Vilela Neto, Ado Jorio, and Luiz Gustavo Cançado. Raman spectroscopy analysis of number of layers in mass-produced graphene flakes. *Carbon*, 161:181–189, May 2020. 75

[224] Biswanath Chakraborty, H. S. S. Ramakrishna Matte, A. K. Sood, and C. N. R. Rao. Layer-dependent resonant Raman scattering of a few layer MoS $_2$: Raman scattering of a few layer MoS $_2$. *Journal of Raman Spectroscopy*, 44(1):92–96, January 2013. 76

[225] Bruno R. Carvalho, Yuanxi Wang, Sandro Mignuzzi, Debdulal Roy, Mauricio Terrones, Cristiano Fantini, Vincent H. Crespi, Leandro M. Malard, and Marcos A. Pimenta. Intervalley scattering by acoustic phonons in two-dimensional MoS2 revealed by double-resonance Raman spectroscopy. *Nature Communications*, 8(1), April 2017. 76

[226] Neil J. Everall. Confocal Raman Microscopy: Performance, Pitfalls, and Best Practice: Invited Lecture at the Symposium “50 Years of SAS: Looking to the Future with Vibrational Spectroscopy” at Pittcon 2008, New Orleans, Louisiana. *Applied Spectroscopy*, 63(9):245A–262A, September 2009. 81

[227] Teng-Xiang Huang, Xin Cong, Si-Si Wu, Kai-Qiang Lin, Xu Yao, Yu-Han He, Jiang-Bin Wu, Yi-Fan Bao, Sheng-Chao Huang, Xiang Wang, Ping-Heng Tan, and Bin Ren. Probing the edge-related properties of atomically thin MoS2 at nanoscale. *Nature Communications*, 10(1), December 2019. 84, 86

[228] Joon Young Kwak. Absorption coefficient estimation of thin MoS2 film using attenuation of silicon substrate Raman signal. *Results in Physics*, 13:102202, June 2019. 85, 135, 136

[229] Wen-Bo Shi, Jie He, Qing-Xuan Li, Xi-Chao She, Di Wang, Hao Jing, Rui-Li Zhang, Jin-Zhu Zhao, Ru-Wen Peng, Hu Xu, and Mu Wang. Asymmetric valley polarization and photoluminescence in MoS $_2$ /MoO $_3$ heterostructure. *Optics Express*, 27(26):38451, December 2019. 92

[230] Hye Min Oh, Gang Hee Han, Hyun Kim, Jung Jun Bae, Mun Seok Jeong, and Young Hee Lee. Photochemical Reaction in Monolayer MoS $_2$ *via* Correlated Photoluminescence, Raman Spectroscopy, and Atomic Force Microscopy. *ACS Nano*, 10(5):5230–5236, May 2016. 92

[231] Felix Carrascoso, Gabriel Sánchez-Santolino, Chun-wei Hsu, Norbert M. Nemes, Almudena Torres-Pardo, Patricia Gant, Federico J. Mompeán, Kourosh Kalantar-zadeh, José A. Alonso, Mar García-Hernández, Riccardo Frisenda, and Andres Castellanos-Gomez. Direct Transformation of Crystalline MoO3 into Few-Layers MoS2. *Materials*, 13(10):2293, May 2020. 92

[232] Guangfeng Wang, Xiuping He, Lingling Wang, Aixia Gu, Yan Huang, Bin Fang, Baoyou Geng, and Xiaojun Zhang. Non-enzymatic electrochemical sensing of glucose. *Microchimica Acta*, 180(3-4):161–186, February 2013. 94, 95

[233] Sejin Park, Hankil Boo, and Taek Dong Chung. Electrochemical non-enzymatic glucose sensors. *Analytica Chimica Acta*, 556(1):46–57, January 2006. 95

[234] Peter J. Lynch, Aline Amorim Graf, Sean P. Ogilvie, Matthew J. Large, Jonathan P. Salvage, and Alan B. Dalton. Surfactant-free liquid-exfoliated copper hydroxide nanocuboids for non-enzymatic electrochemical glucose detection. *Journal of Materials Chemistry B*, 8:7733–7739, 2020. 95

[235] David S. Hall, David J. Lockwood, Christina Bock, and Barry R. MacDougall. Nickel hydroxides and related materials: A review of their structures, synthesis

and properties. *Proceedings of the Royal Society A: Mathematical, Physical and Engineering Sciences*, 471(2174):20140792, February 2015. 95

[236] H. R. Oswald, A. Reller, H. W. Schmalle, and E. Dubler. Structure of copper(II) hydroxide, Cu(OH)2. *Acta Crystallographica Section C Crystal Structure Communications*, 46(12):2279–2284, December 1990. 95

[237] Yilin Deng, Albertus D. Handoko, Yonghua Du, Shibo Xi, and Boon Siang Yeo. *In Situ* Raman Spectroscopy of Copper and Copper Oxide Surfaces during Electrochemical Oxygen Evolution Reaction: Identification of Cu ^{III} Oxides as Catalytically Active Species. *ACS Catalysis*, 6(4):2473–2481, April 2016. 95

[238] Hongsheng Liu, Nannan Han, and Jijun Zhao. Atomistic insight into the oxidation of monolayer transition metal dichalcogenides: From structures to electronic properties. *RSC Advances*, 5(23):17572–17581, January 2015. 98

[239] Ayse Berkdemir, Humberto R. Gutiérrez, Andrés R. Botello-Méndez, Néstor Perea-López, Ana Laura Elías, Chen-Ing Chia, Bei Wang, Vincent H. Crespi, Florentino López-Urías, Jean-Christophe Charlier, Humberto Terrones, and Mauricio Terrones. Identification of individual and few layers of WS2 using Raman Spectroscopy. *Scientific Reports*, 3(1), December 2013. 100

[240] Marco Bernardi, Maurizia Palummo, and Jeffrey C. Grossman. Extraordinary Sunlight Absorption and One Nanometer Thick Photovoltaics Using Two-Dimensional Monolayer Materials. *Nano Letters*, 13(8):3664–3670, August 2013. 136

[241] A R Beal and H P Hughes. Kramers-Kronig analysis of the reflectivity spectra of 2H-MoS $_2$, 2H-MoSe $_2$ and 2H-MoTe $_2$. *Journal of Physics C: Solid State Physics*, 12(5):881–890, March 1979. 136

Appendix A

Inter-defect distance calculation from defect density

Starting with the assumption that basal plane defects are distributed uniformly (that is, according to a Poisson Point Process with intensity measure λ), it is known that the inter-defect distances d_e are distributed according to the Nearest Neighbour distribution:

$$P(d_e) = 1 - e^{-\lambda \pi d_e^2} \tag{A.1}$$

The probability density function is then:

$$p(d_e) = 2\lambda \pi d_e e^{-\lambda \pi d_e^2} \tag{A.2}$$

The average value of d_e for a large area of the basal plane whose length $L \to \infty$:

$$\begin{aligned} \langle d_e \rangle &= \int_0^\infty d_e p(d_e) \mathrm{d}d_e \\ &= 2\lambda\pi \int_0^\infty d_e^2 e^{-\lambda \pi d_e^2} \mathrm{d}d_e \\ &= 2\lambda\pi \frac{1}{4\pi\lambda^{1/2}} \end{aligned}$$

$$\langle d_e \rangle = \frac{1}{2\sqrt{\lambda}} \tag{A.3}$$

Vancsó *et al.* [221] estimated the defect density per unit area λ to be between $5 \times 10^{12}\,\mathrm{cm}^{-2}$ and $5 \times 10^{13}\,\mathrm{cm}^{-2}$. Using λ equal to $1 \times 10^{13}\,\mathrm{cm}^{-2}$ yields an inter-defect distance of $\sim 2\,\mathrm{nm}$.

Appendix B

Absorption coefficient estimation using Raman spectroscopy

Kwak [228] studied a simple method to estimate the absorption coefficient of MoS_2 using Raman spectroscopy, AFM measurements and a light attenuation model. If the nanosheet is thin, silicon modes from the substrate will also be observed in the resulting Raman spectrum. The expression that describes the phenomenon is:

$$I = I_0 e^{-2\alpha t} \tag{B.1}$$

where I is the silicon Raman peak intensity from the nanosheet, I_0 is the reference silicon Raman peak intensity taken at the substrate under the same measurement conditions, t is the thickness of the MoS_2 nanosheet, and α is the MoS_2 absorption coefficient (cm^{-1}).

Applying the expression to spectra measured at the same spot before and after laser oxidation, as discussed in Chapter 6, gives:

$$I_A = I_0 e^{-2\alpha_A t_A} \text{ and } I_B = I_0 e^{-2\alpha_B t_B}$$

where the subscripts A and B refer to after and before laser treatment, respectively.

Assuming $\alpha_A = \alpha_B = \alpha$ for MoS_2 and calculating the intensity ratio as follows:

$$\frac{I_B}{I_A} = \frac{I_0 e^{-2\alpha t_A}}{I_0 e^{-2\alpha t_B}}$$

The absorption coefficient was estimated as $2.79 \times 10^6\,\mathrm{cm}^{-1}$ for monolayer MoS_2 [228]. However, the value for bulk is between 0.1 and $0.6 \times 10^6\,\mathrm{cm}^{-1}$ [240, 241]. Using $0.3 \times 10^6\,\mathrm{cm}^{-1}$, a value consistent with previous measurements for the samples studied in this thesis, and the intensity ratio difference ($I_B/I_A = 0.963$) yield:

$$t_B - t_A = 6.3 \times 10^{-8}\ \mathrm{cm} = 0.63\ \mathrm{nm} \tag{B.2}$$

A value consistent with previous measurements of interlayer spacing in MoS_2[7].

Appendix C

Size and thickness analysis using metrics from Chapter 6 for every LCC step

Spectroscopic metrics require microscopic calibration. Two Raman metrics were developed in Chapter 6, one for layer number and other for nanosheet length. Here, the comparison of the distributions obtained from both characterisation techniques are shown for every LCC step of an LPE MoS_2 dispersion. The first column has representative AFM micrographs, whilst the second one has Raman maps colour-coded for layer number determined by the present metric. Both measurements are done on the same sample but not the same area. Columns three and four represent the histograms for characteristic length and layer number, respectively. Distributions in red were obtained from the newly-developed Raman metric and in blue from AFM measurements. Rows A to J are, in order, the samples labelled according to different centrifugation times, since relative *g*-force was kept constant ($3,000$ *g*): 9 min, 12 min, 14 min, 20 min, 40 min, 1 h, 2 h, 4 h, 8 h, and 12 h.

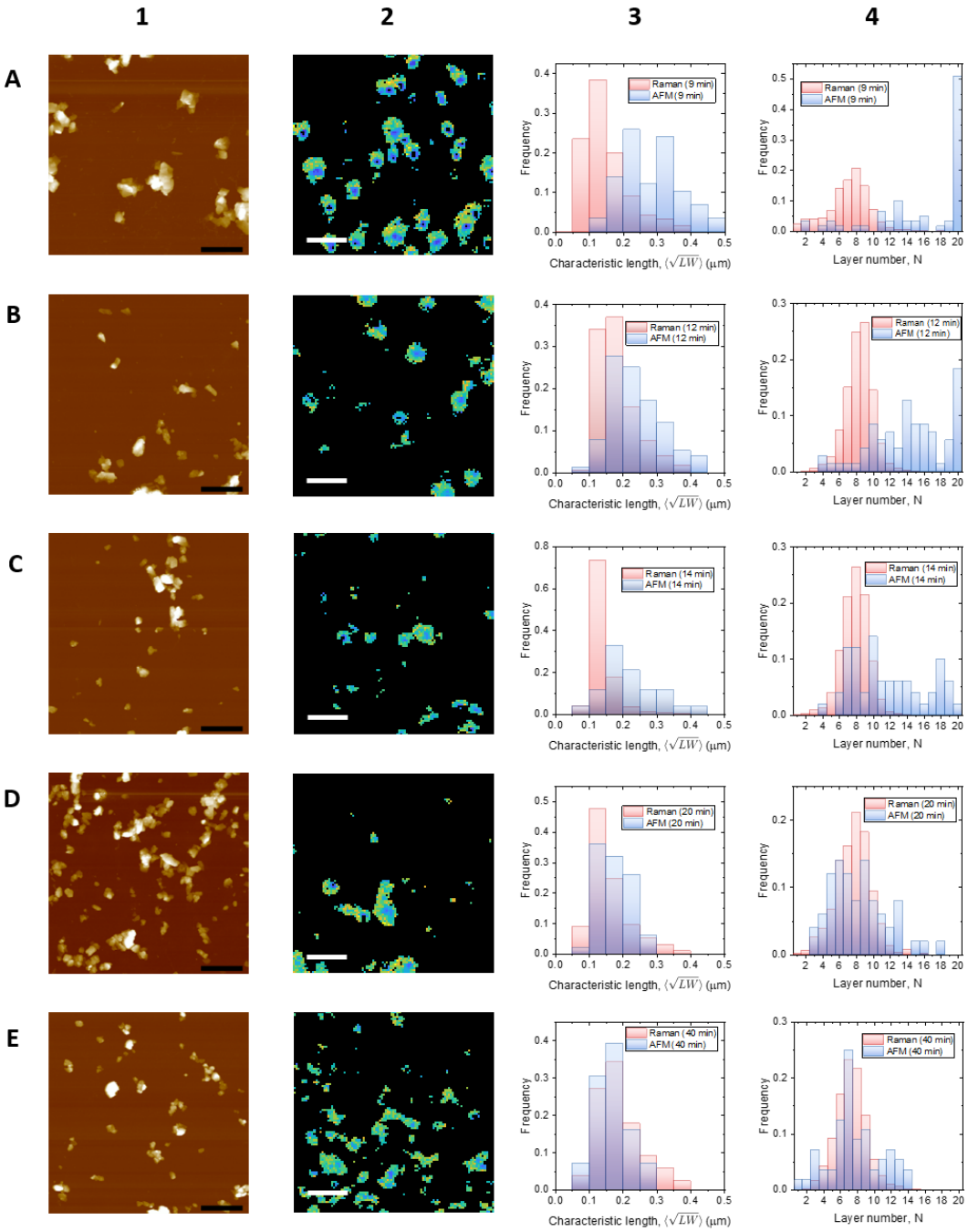
1
2
3
4
A
B
C
D
E
Raman (9 min)
AFM (9 min)
Raman (12 min)
AFM (12 min)
Raman (14 min)
AFM (14 min)
Raman (20 min)
AFM (20 min)
Raman (40 min)
AFM (40 min)
Frequency
Characteristic length, $\langle\sqrt{LW}\rangle$ (μm)
Layer number, N

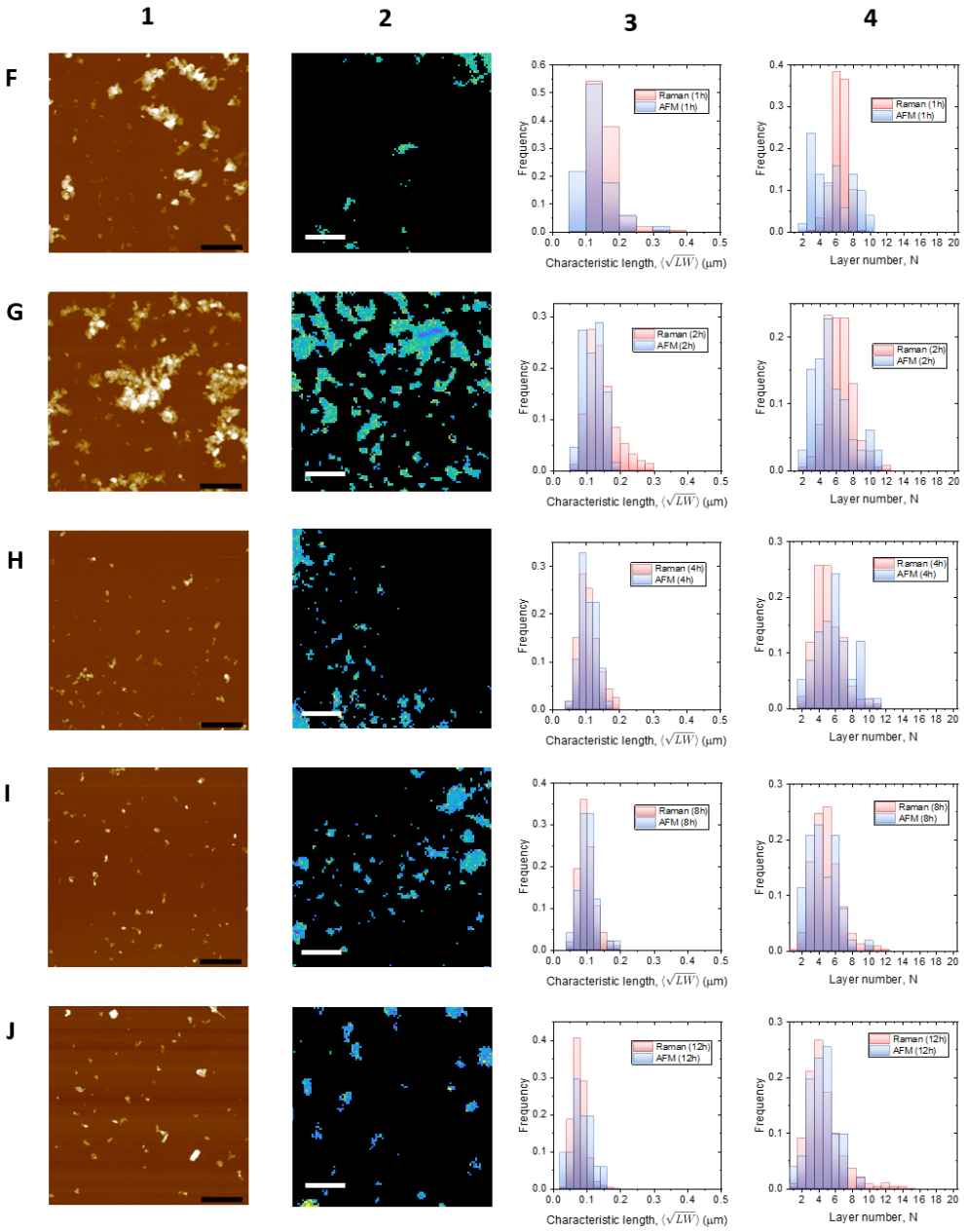

Figure C.1: **(1)** Representative AFM micrograph, **(2)** Raman map colour-coded according to layer number, **(3)** histogram for characteristic length using both Raman and AFM, and **(4)** histograms of layer number using the same techniques for every LCC series sample: **A:** 9 min, **B:** 12 min, **C:** 14 min, **D:** 20 min, **E:** 40 min, **F:** 1 h, **G:** 2 h, **H:** 4 h, **I:** 8 h, and **J:** 12 h. Same scale was used for each column to highlight the differences for each sample. For the AFM micrographs, scale bar is 1 μm, whilst the scale bar for the Raman maps is 5 μm.